Investigating Mechanisms Leading to Ventricular Tachycardia Following Cardiac Stem Cell Therapy

Chelsea Elizabeth Gibbs

A dissertation

submitted in partial fulfillment of the

requirements for the degree of

Doctor of Philosophy

University of Washington

2024

Reading Committee:

Patrick Boyle, Chair

Jennifer Davis

Hao Yuan Kueh

Program Authorized to Offer Degree:

Bioengineering

University of Washington

Abstract

Investigating Mechanisms Leading to Ventricular Tachycardia Following Cardiac Stem Cell Injections

Chelsea Elizabeth Gibbs

Chair of the Supervisory Committee:
Patrick Boyle
Department of Bioengineering

This dissertation discusses the use of computational models to understand possible mechanisms leading to ventricular tachycardia (VT) following cardiac regenerative therapies. We review the history of cardiac stem cell therapies and the current challenges being faced in Chapter 1. Particular emphasis is given to how computational models are a valuable tool for understanding VT mechanisms. Chapter 2 tests the hypothesis that VT following stem cell therapy can be explained by the evolution of graft-host coupling over time in novel computational slice models. These models are derived from 2D histology images of non-human primates that provide a realistic look at engrafted cell geometry. Chapter 3 explores how individual grafts and groups of grafts can affect arrhythmogenicity and looks at spatial parameters that may be important for future injection strategies.

Chapter 4 examines how modulation of the intrinsic beating rate of stem cell-derived cardiomyocytes affects focal VT in three in silico human slice models. The work presented in this dissertation provides valuable insights into VT mechanisms and new toolsets that can be used to generate and test hypotheses that can be used by experimentalists and computational modelers alike.

Table of Contents

Acknowledgments

While this dissertation bears my name, this work would not have been possible without the community of scientists, colleagues, family, and friends who helped me along the way. Whether you've been on this journey with me my entire life or have only just joined me, I want to say thank you.

I would first like to thank my PhD advisor, **Dr. Patrick Boyle**, for his mentorship and guidance over the past five years. He has helped me grow as a scientific writer, to trust my gut when data does not make sense, and to find my voice as an independent scientist.

Beyond my supervisor, I would like to thank the rest of my supervisory committee: **Drs. Hao Yuan Kueh, Jennifer Davis, Kenta Nakamura, Chuck Murry**, and **Andrew Stergachias**. Each of you has been a critical part of my PhD journey, providing invaluable insights and asking questions that helped change the trajectory of my research.

Thank you to **Dr. Silvia Marchiano** and my other collaborators in the Murry lab. Without your help, I don't think my first project would have prepared me for the rest of my PhD.

I would also like to thank my peers in the Cardiac Systems Simulations (CardSS) lab. **Drs. Savannah Bifulco and Alex Ochs**, who have been with me since the beginning of my PhD journey. Your feedback, knowledge, and friendship have meant a lot to me, especially during the pandemic. I do not know if half of my figures and abstracts would have looked nearly as good without your help. I would also like to thank **Matt Magoon, Åshild Telle**, and **Surbhi Sharma,** who have joined the lab more recently. You all have been a great asset to me as I finished up my work.

I want to thank **Kevin Bishop** for our thesis writing group. Your feedback on many of these pages has been invaluable. I also want to thank **Sarah Nick** and **Irina Kopyeva**, who were always willing to go hiking, skiing, swimming, or meet up to watch reality TV with me. I could not have asked for better roommates when I first moved to Seattle. You have now become some of my closest friends. To all my other friends across the country, thank you for your encouragement and support.

To my parents, **Jerry** and **Stacey,** thank you for your unwavering support. You have also always supported me and my dreams. Thank you for always being a phone call away and answering when I need to tell you about the uncertainty and triumphs of my PhD. Thank you for not asking why and instead always asking how we can help. It means the world to me.

Finally, I would like to thank my partner and best friend, **Joshua**. You have seen me go through the highs and lows of my PhD and have been there to support me every step of the way. Whether that be with ice cream and hugs or going out to celebrate my various milestones. Your belief, support, humor, and love have been something I am immensely grateful for. I love you, and I can’t wait to see what the future holds.

List of Figures

List of Tables

List of Abbreviations

AUC	Area under the curve
AUROC	Area under receiver operating characteristics
BPM	Beats per minute
EA	Engraftment Arrhythmia
ECG	Electrocardiogram
EHT	Engineered Heart Tissue
EP	Electrophysiology
GHE	Graft-Initiated Host Excitation
Graft	Engrafted hPSC-CMs
G_{CaT}	Conductance value of t-type calcium
G_{f}	Conductance value of funny current
G_{K1}	Conductance value of inward rectifier potassium current
G_{Kr}	Conductance value of rapidly activating delayed rectifier potassium current
G_{Ks}	Conductance value of slowly activating delayed rectifier potassium current
hESC-CM	Human Embryonic Stem Cell-Derived Cardiomyocytes
hiPSC-CM	Human Induced Pluripotent Stem Cell-Derived Cardiomyocytes
hPSC-CM	Human Pluripotent Stem Cell-Derived Cardiomyocytes
hESC	Human Embryonic Stem Cell

hiPSC	Human Induced Pluripotent Stem Cell
HF	Heart Failure
I_{CaT}	T-type Calcium Current
I_f	“Funny” Current
I_{K1}	Inward Rectifier Potassium Current
I_{Kr}	Rapidly activating delayed rectifier potassium
I_{Ks}	Slowly activating delayed rectifier potassium
I_{NCX}	Sodium-Calcium Exchanger
MDP	Minimum Diastolic Potential
MI	Myocardial Infarction
NHP	Non-Human Primate
ODE	Ordinary Differential Equation
p_C	Graft-host percent connected
PDMS	Polydimethylsiloxane
RMP	Resting Membrane Potential
VT	Ventricular tachycardia
WOV	Window of vulnerability
$\sigma_{hPSC\text{-}CM}$	Isotropic conductivity tensor value for hPSC-CM
σ_L	Conductivity tensor values in the longitudinal direction
σ_T	Conductivity tensor values in the transverse direction

Publications

1. Blackwell DJ, Faggioni M, Wleklinski MJ, Gomez-Hurtado N, Venkataraman R, **Gibbs CE**, Baudenbacher FJ, Gong S, Fishman GI, Boyle PM, Pfeifer K, Knollmann BC. "The Purkinje-myocardial junction is the anatomic origin of ventricular arrhythmia in CPVT". *JCI Insight*. 2022 Feb 8;7(3):e151893. doi: 10.1172/jci.insight.151893. PMID: 34990403; PMCID: PMC8855823.
2. **Gibbs CE***, Marchianó S, Zhang K, Yang X, Murry CE, & Boyle PM (2023). "Graft–host coupling changes can lead to engraftment arrhythmia: a computational study." *The Journal of Physiology*. 2023 Jul;601(13):2733–49.
3. **Gibbs CE*** & Boyle PM. (2024). Population-Based Computational Simulations Elucidate Mechanisms of Focal Arrhythmia Following Stem Cell Injection. *Submitted*.
4. **Gibbs CE*** & Boyle PM. (2024) "Accelerated Intrinsic Beating Rate in Heterogeneously Coupled Cardiac Stem Cells May Underlie Focal Ventricular Tachycardia in Regenerative Therapy." *In preparation*.
5. Lee JD, Nguyen A, Jin ZR, Moghadasi A, **Gibbs CE**, Wait SJ, Evitts KM, Asencio A, Bremner SB, Zuniga S, Chavan V, Williams A, Smith N, Regnier M, Young JE, Mack D, Nance E, Boyle PM, Berndt A. (2024) ""Far-red and sensitive sensor for monitoring real time H2O2 dynamics with subcellular resolution and in multi-parametric imaging applications" *bioRxiv* doi: https://doi.org/10.1101/2024.02.06.
6. Yang J, Ochs A, **Gibbs CE**, & Boyle PM (2024) "Optogenetic stimulation of channelrhodopsins suppresses ectopic activity in computational models of cardiac stem cell therapy**"** *In preparation.*

* Indicates first author

Highlighted Abstracts and Presentations

- "*Accelerated Intrinsic Beating Rate in Heterogeneously Coupled Stem Cells May Underlie Focal Ventricular Tachycardia in Regenerative Cardiac Therapy*" (2024, October 24th) Talk presented by Dr. Patrick Boyle at Biomedical Engineering Society Conference, Baltimore, MD.
- *Individual Graft Spatial Features Reveal Mechanisms of Focal Arrhythmia Following Cardiac Stem Cell Therapy in Population-Based Computational Simulations*" (2024, September 20th) 2024 Carnegie Mellon Forum on Biomedical Engineering. Online
- "*Graft interactions can impact potential arrhythmogenicity of stem cell therapy*" (2024, January 11th) Poster Presentation. Cascadia 5.0, Vancouver, BC, CA
- "*Multiple Graft Interactions Increases Engraftment Arrhythmia Propensity: A Computational Study*" (2023, October 14th). Poster Presentation at Biomedical Engineering Society Conference, Seattle, WA
- *"Changes in Graft-Host Coupling Can Lead to Engraftment Arrhythmia: A Computational Study"* (2023, May 15th). Poster Presentation Bioengineering Cardiovascular Training Program Symposium, Seattle, WA
- *"Changes in Graft-Host Coupling Can Lead to Engraftment Arrhythmia: A Computational Study*". (2023, April 24-26th, 2023) Oral Presentation at Cardiac Physiome 2023, Irvine, CA
- "*Changes in Graft-Host Coupling Can Lead to Engraftment Arrhythmia: A Computational Study*" (2023, November 3 – 4th). Oral Presentation in the Rising Star Category at BC Regenerative Medicine Cascadia Corridor Research Symposium, Seattle, WA

Chapter 1: Benefits and Challenges of Cardiac Stem Cell Therapy

1.1 Introduction

Globally, ischemic heart disease continues to be a leading cause of death [1], manifesting as either myocardial infarction (MI) or ischemic cardiomyopathy [2]. During a MI, blood supply to the heart is reduced, leading to cardiomyocyte injury due to lack of oxygen [3]. For those that survive the initial MI, many patients still experience a decrease in quality of life [4]. This, in part, can be attributed to the heart's limited regenerative response [5]. Following an ischemic event, non-contractile collagenous scar tissue replaces damaged myocardium over multiple weeks [6]. While scar tissue helps maintain the structural integrity of the heart, it also leads to arrhythmias, adverse ventricular remodeling, and eventual heart failure (HF) (**Fig. 1.1**) [6–11]. Currently, treatment options address patients' symptoms but cannot restore the damaged myocardium apart from a heart transplant, where donors remain a limiting factor [12–14]. This has spurred many to research novel cardiac regenerative therapies to fulfill this need.

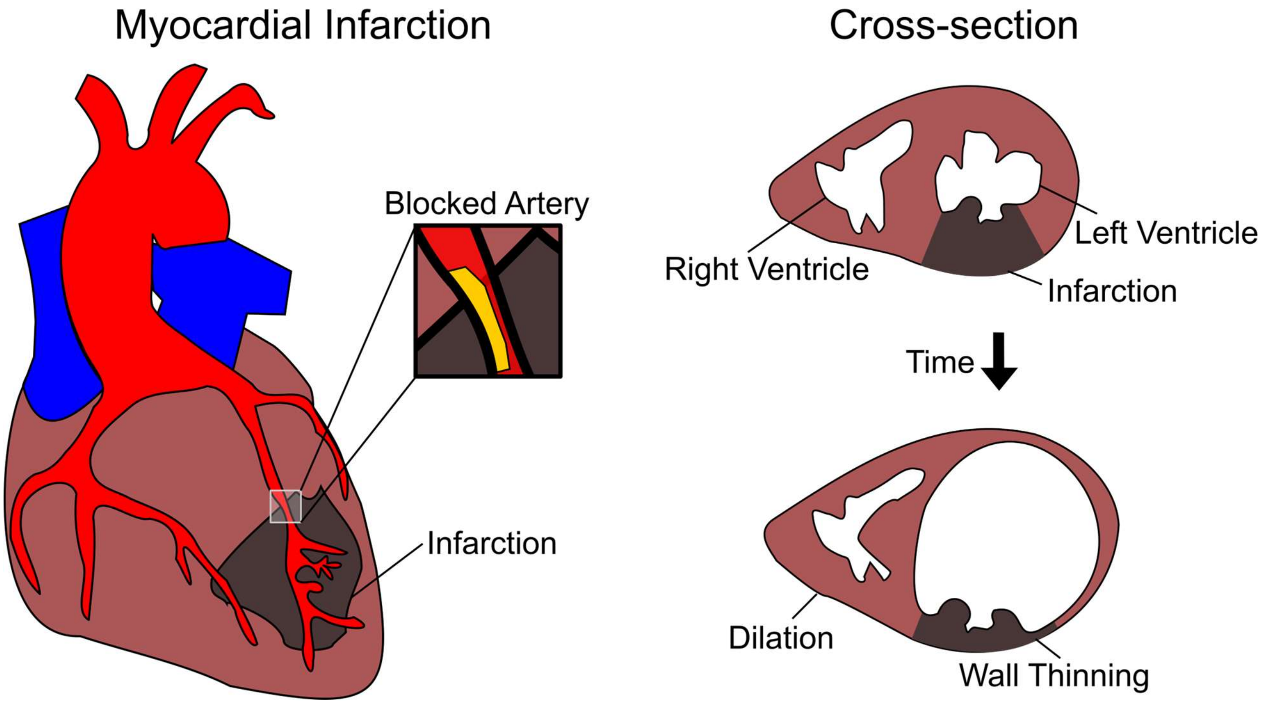

Figure 1.1: Myocardial infarction leads to left ventricular wall thinning and dilation.

Over the past two decades, many cell types have been tried as potential cell-based cardiac regenerative therapies, but none have been proven effective in human clinical trials as of 2024 [15]. More detailed reviews of these cells and their clinical trials can be found elsewhere [16–18]. This review highlights the use of human pluripotent stem cell-derived cardiomyocyte (hPSC-CM) as a cardiac regenerative cell therapy and the challenges that have arisen. We will also discuss the use of computational modeling to increase our mechanistic understanding of the electrophysiology of this proposed therapy.

1.2 HPSC-CMs Can Repair the Heart

In 1994, Soonpaa et al. discovered that fetal cardiomyocytes injected into the myocardium of mice could engraft and form intercalated disks with the adult cardiomyocytes, indicating electrical coupling [19]. These findings led to multiple decades of research to find a human cell type capable of cardiac regeneration [20,21]. Today, hPSC-CMs from either embryonic or human-induced origins have become a desired source for cardiac regenerative therapies due to the ability of stem cells to endlessly self-renew and differentiate into desired cell types, such as cardiomyocytes (**Fig. 1.2**) [22,23].

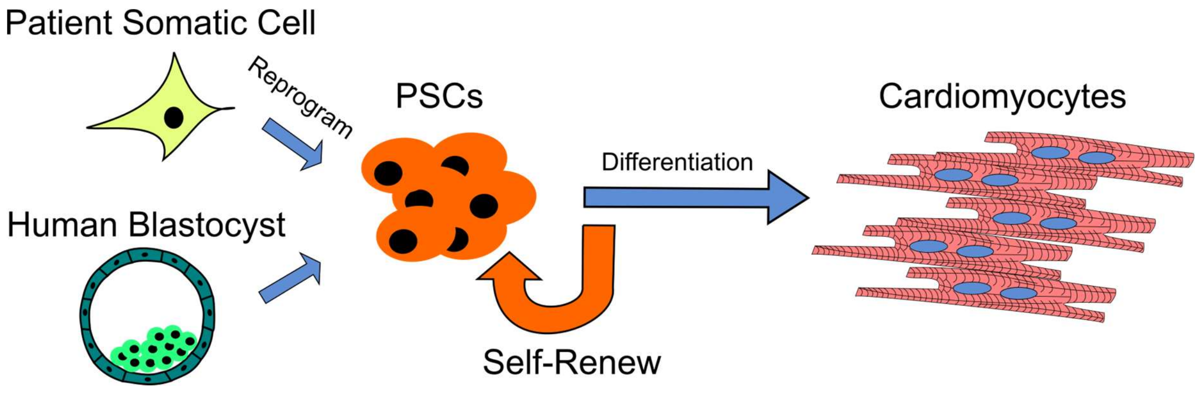

Figure 1.2: hPSC-CM can come from differentiating either a patient's somatic cells that are reprogrammed into a stem cell (hiPSC) or from a human blastocyst where embryonic stem cells (hESC) are isolated.

1.3 Transplantation Methods

Multiple transplantation strategies have been explored, including intravenous injection, intracoronary injection, tissue patches, and cardiomyocyte spheroids [20,24–28]. Epicardial patches and intramyocardial injections are the most popular and well-studied approaches [24,29–33]. This review will focus on engineered cardiac tissue patches and intramyocardial injections (Fig 1.3).

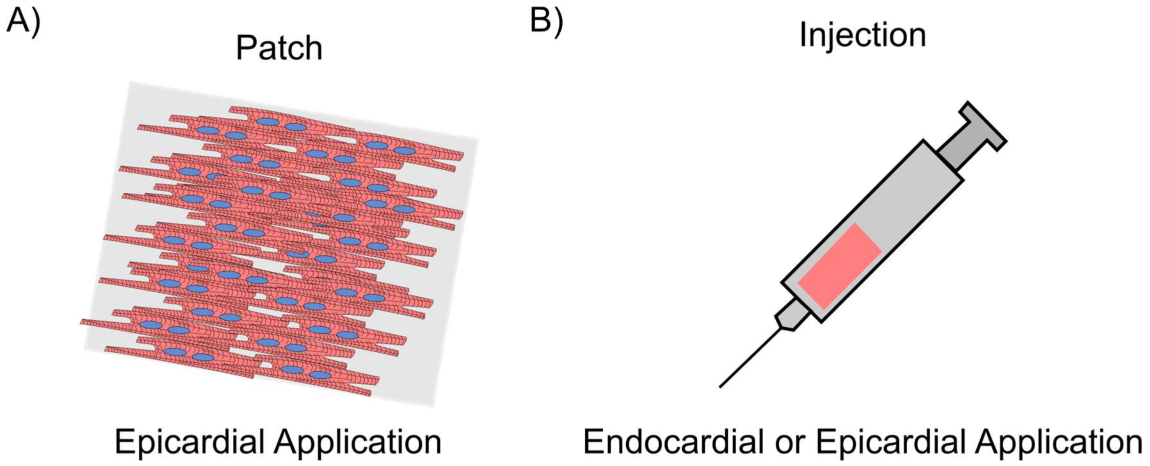

Figure 1.3: Two of the common methods of used for cardiac stem-cell therapy are cardiac patches and injections *A) Cardiac tissue patches are applied to the epicardial surface. B) Cardiac injections can be administered to either the endocardium or epicardium.*

1.3.1 Engineered Cardiac Tissue Patches

A cardiac tissue patch is an organized collection of cardiac cells grown in a lab that function as a tissue-like structure capable of generating contractile force [34]. While there are many types of cardiac tissue patches, we will focus on engineered heart tissues (EHT) and cardiac cell sheets. EHTs are 3D structures made by casting cardiac cells and a biomaterial scaffold into molds to form a tissue [29]. Cell sheets, on the other hand, are made up of confluent monolayers cultured on temperature-sensitive polymers that allow sheets to be released without the need for enzymatic digestion or scaffolding [35]. These intact monolayers can then be stacked to form 3D tissues with preserved cell-to-cell attachment [36]. Both EHTs and cell sheets have been shown to improve cardiac function following MI in multiple animal models [29,37–41]. One of the significant advantages of cardiac tissue patches is tissue engineering techniques are used to manipulate the cell microenvironment to create functional cardiac tissues composed of multiple cell types [42]. Electrical and mechanical stimulation can also be applied to increase cell alignment and improve mechanical and electrical properties [43–45]. Some work has been done to create parches that One of the disadvantages of using a patch is it requires more invasive surgical placement. Most patches are applied to the epicardial wall and are attached using sutures or adhesive. This can create a fibrotic layer between the patch and host myocardium, preventing electrical integration [20,29,46]. At this time, it is unknown how detrimental the lack of electrical integration may be. It has also be observed by some using this method that cells do not survive past 30 days but still provide a physiological benefit [47,48]. Thus, more work is needed to identify the exact mechanism for the observed cardiac improvement.

1.3.2 Intramyocardial Injection

Transplantation of hPSC-CMs using dispersed cell suspensions injected via a needle into damaged myocardium is another method that has been well-established in multiple pre-clinical animal models [49–53]. In these models, the cells can partially remuscularization and restore some cardiac function following an acute MI [49–56]. One significant advantage of this approach is its simplicity [37]. This methodology can be applied to a wide variety of patients because it can be administered using a catheter-based system or through epicardial injections [46,49,51,55]. Additionally, injecting cells directly into the host myocardium has been shown to facilitate electromechanical coupling between hPSC-CM grafts and host myocardium, which may prove advantageous [46,49,50,54]. One disadvantage of this technique is that only a small fraction of cells injected into the myocardium survive and engraft due to an initial cell die-off and washout

[57]. Pro-survival cocktails have been created to improve cell viability [57]; however, large quantities of cells may still be needed to achieve a clinically relevant dose. Various cell doses have been tested in a variety of animal models. To our knowledge, the highest dose that has been tested was over 1 billion cells injected in non-human primates (NHPs). This amount resulted in extensive engraftment and promising remuscularized host myocardium that could be translated to patients [50].

1.3.3 Human Clinical Trails

As of 2024, four human clinical trials are taking place in the US, Japan, and China using hPSC-CM injections [58–61]. All four trials are being conducted in chronic heart failure patients with a left ventricular ejection fraction of less than 45%. Interestingly, the doses reported are also lower than those that have been tested in animal models (Table 1.1).

Trial Name	**Clinical Trials ID**	**Location, Sponsor**	**Patient Population**	**Cell Dosage and Type**
A Study of iPS Cell-derived Cardiomyocyte Spheroids (HS-001) in Patients With Heart Failure (LAPiS Study) [58]	NCT04945018	Japan, Heartseed Inc	Severe HF secondary to MI	50/100 million (M) hiPSC-CM spheroids injected via spheroids dedicated needles for implantation and guided adaptors
Human Embryonic Stem Cell-Derived Cardiomyocyte Therapy for Chronic Ischemic Left Ventricular Dysfunction (HECTOR) [59]	NCT05068674	USA, Stanford Hospitals and Clinics	Chronic Ischemic Left Ventricular (LV) Dysfunction secondary to MI	hESC-CMs 50 M, 150 M, or 300 M cells delivered over 10 injections
Treating Heart Failure With hPSC-CMs (HEAL-CHF) [60]	NCT03763136	China, Help Therapeutics	Chronic LV dysfunction and indication for coronary artery bypass grafting (CABG)	Injection of 200 million allogenic hiPSC-CMs during CABG procedure
Treating Congestive HF With hiPSC-CMs Through Endocardial Injection [61]	NCT04982081	China, Help Therapeutics	Progressive heart failure patients who have received regular treatment	100/400 M allogenic iPSC-CMs delivered via transcatheter endocardial injection

Table 1.1: Clinical trials using hPSC-CM to treat heart failure

1.4 Challenges

1.4.1 Maturity

The inability to uniformly control the maturation of hPSC-CMs remains a significant concern for cell-based cardiac regenerative therapies. When differentiating hPSC-CMs *in vitro*, the media lacks the physical and environmental cues to homogenize the population, resulting in cells with varied shapes, sizes, and electrical properties [62]. When comparing adult ventricular cardiomyocytes and hPSC-CMs, the expression level of primary ionic current differs. For example, hPSC-CMs can spontaneously beat due to high levels of “funny” current (I_f) and lower levels of inward rectifier potassium current (I_{K1}), leading to a more positive (-60 mV) minimum diastolic potential (MDP). Adult ventricular cardiomyocytes, on the other hand, are quiescent and only electrically excited when depolarization of a neighboring cell causes the membrane of the next cell to reach the activation threshold [62]. The resting membrane potential of adult ventricular cardiomyocytes is also much more negative (-90 mV). More detailed reviews of hPSC-CM maturity can be found elsewhere [62–64].

To overcome this lack of maturity, many researchers have tried various methods to promote maturation ranging from longer culture times, electrical stimulation, and alteration of the tissue culture environment. In a study by Herron et al., culturing hPSC-CMs on a soft polydimethylsiloxane (PDMS) surface enhanced the structural and functional maturity of the cells *in vitro* [65]. Using this idea, Dhahri et al. investigated how increasing hPSC-CM maturity could improve engraftment in a guinea pig MI model. They found that culturing their cells on PDMS-lined roller bottles before engraftment improved cardiomyocyte alignment, decreased hPSC-CM spontaneous electrical activity, increased gap junction formation with the host myocardium, and improved host-graft electromechanical integration compared to cells grown on tissue culture plastic alone [52]. These studies show one of many potential methods to improve the safety profile of hPSC-CM-based cell therapies, but evaluation of these methods in larger animal studies is needed.

1.4.2 Proarrhythmic Activity

Arrhythmias following the transplantation of hPSC-CMs are another major concern. In large animal models such as NHP and pigs, ventricular tachycardias (VT) have been observed following the injection of hPSC-CM. While VT can be well tolerated in NHPs [49,50], in pigs, it can lead to ventricular fibrillation and cardiac death [51,54]. These arrhythmias have impeded the translation to human clinical trials of large-dose hPSC-CM injections until a better safety profile can be established.

Recent attempts to make hPSC-CM injection safer have included pharmacologic treatment and genetic modifications to the hPSC-CMs. In a paper by Nakamura et al., clinically available antiarrhythmics were tested to mitigate the risk of VT in an infarcted pig model. After screening seven antiarrhythmics, the researchers found amiodarone and ivabradine to be the most promising drug candidates. Amiodarone is a class III antiarrhythmic drug that blocks the potassium channel. Ivabradine is a class 0 antiarrhythmic that inhibits pacemaker activity leading to heart rate slowing. All animals that received hPSC-CM developed VT; however, combining these two drugs in the treatment group enhanced survivability. This drug combination prevented cardiac death and unstable VT in all nine subjects compared to 3/8 in the untreated group [51]. These findings indicate that these two antiarrhythmics could help make hPSC-CM engraftment safer.

In another recent work by Marchiano et al., the authors hypothesize that spontaneous depolarizations within engrafted hPSC-CMs were the source of VT. To reduce VT burden, the authors sought to either knock out or overexpression ion channels to make the action potential of the hPSC-CMs more adult ventricular-like. They found that knocking out genes specific to funny channel (HCN4), T-type calcium (CACNA1H), and the sodium-calcium exchanger (SLC8A1) in combination with overexpression I_{K1} (KCNJ2) did not result in VT when injected into the myocardium of uninjured pig hearts [66]. While this study was not conducted in infarcted hearts, it showed promising results to increase the safety profile of this therapy and warrant further investigation.

1.5 Multiscale Computational Modeling of hPSC-CM and VT

While traditional experimental approaches are essential to understanding the effects of hPSC-CM as a stem cell therapy, computational models are another important tool that help us explain electrophysiology phenomena at multiple scales. Computational modeling allows for a multiscale approach with precise control over sub-cellar kinetics and tissue geometry. Using a system of ordinary differential equations (ODEs), individual ion channels and their kinetics can be represented at the sub-cellular scale. Mathematical cell scale model of the action potential (AP) for the different cell types, such as scar, adult cardiomyocytes, and hPSC-CMs can then be generated. These cell models can then be applied to tissue and organ meshes with patient-specific or prescribed geometries to investigate how tissue heterogeneity can affect arrhythmia propensity **(Fig. 1.4)** [67,68].

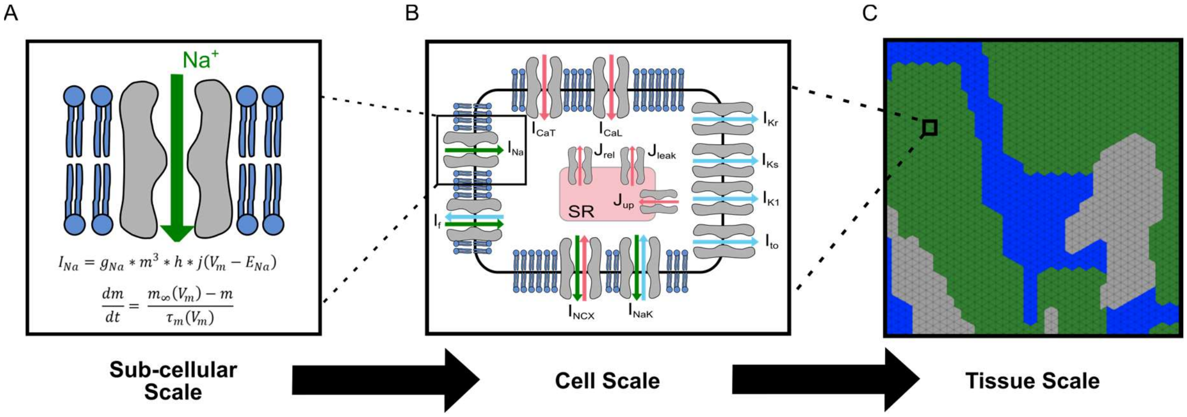

Figure 1.4: Hierarchy of multiscale electrophysiology modeling. *A) Representative image of modeling a sodium ion channel. Sample equations for a Hodgkin-Huxley formulation of rapid sodium current are shown. B) Schematics of a two-compartment ionic model. C) Heterogeneous spatial pattern of hPSC-CM graft (green), host myocardium (blue), and scar (grey).*

1.5.1 Cell Scale

At the cell scale, multiple hPSC-CM cellular ionic models have been created [69–71]. Paci et al. and its subsequent updates have created a two-compartment atrial and ventricular-like hPSC-CMs model using a single comprehensive data set [71–73]. Similarly, Kernik et al. created a two-compartment whole cell hPSC-CM electrophysiology model that leveraged multiple data sources and *in vitro* kinetics to better represent the diverse phenotypes found in experimental *in vitro* cell populations [69]. Koivumäki et al. created a more biophysically detailed hPSC-CM model to more realistically represent calcium handling and dynamics [70]. However, this model is relatively computationally expensive, limiting its scalability to the tissue and organ scale simulations [74].

1.5.2 Tissue and Organ Scale

The arrhythmogenic effects of engrafted hPSC-CMs have also been investigated at the tissue and organ scale. Yu et al. created a multi-scale modeling framework to study focal and macro-reentrant mechanisms of VT in human ventricular MI models [75]. To model VT from injected hPSC-CMs, a heterogenous spatial distribution was created by varying the volume of tissue occupied by hPSC-CMs and the number of clusters generated. They found that focal VT from intramyocardial injection was highest when the cell dose and the number of clusters were high and delivered at the infarct boundary. This study also modeled hPSC-CM cell sheets applied to the epicardial surface and found the sheet could function as a substrate for reentry, where pre-treatment reentry was not observed [75].

In the follow-up study, Yu et al. explored both focal and re-entrant VT mechanisms resulting from remuscularization via an hPSC-CM patch in post-MI human heart models [76]. They found reentrant drivers dominated over focal mechanisms. Graft automaticity was suppressed by sinus rhythm, leading the authors to conclude that focal sources are unlikely to contribute to VT in their models. They also explored how patch location affected VT burden in patient-specific post-MI substrates. Some areas drastically elevated VT inducibility and burden, while others did not [76].

In another recent study, Yu et al. created a new biophysically detailed computational model of the intercellular junctions between graft and host cells to assess focal VT mechanisms (66) further. This study examined the consequences of different graft conductivities and found that ectopic beat propagation was reduced by increased coupling between graft and host. However, the observed ectopic beats never exceeded the intrinsic automaticity rate of ~96 bpm. Due to this slow graft-induced focal beating rate, the authors concluded that a reentrant driver mechanism is more likely to contribute to the clinically observed rapid VT [77].

In a different study, Fassani et al. created a framework to look at various EHT patch design components that could influence electrical activation. This study found that EHT patch conductivity was the main parameter influencing electrical propagation. A physiologic activation pattern could also be achieved by increasing the conductivity of the patch; however, it could promote proarrhythmic behavior [78].

Work from our lab and the focus of this dissertation has been to create a computational framework for testing and understanding focal arrhythmia mechanisms following the engraftment of hPSC-CMs. In **Chapter 2,** we tested our hypothesis that VT may be explained partially by time-varying, spatially heterogeneous, graft-host electrical coupling using 2D histology-derived slice models. We found that our models could recapitulate the "wax and wane" phenomenon of VT as graft-host coupling progressively increased and that VT burden was reduced as cell-cell coupling within the graft was also increased [79]. In **Chapter 3**, we examined how different geometric combinations of grafts could affect the overall arrhythmogenic overserved in our simulations but symmetrically removing selected grafts from our slice models. We found that individual grafts in isolation can be arrhythmogenic but to varying degrees that appear to depend on the tortuosity of graft boundaries, graft-host proximity, and total graft area. In **Chapter 4**, we explore the impact that varied intrinsic hPSC-CM beating rates can have on VT inducibility in 2D human slice geometries.

Chapter 2: Graft-Host Coupling Changes Can Lead to Engraftment Arrhythmia[1]: A Computational Study

With text and figures from *Journal of Physiology* DOI: 10.1113/JP284244

2.1 Abstract

After myocardial infarction (MI), a significant portion of heart muscle is replaced with scar tissue, progressively leading to heart failure. Human pluripotent stem cell-derived cardiomyocytes (hPSC-CM) offer a promising option for improving cardiac function after MI. However, hPSC-CM transplantation can lead to engraftment arrhythmia (EA). EA is a transient phenomenon arising shortly after transplantation then spontaneously resolving after a few weeks. The underlying mechanism of EA is unknown. We hypothesize that EA may be explained partially by time-varying, spatially heterogeneous, graft-host electrical coupling. Here, we created computational slice models derived from histological images that reflect different configuration of grafts in the infarcted ventricle. We ran simulations with varying degrees of connection imposed upon the graft-host perimeter to assess how heterogeneous electrical coupling affected EA with non-conductive scar, slow-conducting scar, and scar replaced by host myocardium. We also quantified the effect of variation in intrinsic graft conductivity. Susceptibility to EA initially increased and subsequently decreased with increasing graft-host coupling, suggesting the wax and wane of EA is regulated by progressive increases in graft-host coupling. Different spatial distributions of graft, host, and scar yielded markedly different susceptibility curves. Computationally replacing non-conductive scar with host myocardium or slow-conducting scar, and increasing intrinsic graft conductivity, both demonstrated potential means to blunt EA vulnerability. These data show how graft location, especially relative to scar, along with its dynamic electrical coupling to host, can influence EA

---

[1] Engraftment arrhythmia (EA) is a term that some labs use to refer to VT following stem cell engraftment

burden; moreover, they offer a rational base for further studies aimed to define the optimal delivery of hPSC-CM injection.

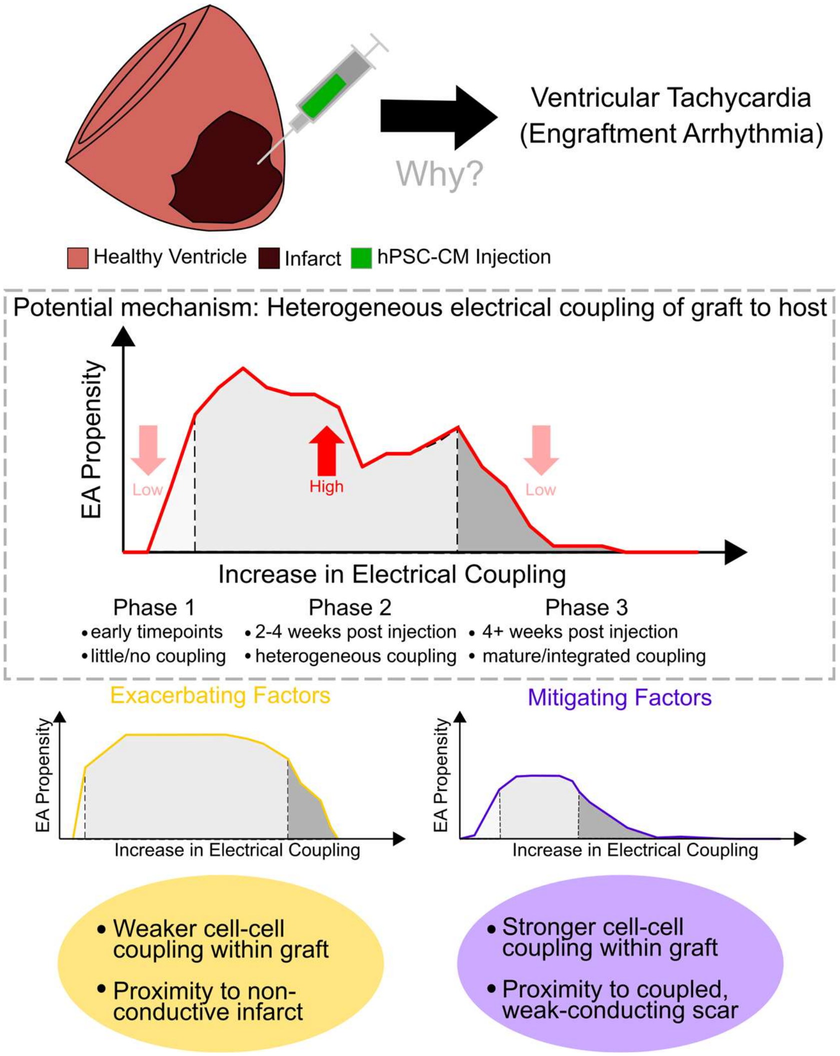

2.0 Graphical Abstract: *EA following hPSC-CM injection can be explained in part by spatially and temporally heterogeneous graft to host electrical coupling. EA propensity can be exacerbated by weak intra-graft cell-cell coupling or by graft proximity to non-conductive infarct; conversely, it can be mitigated by graft proximity to weak-conducting scar or by strong intra-graft cell-cell coupling.*

2.2 Introduction

Myocardial infarction (MI) is a global health burden and the leading cause of death worldwide [80]. The regenerative capacity of the human heart decreases soon after birth [5,81], and muscle tissue lost after MI is replaced by non-contractile scar tissue [6,11,82]. This leads to detrimental structural remodeling and heart failure (HF), which is common following MI [80,83–85]. Current HF treatment options focus on symptom management and delaying disease progression, but these strategies fail to solve the underlying issue of damaged myocardium, namely replacement of functional myocardium with fibrosis [86]. Heart transplantation remains the ultimate option, but this procedure is limited by the number of donor hearts available [12]. Thus, there is a pressing need for regenerative-based cardiac therapies [87,88].

Human pluripotent stem cell-derived cardiomyocytes (hPSC-CM) represent a promising candidate for cardiac regenerative cell-based therapies. Pre-clinical studies have shown that hPSC-CM limited adverse remodeling of the heart while also improving ventricular function [52,53,87–89]. However, after transplantation in large animal models (e.g., pigs and non-human primates [NHP]), this therapeutic approach leads to transitory but serious cardiac arrhythmias, defined as engraftment arrhythmia (EA) [49–51,54,90]. Electrical mapping studies suggest EA is focal in nature, with ectopic excitations originating at the sites of hPSC-CM implantation [49,51,54,91]. This notion agrees with the immature profile of hPSC-CM that, like embryonic cardiomyocytes, exhibit automaticity (i.e., the ability to spontaneously depolarize and generate action potentials) [62,92,93]. EA burden becomes detectable as graft starts to electromechanically couple with host cells (within ~1 week), and it peaks to occupy > 50-75% of day, around two-weeks post-treatment. These arrhythmias persist for multiple weeks while the burden progressively wanes before resolving [49,54]. It is still mechanistically unclear, however, how spontaneous excitations in a relatively small number of transplanted hPSC-CM can serve as a rapid-firing bioelectric source that elicits propagating responses in the dense, well-coupled current sink of host myocardium. Previous studies have shown that expression of the proteins mediating mechanical and electrical coupling between host myocardium and grafts, such as N-cadherin and connexin43, are progressively up-regulated and localized to nascent intercalated disks with maturation. In turn, maturation is accelerated after *in vivo* transplantation, compared to *in vitro* culture [56,62,94]; however how this upregulation in proteins is related to EA propensity remains poorly understood.

Computational cardiology has emerged as a useful tool to gain mechanistic insights into arrhythmia initiation and perpetuation at various spatial scales [78,95,96]. Cell-, tissue-, and organ-scale computational models have helped to understand arrhythmias in ways difficult to achieve through traditional experimental or clinical techniques [97–99]. Prior computational modeling work suggests reentrant mechanisms may play a role in EA onset [75,77], but those studies assumed a continuum of graft-host electrical coupling and were unable to recapitulate the key observation from pre-clinical animal studies that showed EA is focal in nature. The development of histology-based computational tools that can reconcile this apparent contradiction will lead to a better understanding of EA and may lead to new strategies for mitigating side effects in cell-based heart regeneration therapies.

In this study, we created computational models from 2D-histological images of engrafted hPSC-CM to better represent the spatial distribution of graft, host, and scar tissue. Simulations were conducted in these models to assess how heterogeneous graft-host electrical coupling affects EA propensity. Specifically, we examined the role played by spatiotemporal evolution of coupling along boundaries between hPSC-CM and host myocardium regions. We hypothesized that temporal dynamics of EA in pre-clinical studies (i.e., delayed onset post-engraftment, eventual resolution) can be explained partially by the formation of graft-host electrical connections in a gradual, spatially heterogeneous manner. To model this, we used ventricular slice models derived from histological images [49], and stochastically modified graft-host coupling patterns to comprehensively test thousands of plausible combinations. In each configuration, EA propensity, intended as the possibility of graft-host ectopic excitation, was evaluated during its evolution: from the time of hPSC-CM injection to fully integrated grafts. Finally, we examined how the presence or absence of scar tissue modified graft arrhythmogenicity in the same ventricular slice models.

2.3 Methods

2.3.1 Ethical Approval

The histology images used in this study were derived from infarcted macaque hearts that came from a previous study [49]. All procedures and protocols used for the animals in that study complied with the NIH Guidelines for the Care and Use of Laboratory Animals and the Animal Welfare Act. Ethical approval was obtained from the University of Washington Animal Care and Use Committee. Animals are housed in the primate center facility of the University of Washington Department of Comparative Medicine and monitored by University of Washington's staff veterinarians. All activities involving animals are reviewed and approved by the University of Washington's Institutional Animal Care and Use Committee (IACUC, protocol number 448602).

2.3.2 Histology-based slice models

Five unique histology images from post-MI ventricles of two macaque NHPs three months following hPSC-CM injection were used to reconstruct two-dimensional slice models [49]. Models 1-2 came from one NHP; Models 3-5 came from a second animal. The histology approach has been described previously [49]. Briefly: human cardiac troponin I staining was used to visualize hPSC-CM graft; picrosirius red and fast green stains were used to delineate regions of collagen (i.e., infarct or scar, red), and healthy myocardium (green), respectively **(Fig. 2.1 A).** Images for each stain were aligned in imaging software (GNU Image Manipulation Program) and color thresholding was used to create four bins (graft, scar, myocardium, non-cardiac) **(Fig. 2.1 B)**. Thresholded images were loaded into 3D modeling software (Blender). Using the thresholded images as a reference, slice models were constructed using triangles with an edge length of ~50 µm. Each region (graft, host, and scar) was assigned to its respective vertex groups. Finally, the points interconnected by region-labeled triangles were exported, then converted to a format compatible with our finite element modeling software **(Fig. 2.1 C)**. The number of nodes and triangular finite elements for each model can be found in Table 1.

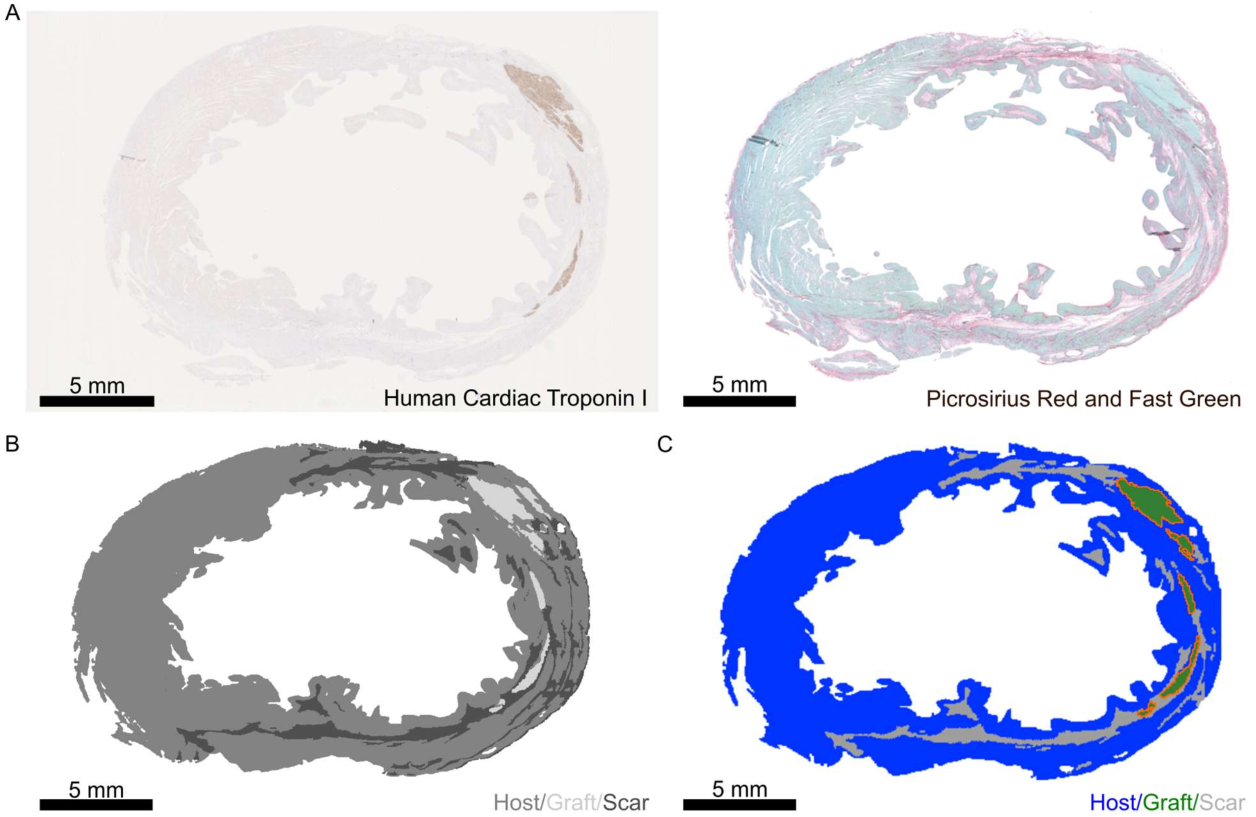

***Figure 2.1: Deriving slice models from histological images of post-MI macaque ventricles**. A) Example histology images used to generate slice model. Left: Human Cardiac Troponin I stained for graft. Right: Fast Green stained for myocardium and Picrosirius Red stained for collagen (i.e., scar). B) Example thresholded image. Areas that are within the tissue boundary but are delineated as neither scar nor graft are deemed host myocardium. C) Example slice model with grafts outlined in orange. All scale bars: 5 mm.*

	Number of Nodes	Number of Elements
Model 1	52446	103523
Model 2	80419	158908
Model 3	67061	131027
Model 4	52823	103135
Model 5	47193	92475

Table 2.1: Finite element mesh properties for models used in this study.

Myocardial fibers are helically wound within the ventricular wall, with fiber axes ranging from –60° at the endocardium to +60° at the epicardium relative to the transverse short axis. Histological sections here were taken after sectioning the heart in the transverse plane, from the apex to the base; this poses a substantial challenge in reconstructing the orientation of the fibers from histology images [100,101]. For this reason, we used a mathematical approximation to represent idealized fibrous structure for each slice model used in this study. Our guiding assumption was that fibers should be tangential to the surface at the epicardial and endocardial walls and vary smoothly in between. First, we solved the Laplacian equation ($F = \nabla^2 \phi = 0$) with Dirichlet boundary conditions imposed at the endocardium ($\phi = 0$) and epicardium ($\phi = 1$). Second, we calculated the gradient of this field (∇F) to produce a map of radial vectors on each triangle in the model domain. Finally, we rotated these element-wise vectors 90º in-plane to produce the field approximating myocardial fiber orientations (see examples in **Figs. 2.2A-B**).

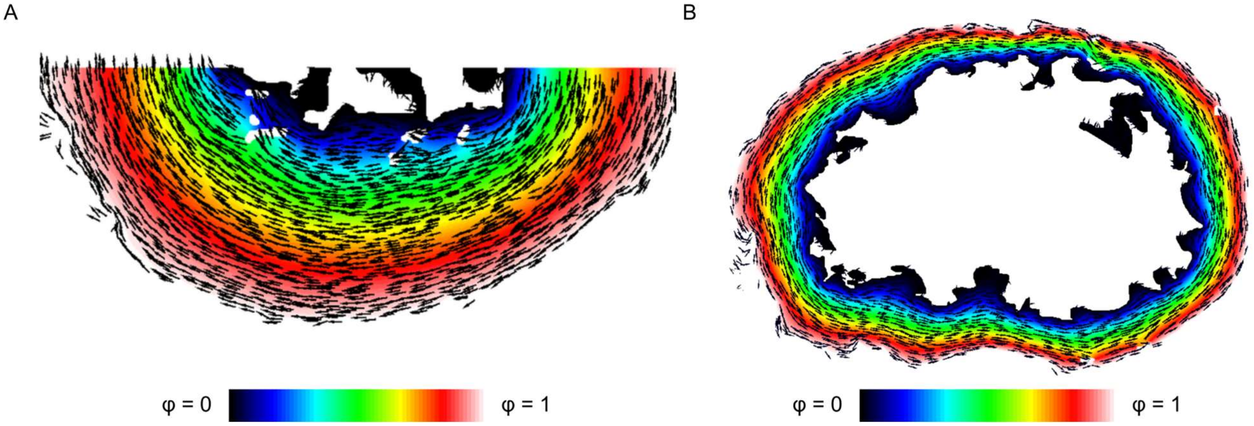

Figure 2.2: Illustration of the process used to map myocardial fiber orientations into each model. *Vectors (black arrows) show fiber orientations calculated using the Laplacian-based approach (see text). Color map shows the solution to the Laplacian problem with boundary conditions imposed on the endocardial (φ = 0) and epicardial (φ = 1) surfaces. A) Model 1. B) Model 3.*

2.3.3 HPSC-CM differentiation and characterization by RTqPCR

RUES2, a human embryonic stem cell (hESC) line, was differentiated into CMs (hESC-CMs) through small molecules that modulate Wnt pathway: briefly, hESCs are treated with CHIR99021 (Wnt agonist) to initiate direct differentiation and the Wnt antagonist WNTC59 to induce cardiomyocytes state after mesoderm formation [102]. Fourteen days after the induction of cardiac differentiation, RNA from hESC-CMs was harvested using RNAeasy Mini kit (QIAGEN) according to manufacturer’s instruction. RNA was then retro-transcribed using M-MLV RT kit (Thermofisher), and RT-qPCR was performed with SYBR Select Master Mix (Applied Biosystem). Reactions were run on a CFX384 Real-Time System (Biorad), and data were analyzed using the ΔΔCt method using HPRT1 (hypoxanthine-guanine phosphoribosyl transferase 1) as the housekeeping gene. Primers were designed using PrimerBlast and confirmed to amplify a single product. Primer sequences (5’ → 3’): *HPRT1* (FWD: TGACACTGGCAAAACAATGCA, RVS:

GGTCCTTTTCACCAGCAAGCT); *KCNJ2* (FWD: GTGCGAACCAACCGCTACA, RVS: CCAGCGAATGTCCACACAC); *HCN4* (FWD: GATCCTCAGCCTCTTACGCC, RVS: CCCCAGGAGTTGTTCACCAT); *SLC8A1* (FWD: AGACCTGGCTTCCCACTTTG, RVS: TGGCAAATGTGTCTGGCACT).

2.3.4 Modeling of Varied Graft-Host Coupling

We modeled differences in graft-host coupling using a discontinuous finite element method [103]. From the starting point of a continuous boundary that uniformly allows passage of electrical current between graft and surrounding tissue, a subset of edges shared between graft and host finite elements (triangles) is identified for disconnection. For this part of the boundary, finite element edges and nodes are duplicated such that current flux between the adjacent triangles is no longer possible (**Fig. 2.3 A**). Since the timing and spatial pattern with which graft-host coupling evolves during engraftment is not well understood, we used a stochastic approach to examine a wide variety of potential electrical coupling configurations. In each model, for 24 distinct values of graft-host connectedness level (p_c) – 2.5% to 60% in steps of 2.5% – we used random edge selection to generate 40 unique variants in which exactly that proportion of boundaries were disconnected (see examples in **Fig. 2.3 B**). p_c values above 60% were never tested since graft-host excitation was never observed in that parameter range. The p_c constraint was imposed on a graft-by-graft basis (i.e., in a model with several distinct “islands” of graft, the same proportion of boundary was modeled as electrically conductive in each of them).

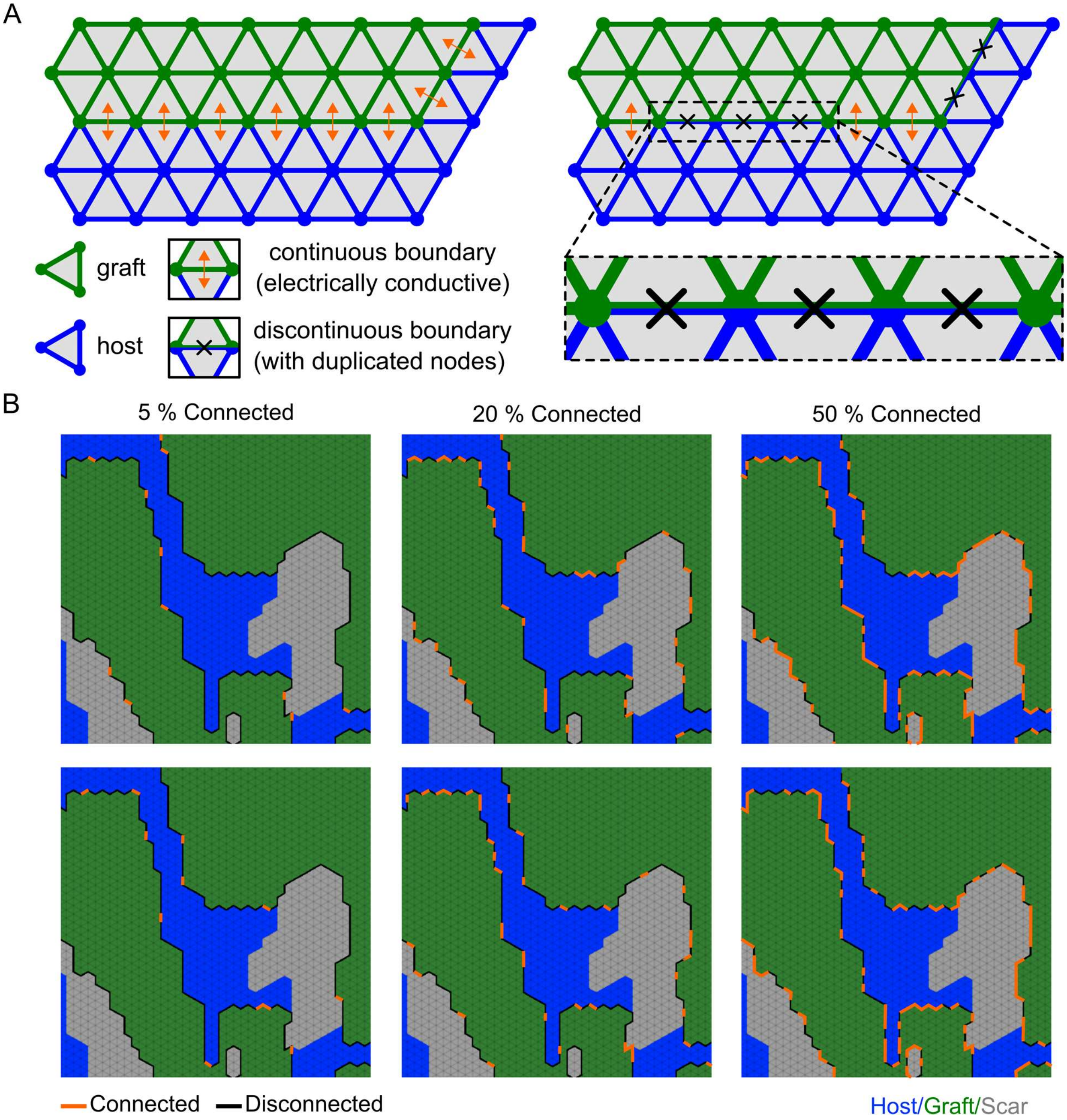

Figure 2.3: Schematic of how graft-host coupling was varied. *A) Schematic illustrating continuous vs. discontinuous finite element modeling. B) Two example permutations each are shown for* p_c *levels of 5%, 20%, and 50% connected. Each image has regions of graft (green), host (blue), and scar (grey) labeled. Edges of graft connected to surrounding tissue are shown with orange lines and edges that are disconnected are shown with black lines.*

2.3.5 Cell- and tissue-scale electrophysiological modeling

In graft tissue regions, we used an existing model of hPSC-CM membrane kinetics [69] with two modifications (**Fig. 2.4 A**). These modifications were motivated by several experimental observations. First, EAs originate from graft and cause heart rates much faster (>5Hz) than the intrinsic rate of the Kernik model (1.1 Hz) or published experimental *in vitro* data [49,54,70]. Second early stage hPSC-CM, similar to those used in transplanted hearts, have a less negative minimum diastolic potential ([MDP] between -68 mV and -57 mV) [62,94] compared to the Kernik model (MDP = -75.826 mV). Lastly, our *in vitro* hPSC-CM, analyzed by real-time quantitative PCR (RTqPCR), showed low expression of *KCNJ2* (the gene encoding for Kir2.1, the channel corresponding to inward rectifier potassium channel (I_{K1}); **Fig. 2.4 B**), compared to *HCN4*, *CACNA1H* (encoding for Cav3.2), and *SLC8A1* (encoding for NCX1). All three of these channels are involved in AP formation in immature cardiomyocytes [62,92,104]. This observation is consistent with prior work showing that inward rectifier potassium channel (I_{K1}) is barely detectable in immature cardiomyocytes, like hPSC-CM [62,105]. Accordingly, we removed I_{K1} from the model and doubled the conductance associated with the *HCN4*-mediated "funny" current (I_f). The latter change was motivated by the fact that I_f is among the most important drivers of pacemaker activity and controls the diastolic membrane potential, together with I_{K1} [106–108]. These two changes led to a markedly faster spontaneous beating rate (~1.9 Hz), but the effect on MDP was less dramatic (-72.096 mV; **Fig. 2.4C**). We modeled membrane kinetics of host myocardium using the Ten Tusscher et al. human ventricular ionic model [109] since there is no published model of NHP cardiomyocyte electrophysiology. For ease of reproducibility, all cell-scale initial conditions were identical to those used in the published version of the Kernik et al. model.

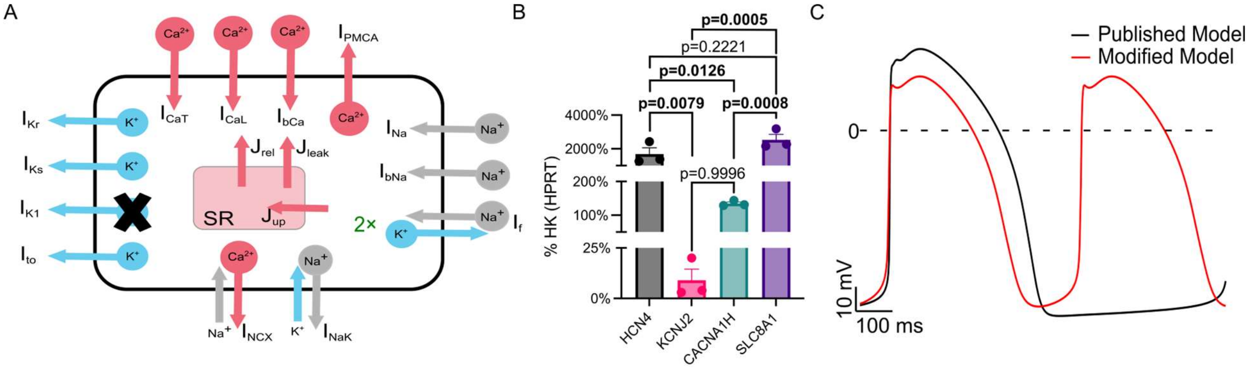

__Figure 2.4: Modifications made to published hPSC-CM model.__ A) Schematics showing modifications made to ionic model. I_{K1} was blocked and I_f was doubled. B) RTqPCR analysis of wild type hPSC-CMs at day 14 after differentiation. Data shown as mean (SD) of 3 independent biological replicates. HK = Housekeeping gene. Statistical differences are reported by one-way ANOVA with Sidak correction. Bolded p values denote statistical significance. C) Action potential traces of published model (black) compared to modified model (red). The spontaneous beating rate of modified model showed an increased beating rate of 1.9 Hz compared to 1.1 Hz in the published model.

At the tissue scale, a finite-element approximation of the monodomain formulation was used to govern the propagation of electrical activity [110,111]. Partial differential equations were solved to describe electrical current flow in the myocardium; ordinary differential and algebraic equations were solved to represent membrane kinetics (as described in the preceding section) at each finite-element node. This approach has been used in many other studies examining cardiac arrhythmia mechanisms [112–115]. As in prior work [98], conductivity tensor values in the longitudinal and transverse directions with respect to fiber orientation were set to $\sigma_L = 0.255$ S/m and $\sigma_T = 0.0775$ S/m, respectively. hPSC-CM graft islands were modeled with isotropic conductivity (i.e., no difference between longitudinal and transverse directions). Since intra-graft conduction velocity in hPSC-CM islands remains poorly characterized but is presumed to be slower than in the longitudinal direction in host myocardium [52], we assigned a baseline conductivity value identical to σ_T (i.e., $\sigma_{hPSC\text{-}CM}$ = 0.0775 S/m). We ran additional simulations with this parameter adjusted by 4×, 2×, ½×, or ¼× to examine a range of plausible conditions. Scar was modeled either as a non-conductive insulator [116] or as slow-conducting passive tissue (i.e., pure electrical sink) [78,117]. To avoid spurious scar-to-host excitations from electrotonic current, we set the resting potential of slow-conducting scar to match that of the human ventricular ionic model (–85.8 mV) [109]. Additionally, we sought to explore how the absence of infarct might influence EA propensity. In these cases, cell- and tissue-scale electrophysiological properties of regions previously tagged as “scar” were indistinguishable from host myocardium. In all simulations, no external pacing was applied. To summarize each model’s EA susceptibility, we extracted metrics from graphs of EA incidence as a function of coupling: area under the curve (AUC) to quantify EA burden; window of vulnerability (WOV) to reflect the range of p_c values within which EA occurred.

2.3.6 Identifying earliest activation sites

For each simulation resulting in graft-initiated host excitation, we identified the earliest activation sites that led to full-blown propagating wavefronts in the host myocardium. To do this, we identified the time at which activation occurred distal to the graft and worked backward to identify the origin. This approach avoided incorrect identification of false positive breakthrough sites where spontaneous activity in the graft caused subthreshold depolarization in coupled host tissue.

2.3.7 Computational resources

This work was facilitated through the use of advanced computational, storage, and networking infrastructure provided by the Hyak supercomputer system at the University of Washington. Simulations of bioelectrical activity were conducted using openCARP [118] and the resulting data were visualized using the meshalyzer tool by Dr. Edward J. Vigmond; both of the latter are freely available for non-commercial reuse (see: http://opencarp.org/).

2.3.8 Statistics

For the in vitro experiment (RTqPCR Fig. 2.4B), the number of biological replicates is intended as independent batches of hPSC-CM differentiation. For multiple group comparison, one-way ANOVA with Sidak correction was used as statistical analysis. Difference was considered statistically significant when $p < 0.05$.

2.4 Results

2.4.1 Arrhythmogenic propensity as a function of graft-host coupling

We first wanted to understand graft behavior in the context of full isolation from (connectedness level [p_c] = 0% connected) or full coupling (p_c = 100%) with the surrounding myocardium. When fully decoupled, isolated grafts beat spontaneously but never initiated a response in the host **(Fig. 2.5 A)**. When grafts were fully connected to surrounding tissue, spontaneous depolarization was suppressed due to dissipation of excitatory current in the well-coupled electrical sink of surrounding myocardium [119]. As shown in **Fig. 2.5 B**, the tissue quickly returned to a quiescent state. We then tested many intermediate configurations of partial graft coupling that created a milieu in which graft-initiated host excitation occurred. **Figure 2.5 C** shows an illustrative example where a p_c = 5% gave rise to conditions favorable to graft-initiated host excitation. For the example shown, the leading pacemaker site was in the upper right-hand corner of the large graft, and the resulting wavefront followed the path indicated by the blue arrow before breaking through into host myocardium (white asterisk).

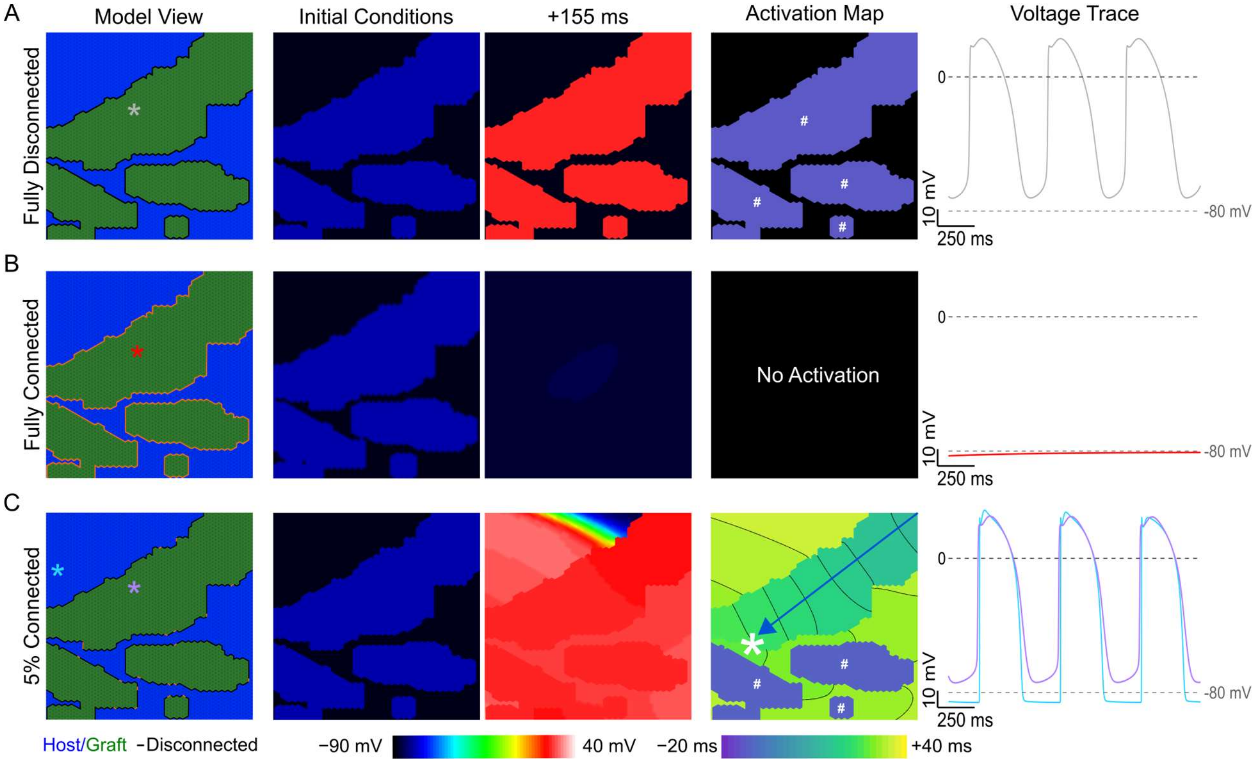

Figure 2.5: Fully coupled graft-host myocardium does not facilitate any graft-initiated host excitation. *A) Fully isolated grafts beat spontaneously in isolation. B) Grafts fully coupled to host myocardium, showed impaired propagation due to dissipation of spontaneous depolarization originating from graft into surrounding myocardium. C) When graft is 5% coupled to host myocardium graft-initiated host excitation occurs (white asterisk). Column 1 shows the labeled model with colored asterisks denote the location of voltage traces shown in column 5. Column 2 shows voltage initial conditions. Column 3 shows the voltage at +155 ms. Column 4 shows the activation map. Grafts that spontaneously excite in isolation before the lead pacemaker graft are denoted by the white colored # symbol. Blue arrow highlights wavefront path. Voltage traces are shown starting at t=500ms to highlight the equilibrium conditions after the initial conditions have resolved.*

Next, we examined the relationship between EA propensity and graft-host connectedness (i.e., p_c) in all five of our slice models. For this set of stimulations, the baseline graft conductivity value was kept at $\sigma_{hPSC\text{-}CM} = 1\times$ (see methods). Characteristics of each model can be found in **Table 2.2**. The total area of each model ranged from 1.0 – 1.7 cm^2. Models 1 and 2 contained a total graft area of ~0.27 cm^2 but the amount of scar in Model 2 was ~12× greater. Models 3 – 5 had roughly the same graft size and amount of scar. **Figure 2.6** shows a representative activation map for each model at 10% p_c for a case in which graft-initiated host excitation occurred (**Fig. 2.6, column 1**). In A, two grafts undergo spontaneous excitation but only the graft denoted with a grey asterisk orange dot successfully excited the host. The wavefront then propagated clockwise exciting both host and non-refractory graft. In B, most grafts were isolated in scar thus making only grafts in the low right corner capable of graft-initiated host excitation. In C, two of the four grafts underwent spontaneous excitation, but the uppermost graft is where graft-initiated host excitation was first to occur. Similarly to B and C, in D two grafts underwent spontaneous excitation but only one led to host excitation. In E, only the graft in the upper left was large enough to successfully excite the host.

	Total Graft Area (cm^2)	Total Scar Area (cm^2)	Graft-Scar Perimeter (cm)	Total Area of Model (cm^2)
Model 1	0.2675	0.0661	2.2367	1.1150
Model 2	0.2664	0.7866	10.9174	1.7629
Model 3	0.0477	0.1550	0.7910	1.4536
Model 4	0.0691	0.1686	0.9079	1.1442
Model 5	0.0344	0.1598	0.6759	1.0259

Table 2.2: Computational slice model characteristics

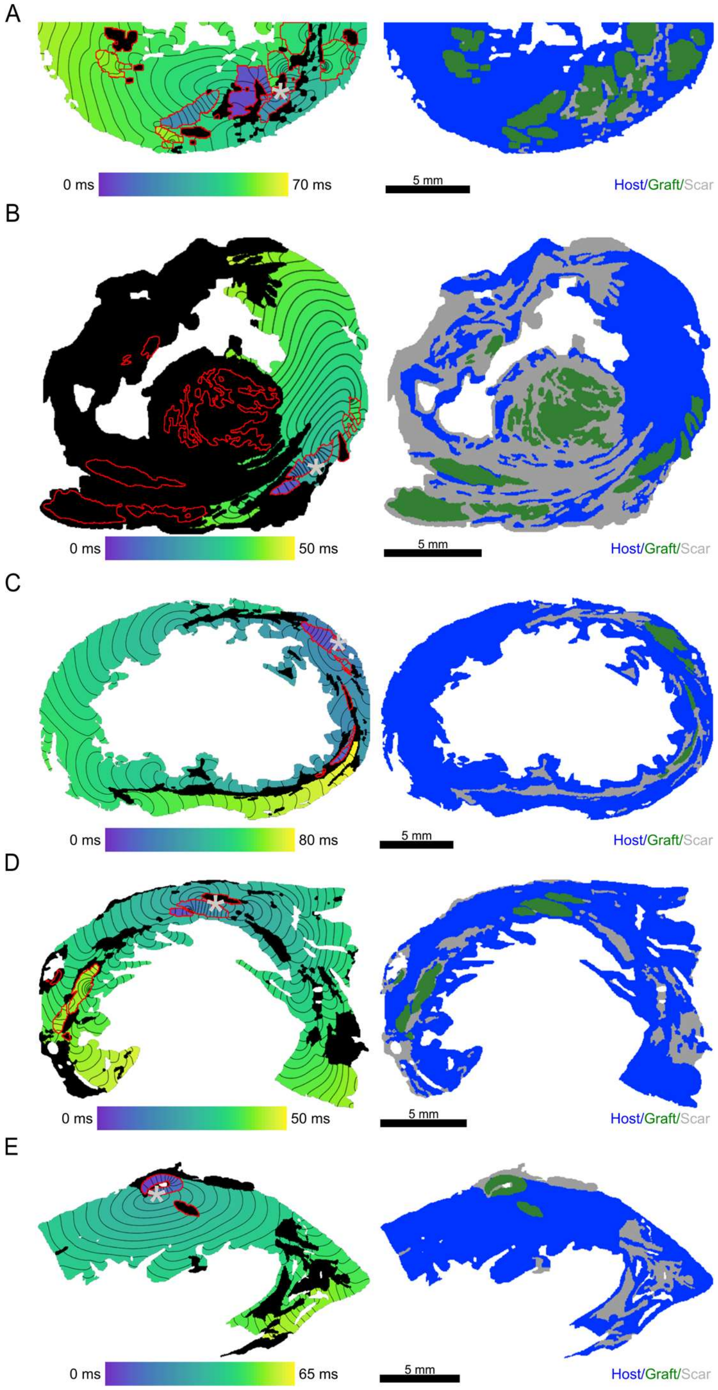

Figure 2.6: In all models at 10% connected at least one permutation had graft-initiated host excitation. *Panels A-E show Model 1 – 5. The left panel shows an example activation map at 10% connected. The grey asterisks denote site of graft-initiated host excitation. The right panel shows the geometry of the mesh labeled with graft (green), host (blue), and non-conductive scar (grey). All scale bars: 5 mm.*

Analysis of all simulations revealed a consistent trend. As p_c increased from very low (i.e., near-complete graft insulation from host) to intermediate values, there was an initial increase in the likelihood ectopic graft-initiated host excitation. Then, with further increase in p_c (i.e., towards full electrical integration of graft), the propensity for these excitations was attenuated and eventually ceased altogether. We observed this inverted paraboloid-shaped relationship in all five models examined (**Fig. 2.7 A**). In four out of five models, the peak incidence of graft-initiated host excitation was at a p_c value of 10-12.5%. At these coupling levels, the proportion of stochastically generated coupling permutations that led to ectopic excitation ranged from ~40% to 100% (in the case of Model 1). The WOV to graft-initiated host excitation ranged from 0-25% in most of these cases. An exception was Model 2, in which ectopic excitations were observed at higher coupling rates up to ~40%. In Model 5, very few permutations resulted in graft-initiated host excitation and peak incidence was at p_c = 5%. Overall, the relationship to graft-host electric coupling was highly dependent on model geometry.

2.4.2 Effects of Scar

It remains unclear how the presence of non-conductive scar affects EA propensity. Does it create restricted channels with arrhythmogenic potential, does it isolate spontaneous excitations by preventing them from reaching host myocardium, or some complex combination of the two? For this reason, we sought to examine the effects of scar on EA propensity. We first replaced scar with healthy myocardium and repeated our experiments as described above. For each model, we still observed an inverted paraboloid shape in the EA relationship; however, the incidence of EA decreased and WOV was shortened to 0-20% in most cases **(Fig. 2.7 B**). To further illustrate this point, Model 2 was an interesting case to consider because several large grafts were isolated by scar. For simulations in this model across all tested p_c values, we observed 288 activations sites (**Fig. 2.7 C**); most of these sites were located around a single medium-sized graft (lower-right corner of image). When identical simulations were re-run with infarcted tissue replaced by host myocardium, the total number of graft-initiated host excitations decreased to 195 (**Fig. 2.7 D**). The only exception to this trend was Model 5, in which replacement of scar with host myocardium increased the number of graft-host excitation. This occurred because removing non-conductive scar left narrow clefts of host myocardium in close proximity to graft, creating conditions that favored initiation of excitation (see right-most panels of **Fig. 2.7 B, D**).

To further understand the range of possible infarct-graft interactions, we conducted additional simulations in which scar was modeled as slow-conducting passive tissue instead of non-conductive insulator. Under these conditions, scar behaved as a pure electrical sink absorbing spontaneously-generated current from graft that could have otherwise initiated excitation elsewhere in host myocardium. This reduced the number of graft-initiated host excitation in all five models, to levels that were even lower than in simulations where scar was removed altogether (**Fig. 2.7 E-F**).

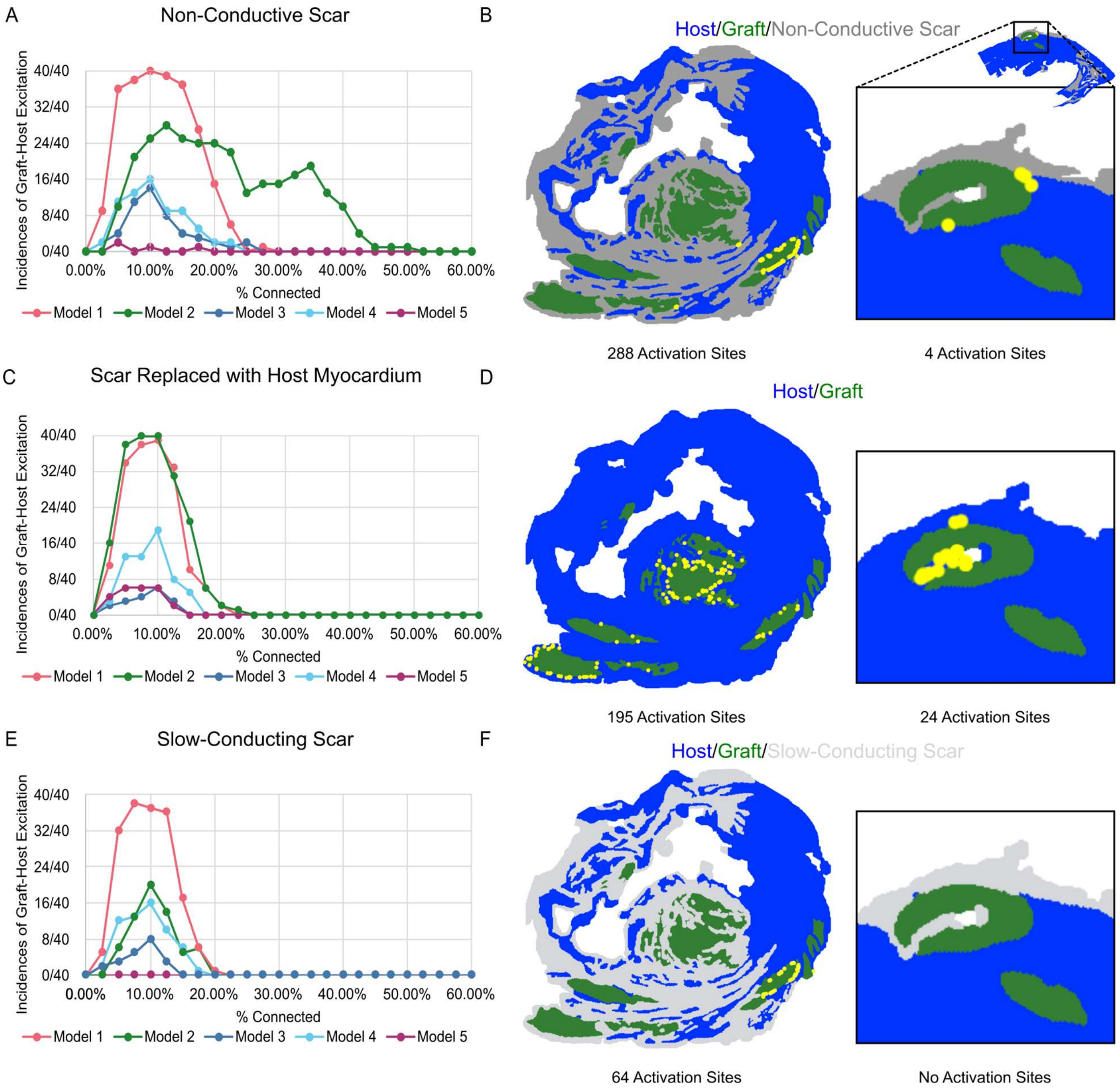

Figure 2.7: Engraftment Arrhythmia is Dynamically Determined by Graft-Host Connectedness. *A-C) Incidence of graft-initiated host excitation across all p_c levels for all five models A) with non-conductive scar, B) scar replaced by host myocardium, and C) slow-conducting scar. D) Model 2 at 1× σ with non-conductive scar had 288 activation sites localized to a few grafts and Model 5 had 4 activation sites. E) When scar was replaced with host myocardium at 1× σ, Model 2 had only 195 activation sites in more widespread locations whereas*

Model 5 had an increase to 24 activation sites. F) When non-conductive scar was replaced by slow-conducting scar, Model 2 had only 64 activation sites and Model 5 had none.

2.4.3 Modulation of intrinsic cell-cell coupling within the graft and EA propensity

Next, we explored how changes in $\sigma_{hPSC\text{-}CM}$ affected EA propensity with non-conductive scar, scar replaced by host myocardium, and slow-conducting scar. For all cases with modified $\sigma_{hPSC\text{-}CM}$, EA propensity vs. p_c relationships retained the characteristic inverted paraboloid shape**.** **Figure 2.8 A** shows the effect of modifications in two representative examples with non-conductive scar. In Model 2, we observed an increase in graft-initiated host excitation at low conductivities, with a dramatic increase in at ¼ × $\sigma_{hPSC\text{-}CM}$ compared to ½ × $\sigma_{hPSC\text{-}CM}$. In Model 3, we also observed an increase in graft-initiated host excitation but the change between ¼ × $\sigma_{hPSC\text{-}CM}$ and ½ × $\sigma_{hPSC\text{-}CM}$ was not as pronounced. In the same representative examples with scar replaced by host myocardium, we observed similar trends. In Model 2, we observed an increase in graft-initiated host excitation at low conductivities relative to 1× $\sigma_{hPSC\text{-}CM}$, but the WOV was shortened from 2.5% - 55% to 2.5% - 30%. In Model 3, we still saw an increase in the incidence of graft-initiated host excitation as we decreased conductivity; however, the overall incidence was flattened when compared to non-conductive scar **(Fig. 2.8 B).** We also observed that as we increase $\sigma_{hPSC\text{-}CM}$, we saw a reduction in the overall prevalence of EA as quantified by AUC and WOV across all models tested for graft conductivities (**Fig. 2.8 D-E**). Finally, when scar was modeled as slow conducting instead of non-conductive, we saw a similar trend towards reduction in EA prevalence. In both representative models shown, we observed a decrease in graft-initiated host excitation compared to non-conductive scar at all $\sigma_{hPSC\text{-}CM}$ values **(Fig. 2.8 C**). The AUC and WOV values across all models were also reduced and abbreviated (**Fig. 2.8 F**). Overall, these findings support the idea that low intrinsic cell-cell coupling in graft strongly favors the incidence of EA.

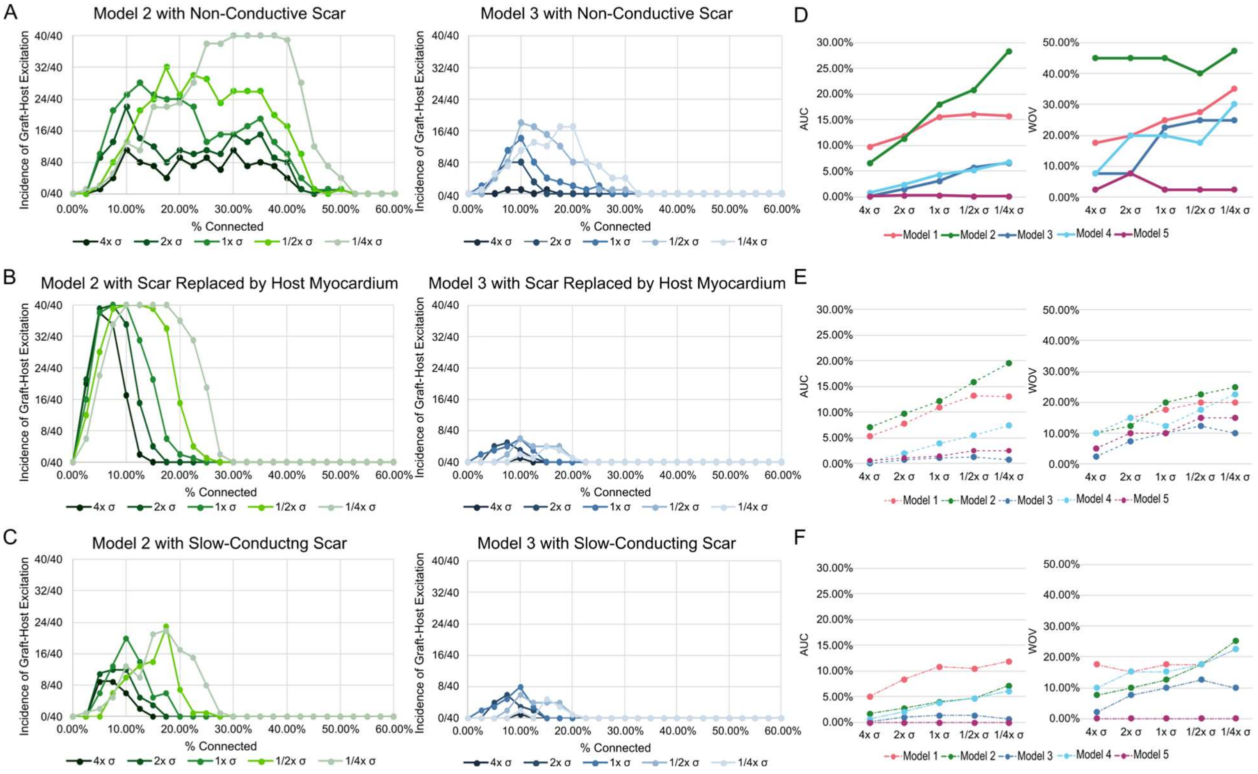

Figure 2.8: Increase in conductivity within the graft and the absence of scar decreases the instances of graft-initiated host excitation in most models. *A-C) Incidence of graft-initiated host excitation with scar at p_c = 0% to 60% for all conductivities tested for Model 2 (green) and Model 3 (blue) A) with non-conductive scar, B) with scar replaced by host myocardium, and C) slow-conducting scar. D-F) The AUC and WOV for all models D) with non-conductive scar, E) with scar replaced by host myocardium, and F) slow-conducting scar are shown.*

2.5 Discussion

In this study, we present a novel computational approach to assess spatiotemporally heterogeneous electrical coupling between graft and host cells in anatomically realistic 2D slice models of remuscularized post-MI macaque ventricles. Our simulations were designed to show how spontaneous excitations of engrafted hPSC-CM could serve as a source that elicits propagating responses in host myocardium. In all five of our models, we showed: (1) varied graft-host coupling creates a milieu conducive to graft-initiated host excitation, (2) in most cases the replacement of scar with host myocardium reduces but does not abolish EA, and (3) increasing intrinsic graft conductivity decreases EA propensity. To our knowledge, this is the first study to computationally investigate focal sources of EA at the tissue scale when the true location and shape of grafts are known.

In our study, we first showed that varying the percentage of graft connected to surrounding tissue could result in graft-initiated host excitation (**Figs. 2.5-7**). For each model, the relationship between EA propensity and the extent of graft-host coupling had an inverted paraboloid shape ranging from p_c = 2.5% to 50%, but the exact dimensions of that shape varied from model to model. Inter-model variability in these characteristics could arise from numerous factors, including differences in MI location and size, the number of cells engrafted in the heart of each animal, details of cardiac anatomy, and locations of the slices with respect to injection sites. This phenomenon observed in simulations is reminiscent of a distinct observation from *in vivo* studies: namely, the variability in timing of the wax and wane of EA from animal to animal [49,51,54]. While we do not know the exact evolution of coupling or whether this phenomenon progresses linearly over time, our results provide a promising starting point to further explore how focal EA mechanisms might depend on graft-host electrical coupling in a broad sense. *In vivo* hPSC-CM transplantation led to a progressive increase of adherens and gap junction proteins, which suggests that electromechanical coupling might be spatiotemporally regulated [56]. This is also consistent with our findings, which show that increasing graft conductivity decreases graft-initiated host excitation (and vice versa, see **Fig. 2.8**).

Finally, we gained more insights into the relationship between scar and graft excitation in the context of EA. In particular, when scar was replaced with host myocardium, graft-initiated host excitation still occurred but was reduced in all but one model. When non-conductive scar was replaced by slow-conducting scar, graft-initiated host excitation was reduced in all models since it created a pure electrotonic sink, effectively increasing the amount of spontaneously generated current that was “squandered” instead of depolarizing host cells (**Figs. 2.7- 8**). Overall, these data suggest that non-conductive scar has a pronounced effect on EA propensity due to changes it creates in source-sink equilibrium. Interestingly, Model 5 showed an increase in EA when scar was replaced by host myocardium. In our simulations of Model 5 with non-conductive scar, there were very few locations at which graft-initiated host excitation could escape: this is because the largest graft region was mostly encased in scar. In Model 5 when non-conductive scar was replaced by slow-conducting scar no graft host-excitations were observed. Upon the replacement of scar with host myocardium, that graft had more locations where excitation of coupled host myocardium could occur. Moreover, proximity to the non-conductive boundary of the model (i.e., the edge of the heart itself) created a favorable source-sink relationship in the thin strip of host myocardium (akin to a Purkinje fiber or an electrically insulated tissue region within a protected isthmus). Although further investigation into the location and consequences of scar relative to graft is needed, these data showed that in some situations the presence of scar could be protective in the context of EA. Finally, on the subject of whether scar *should* ideally be modeled as non-conductive insulator, weakly-conductive passive electrical sink, or some combination of the two, we note that recent studies have shown that nonmyocytes can electrically conduct and couple with myocytes [120–122], it remains unclear if this connection between hPSC-CM and nonmyocytes occurs after transplantation and contributes to EA. In the absence of definitive evidence, we feel that inclusion of both model variants is a prudent approach.

Previous computational work in this area devised a multiscale framework to simulate stem-cell based repair technology in patient-specific models of human hearts post-MI [75]. This study was designed to investigate both focal and reentrant mechanisms. Consistent with our findings, it found that graft-initiated host excitation was constrained by the source-sink mismatch, with the likelihood of ectopic propagation highly dependent on proximity to scar and the theoretical spatial pattern of engrafted cells (in this case represented using a stochastic approximation). Another study created a new biophysically detailed computational model to further assess focal EA mechanisms [77]. Like our work, that study examined the consequences of different graft conductivities and found that ectopic beat propagation was reduced by increased coupling or interface area between graft and host. However, the observed ectopic beats never exceed the intrinsic automaticity rate of ~96 bpm. This might be due to the use of a guinea pig ventricular myocyte model to simulate the graft [123], with automaticity induced by the addition of a constant depolarizing current. Due to this slow graft-induced focal beating rate, the authors again concluded that a reentrant driver mechanism is more likely to contribute to fast EA. Additional studies have tried to look at EA in the context of remuscularization via an hPSC-CM patch [76,78]; however, multiple experimental studies have demonstrated that no electrical coupling occurs in cardiac patches, due to scar-induced insulation of the graft-host border [46,124]. We believe that this is the key to understanding why prior work undervalued the potential importance of focal EA drivers.

Our study has some notable limitations. When modeling variable graft coupling, we chose to stochastically generate different versions of our models, each having a fixed proportion of random graft edges connected to the surrounding tissue. Contemporary understanding from hPSC-CM suggests that connexin-43 co-localizes at the cell membrane in clusters [125] and is circumferentially distributed up to three months following engraftment [49]. Our stochastic approach is plausible and recapitulates this distribution, but it is possible that functional gap junctions would form only along boundaries confluent with fibers, not along laminar boundaries due to shear forces during myocardial contraction.

We also chose to exclude electrophysiological (EP) changes that graft myocytes undergo during maturation (e.g., cells become electrically quiescent due to increased I_{K1} expression and down-regulation of I_f and I_{CaT}). The rationale for this decision was to deliberately explore models in which variables like p_C were the *only* differences, ruling out other potential confounding factors like changes due to intrinsic cell-scale maturity. Moreover, the exact changes in EP properties of engrafted cells over time are not yet fully characterized *in vitro*, so it would be hard to properly calibrate models attempting to probe their importance to EA at this time.

We used 2D slice models derived from histology images, which allowed us to include exact locations of scar, graft, and host myocardium. Creation of 3D models from histology images was not an option in this study due to the inter-slice spacing of 3 mm, which would have led to a staircase effect in the Z direction due to much coarser resolution compared to the X-Y plane. While it might be possible to create 3D models using other imaging techniques, such as magnetic resonance imaging (MRI), graft locations would need to be synthetically generated since contrast agents have not yet been developed to differentiate graft from healthy myocardium in border zone tissue [49]. A related limitation is that in our models we do not modify the underlying ionic currents in host myocardium directly adjacent to scar, as in many prior computational studies [98,116]. However, our models do have a high-resolution representation of the patchy intermingling of myocardium and infarct in these areas, with a resolution greater than what could be observed using MRI.

Finally, since the framework described in this study explored a carefully chosen but narrow question about how spatial properties of graft/host interface may contribute to EA propensity, some important factors remain unexplored. For instance, additional investigations will be needed to clarify the relationship between EA propensity and the spatial conformation of graft/host/scar areas. Moreover, since we did not apply any external pacing to our model, it is unclear if the types of focal sources observed in our simulations could overdrive sinus rhythm. We also note that the MDP in our cell-scale model is slightly lower than values reported in general experimental data [62], and this might affect the dynamics of impulse propagation. We found that the adjustments made to the cell-scale model were the farthest we could push the resting potential towards a more depolarized level without deranging other action potential properties (e.g., upstroke velocity, action potential duration, beating rate, etc.).

In conclusion, our study presented a new way to model hPSC-CM injection with an emphasis on focal mechanisms. We found that varied graft coupling allowed for the wax and wane of EA to be captured in our simulations. This work also allowed us to elucidate the role of scar tissue in the onset of EA and how this can change due to source-sink mismatch. While we may not yet have elucidated the true mechanism of EA, these data can be used in the future to pinpoint areas that are less arrhythmogenic for targeted delivery of hPSC-CM therapy.

Chapter 3: Population-Based Computational Simulations Elucidate Mechanisms of Focal Arrhythmia Following Stem Cell Injection

3.1 Abstract

Following a myocardial infarction (MI), a large portion of ventricular cells is replaced by scar, leading to adverse structural remodeling and heart failure. The use of stem cell-derived cardiomyocytes has shown promise in restoring cardiac function in animal models following an MI but leads to rapid focal ventricular tachycardia (VT). The VT in these animals can be variable, and its underlying mechanisms remain unknown. In this study, we used three distinct computational models derived from histological images of post-MI non-human primate ventricles to understand how human pluripotent stem cell-derived cardiomyocytes (hPSC-CMs) grafts can affect focal VT individually and synergistically. Specifically, we explored whether grafts could work cooperatively to create new arrhythmia and if geometric features such as graft tortuosity, area, host isolation, and amount of surrounding scar inhibited or enhanced the effect. We observed at least one instance of graft-host excitation (GHE) for eleven of the twenty-five individual grafts examined. Since we used a stochastic population-of-models-based approach to generate graft boundaries, we found that the number of permutations with GHE varied from graft to graft. We also examined grafts in aggregate and found that the high prevalence of GHE when all grafts were included arose from combinations of individually arrhythmogenic grafts (i.e., the overall increase in arrhythmogenicity resulted from graft *complementarity* rather than graft *cooperativity*). Further analysis of graft spatial features showed that arrhythmogenic grafts tend to be in areas with high host isolation (i.e., spatially confined regions of surviving myocardium interdigitated with engrafted cells) and when graft area and tortuosity were also high. These insights can aid in the design of novel injection schemes that could result in safer therapy for patients.

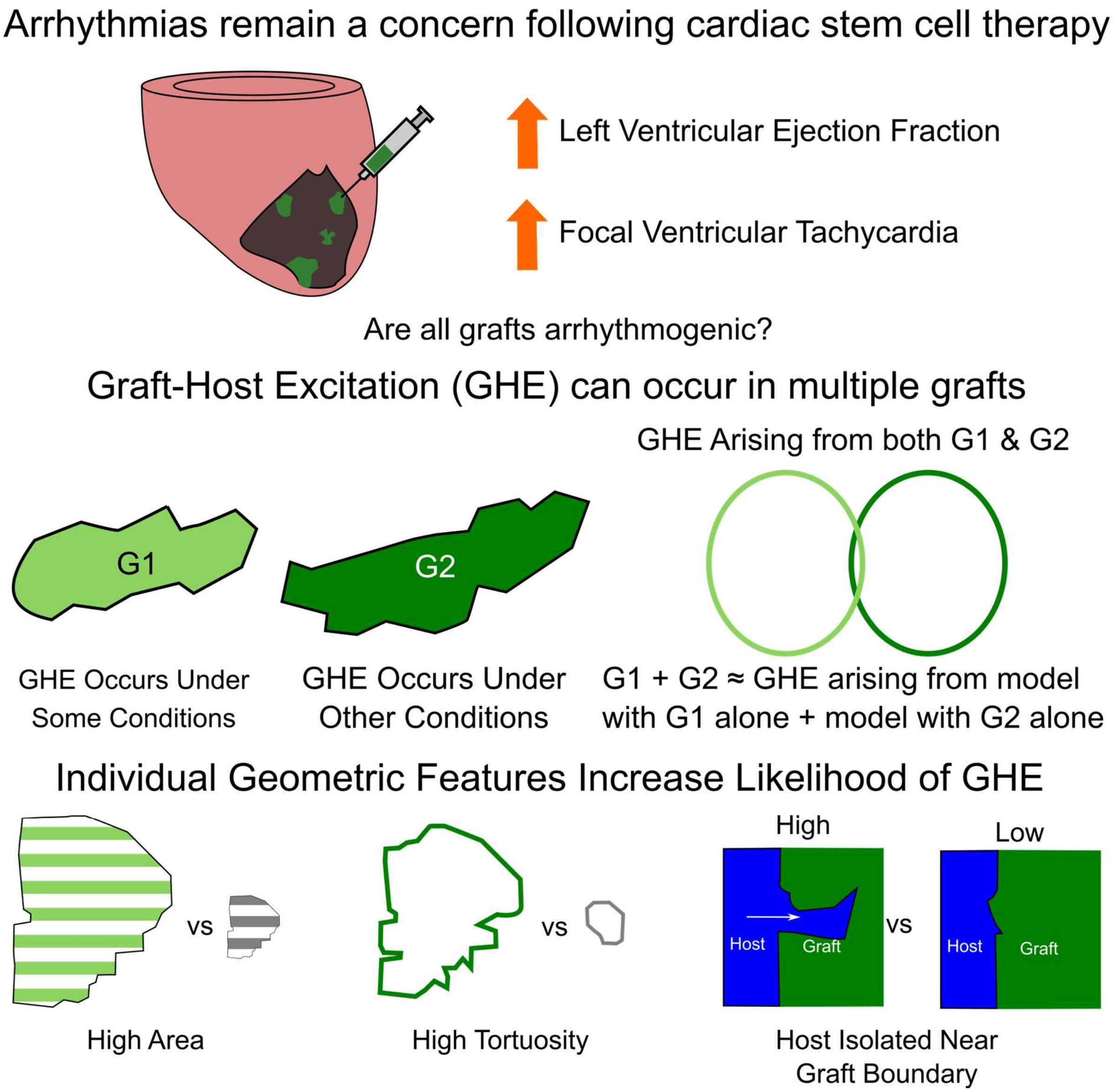

Graphical Abstract 3.0: *Focal arrhythmias following stem cell injection may partly be attributable to graft interactions. Multiple grafts can potentially elicit graft-host excitation (GHE) under different conditions. Individual graft features such as high area, high tortuosity, and host myocardium isolation near the graft boundary increase the likelihood of GHE. When multiple grafts are present, the combined arrhythmogenicity is mostly due to inter-graft redundancy rather than cooperativity between grafts via electric coupling to the host.*

3.2 Introduction

In the United States, it is estimated that 805,000 people experience a myocardial infarction (MI) annually [126]. Following a large MI, over a quarter of the left ventricle is damaged via cell death and necrosis [127,128]. Due to the heart's lack of regenerative ability [5], many patients will develop heart failure due to adverse structural remodeling [129]. Treatment options for these patients focus on symptom management through medications such as angiotensin-converting enzyme inhibitors or beta-blockers [130]. While these medications can help, many patients continue to worsen and progress to advanced or end-stage heart failure [14]. This has created a critical need for innovative cardiac regenerative therapies that effectively replace damaged myocardium.

Human pluripotent stem cell-derived cardiomyocyte (hPSC-CM) transplantation has been shown to remuscularize damaged myocardium following cardiac injury in animal models [89,55,56,49,54,51,90,131]. However, transient ventricular tachycardia (VT) occurred shortly following transplantation in non-human primate and porcine models [49,54,51,90,131,50]. The rate of VT is variable, but cardiac anatomical mapping has shown clinical-grade evidence that these are focal arrhythmias originating at sites of cell implantation [49,51,54]. At present, we do not fully understand the mechanisms leading to variable VT in these animal models, which can impede safe translation to human studies.

Understanding VT mechanisms following transplantation is limited, partly due to a lack of tools to precisely examine electrical interactions between hPSC-CMs and host myocardium. Computational models of cardiac electrophysiology are helpful multiscale tools that can help fill this gap [75–77,79]. They can be used to systematically examine how cell-scale differences, such as varied ion channel kinetics and expression, can affect emergent electrical properties at the tissue and organ scales [67,132,133]. They can also be used to create realistic virtual representations of cardiac geometry [97,116,134–137].

Previous work from our lab showed that focal VT phenomena could be partially explained by spatially heterogeneous development of graft-host electrical coupling over time [79]; however, contributions of individual grafts, including their specific capacity for arrhythmogenicity, remain poorly characterized. This study aims to analyze how arrhythmogenicity is impacted by individual hPSC-CM grafts and groups thereof, including a characterization of relevant geometric features. Using our previously developed computational framework [79], we investigate the hypothetical arrhythmic consequence of specific grafts synthetically removed (i.e., “vanished”) from our geometries to determine whether individual regions of hPSC-CM had cooperative or complementary effects on VT prevalence. We also analyze spatial characteristics of individual grafts and the mixture of scar and surviving myocardium in their vicinity to formulate guidelines for safer injection.

3.3 Methods

3.3.1 Cell and Tissue-Scale Electrophysiological Modeling

Simulations were conducted in three computational slice models from our previous study of post-MI macaque ventricles containing host myocardium, hPSC-CM grafts, and infarcted tissue (scar) [79]. We modeled membrane kinetics of host ventricular myocardium using the ten Tusscher et al. human ventricular ionic model [109]. hPSC-CM membrane kinetics were modeled using our previous study's modified hPSC-CM cellular model [79]. Briefly, we simulated total knockout of inward rectifier potassium current (I_{K1}) and doubled the conductance of the pacemaker current (i.e., the “funny” current; I_f) [69]. As in our previous study and others, scar was modeled as a non-conductive insulator [79,116]. Before all simulations, we let the cell-scale hPSC-CM model run to steady-state conditions, allowing it to beat spontaneously for 130 cycles. Steady state was visually confirmed to ensure no large variations in action potential morphology were observed. The membrane voltage state was saved at the minimum diastolic potential (MDP, i.e., the most negative membrane voltage of the action potential) following the final spontaneous beat.

As in previous studies [79,116,98,114], the monodomain finite-element approximation model was used to govern tissue-scale electrical activity propagation [110,111]. Electrical current flow in the myocardium was represented by solving the associated partial differential equations. Membrane kinetics were described by solving the algebraic and ordinary differential equations related to the models of cellular electrophysiology in ventricular (host) and graft regions, as described earlier in this section. Bioelectrical simulations were conducted using openCARP [118], and the resulting data were visualized using Dr. Edward J. Vigmond's meshalyzer tool; both are freely available for non-commercial use (see http://opencarp.org/). Version 7.0 of openCARP was used for these simulations. Similar to prior work [79,98], conductivity tensor values for host myocardium in the longitudinal and transverse directions with respect to fiber orientation were set to σ_L = 0.255 S/m and σ_T = 0.0775 S/m, respectively. Areas of engrafted hPSC-CMs (grafts) were modeled with an isotropic conductivity tensor of $\sigma_{hPSC\text{-}CM}$ = 0.0775 S/m. All simulations were run for 1000 ms to assess graft-host excitation (GHE) propensity. We defined GHE as spontaneous depolarization of a graft leading to electrical excitation in over 50% of the host myocardium; this was used as a surrogate measurement to approximate VT susceptibility. This work was facilitated using advanced computational, storage, and networking infrastructure provided by the Hyak supercomputer system at the University of Washington.

3.2.2 *Synthetically Altering the Presence or Absence of Individual Grafts*

To assess individual and synergistic effects of grafts on arrhythmogenicity, we labeled and synthetically removed grafts of interest from our slice geometry **(Fig. 3. 1A, Suppl. Fig. 3.1)**. Removal of a graft meant treating it as host myocardium instead of hPSC-CM. As in our previous study[79], we chose to model hPSC-CM graft-to-host intercellular electrical connectedness at 10% **(Fig. 3.1 B)**. A connectedness of 10% was selected because peak GHE was observed in all three geometries at this value in our original study. Briefly, we used a discontinuous finite element method to disconnect 90% of elements along the graft boundary. We used a stochastic approach to generate a population of 40 unique spatial configurations per graft island combination **(Fig. 3.1 C).** We enforced consistent use of random number generator seeds to ensure that every N^{th} individual permutation of a given graft had the same electrical connectivity boundary, regardless of which other grafts were present. An example is shown in **Figs. 3.1 C-E**. The four columns shown, each associated with a different N value, illustrate that the two grafts in the example (#1 and #2) have unique connectivity profiles **(Figs. 3.1 C-D)** that are preserved within each column for configurations in which both grafts are present **(Fig. 3.1 E).** To evaluate possible graft synergistic effects, we defined graft cooperativity as GHE occurring in at least one new spatial configuration with the addition of another graft.

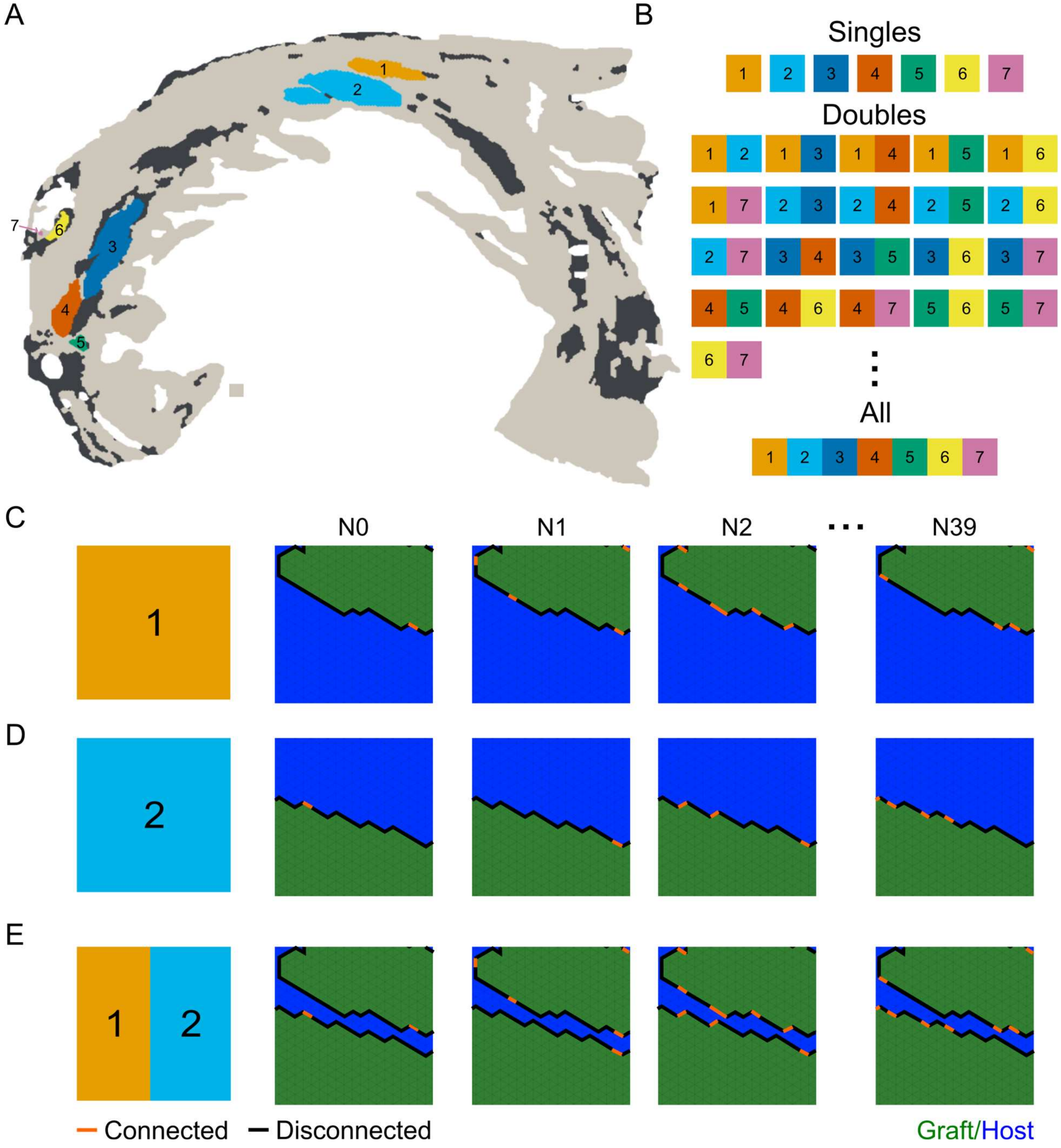

Figure 3.1: Methods *A) Each individual graft was assigned a distinct region identifier. B) Different potential combinations of two or more grafts were tested. C-E) Examples of individual graft connectivity permutations (10% conductive boundary) for C) graft 1 and D) graft 2. E) Graft boundaries were kept consistent when grafts were combined for each connectivity permutation.*

3.3.2 Identifying site and time of earliest activation

As in our previous study [79], we identified the earliest activation sites that led to successful propagating wavefronts in host myocardium. We first identified the time at which activation in the host distal to the graft occurred. We then worked backward to determine the origin site to avoid identifying false positive breakthrough sites where graft spontaneous activity leads to non-sustained depolarization in host tissue.

3.3.3 Spatial Properties Analysis

To probe the relationship between graft spatial properties and GHE propensity, we defined five features of interest: graft area, percentage of scar within 1mm of graft boundary, distance between closest edges of two grafts, graft boundary tortuosity, and host isolatedness. Our rationale for examining scar within 1 mm of graft boundaries was that tissue farther away would be unlikely to affect electrophysiology proximal to the graft due to the cardiac space constant [138,139]. We defined tortuosity as:

$$Tortuosity = \frac{Total\ Graft\ Perimeter}{\sqrt{Total\ Graft\ Area}}$$

Host isolatedness was derived by examining the circular region within 200 μm of each ventricular point in the model and calculating the proportion of that area that was occupied by anything other than host tissue (i.e., the union of graft, scar, and empty space surrounding the model). To analyze the relationship between graft micro-environment and the locations of initial breakthroughs during GHE events, we classified the points along each graft boundary as being either proximal to (≤ 200 μm) or distal from (> 200 μm) from empirically identified sites of the earliest host activation. Receiver operating characteristic (ROC) analysis was used to determine whether graft boundary proximity to breakthroughs could be predicted from the extent of nearby host isolatedness.

3.3.4 Statistics

Individual grafts with and without GHE were divided into two groups. Continuous spatial variables were compared pairwise between groups using Wilcoxon rank-sum tests in Python. Pandas [140], NumPy [141], Matplotlib [142], SciPy [143], and scikit-learn [144] packages were used to create plots to summarize spatial features and for ROC analysis.

3.4 Results

3.4.1 GHE Propensity of Individual Grafts

In our exploration of GHE propensity for individual grafts and combinations of grafts in three ventricular slice geometries, several distinct qualitative trends were identified. Across all models, smaller grafts in isolation tended to be less likely to produce a coupling configuration with GHE. Conversely, larger grafts were more likely to produce multiple coupling configurations with GHE (**Fig. 3.2**). In Geometry 1, nine of fifteen individual grafts could provoke ectopic excitation. The GHE propensities of those grafts ranged from 8/40 to 22/40 (**Fig. 3.2 A**); these proportions indicate the number of unique patterns that resulted in GHE in the population of 40 coupling configurations. In Geometry 2, we observed GHE originating from three of seven grafts, with GHE propensity ranging from 3/40 to 19/40. (**Fig. 3.2 B**). In Geometry 3, we found three of the seven grafts had at least one configuration with GHE, with their propensity ranging from 3/40 to 28/40 (**Fig. 3.2 C**). A comparison of GHE propensity for all single grafts can be found in **Figure 3.2 D** with total GHE when all grafts are present denoted by a star. Quantitatively, we observed that breakthrough sites tended to occur in spatially constrained pockets of surviving myocardium adjacent to graft (**Suppl Fig. 3.2**).

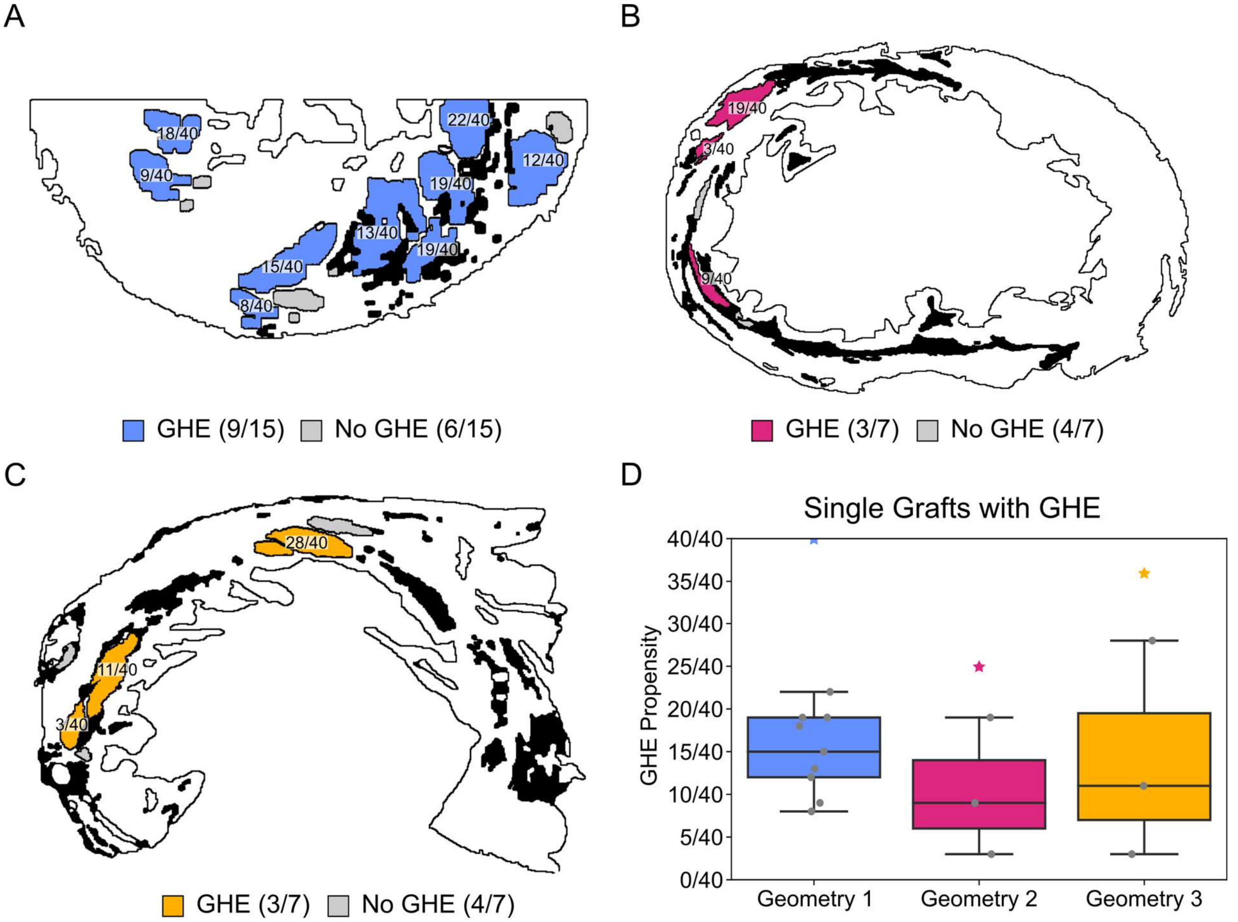

***Figure 3.2: Individual grafts are capable of GHE, but arrhythmogenic propensity varies from graft to graft**. A-C) Individual grafts capable of GHE are shown in A) Geometry 1 (blue), B) Geometry 2 (pink), and C) Geometry 3 (yellow). Grafts incapable of individually provoking graft-host excitation are shown in gray. Scar is shown as black regions. D) Varied GHE propensity of each graft is shown per geometry in a box and whisker plot. Stars show GHE propensity for each histology-based geometry for the simulation configurations where all grafts were present.*

3.4.2 Inter-graft cooperativity plays a minor role in overall GHE.

Next, we explored if possible synergistic interactions between two or more graft configurations that were previously quiescent could result in new GHE, which we classify as graft cooperativity. A representative example of graft cooperativity for Geometry 3 is shown in **Figure**

3.3. Graft 1 alone had no coupling configurations with GHE. Graft 2 alone had 28/40 (70%) configurations with GHE. When both grafts were present, GHE for the aggregate population was 35/40 (87.5%) coupling configurations (**Fig. 3.3 A**). A closer look at this representative example for a specific set of coupling patterns in the population shows that graft 1 was capable of isolated (i.e., non-GHE) spontaneous beating at a slow rate (**Fig. 3.3 B;** dark pink trace) that failed to ignite propagation in the host myocardium. In the proximal myocardium (yellow voltage trace), graft excitations corresponded to a slight elevation of membrane potential that failed to reach the activation threshold; the distal myocardium (light grey trace) was not perturbed. For the isolated version of graft 2 with the same (N^{th}) permutation in the population of coupling configurations (**Fig. 3.3 C**), the spontaneous beating rate in the hPSC-CM region was faster (purple trace), but a similar failure to elicit excitation was seen in the same proximal and distal areas of host myocardium. When grafts 1 and 2 were both included in the geometry with the same identical (N^{th}) electrical coupling configurations (**Fig. 3.3 D**), the combined effects at the proximal host site (yellow) resulted in a depolarized membrane compared to the distal host site (light grey); this altered the electrotonic milieu sufficiently for graft 1 (dark pink) to trigger GHE.

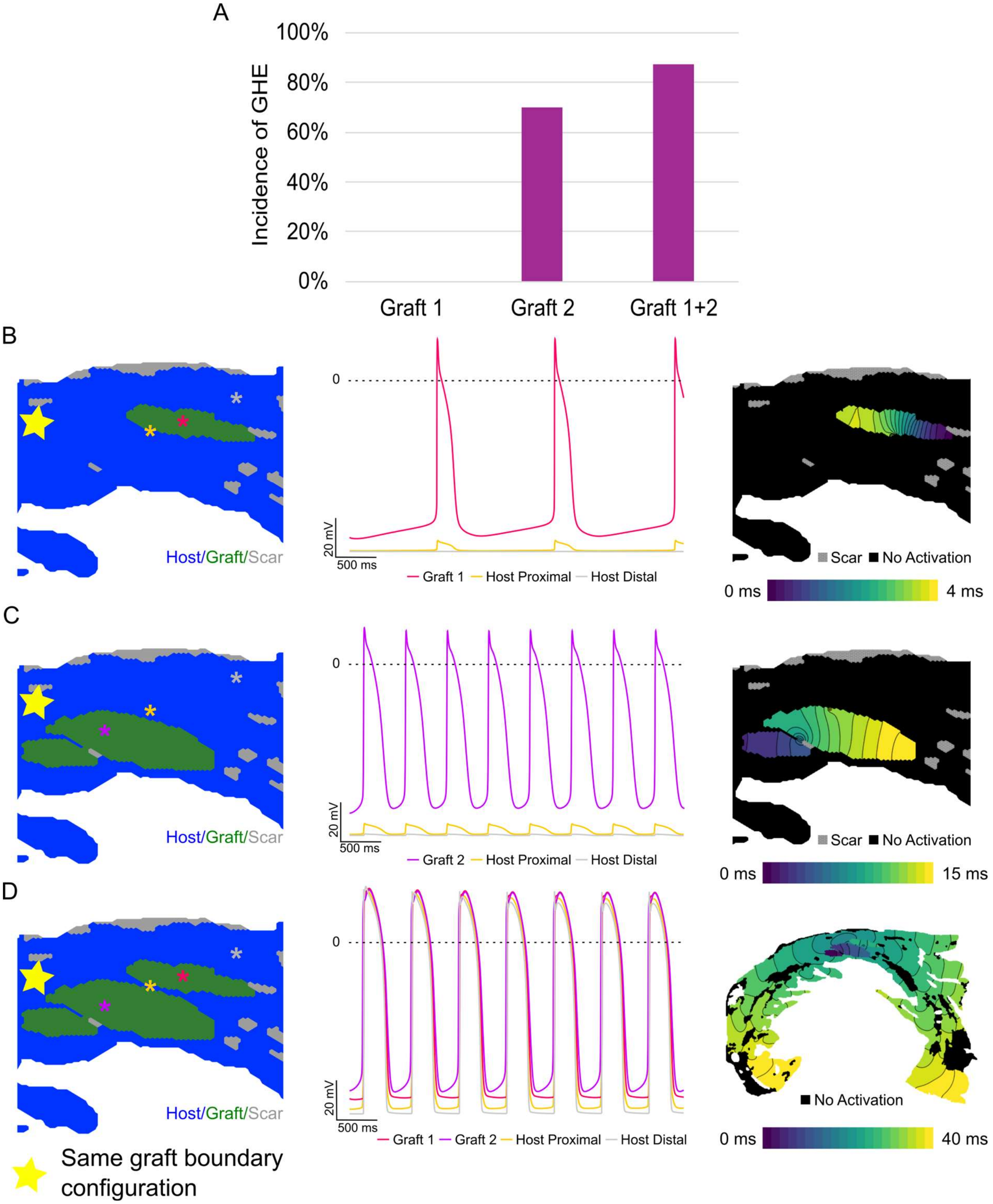

Figure 3.3: Graft cooperativity is possible. *A) For all graft-host boundary configurations, Graft 1 in isolation had no GHE. Graft 2 had some GHE, but the combination of Grafts 1 and 2 led to increased GHE due to synergistic interaction (i.e., cooperativity). B-C) For the boundary*

configuration shown, neither Graft 1 nor Graft 2 had GHE in the individual configuration. D) With identical boundary conditions, when both grafts are present, new GHE occurred. Column 1 shows the labeled geometry with colored asterisks denoting the locations of voltage traces, as shown in column 2. Column 3 shows the activation map.

To better understand graft cooperativity, we mapped the breakthrough sites of new GHEs to their respective locations when two grafts were present (**Fig. 3.4**). All observed graft cooperativity involved at least one graft that was individually capable of eliciting GHE. Two grafts commonly involved in cooperative GHE are shown with pink stars and black asterisks. Most GHEs resulting from cooperativity originated in narrow clefts of host myocardium, frequently in the area between two grafts. There were a few exceptions where new GHE occurred near scar (orange arrows in **Fig. 3.4**) or small divots within the graft (white arrows in **Fig. 3.4**). The prevalence of graft cooperativity was low, with only 56 examples of new GHE observed across all three models.

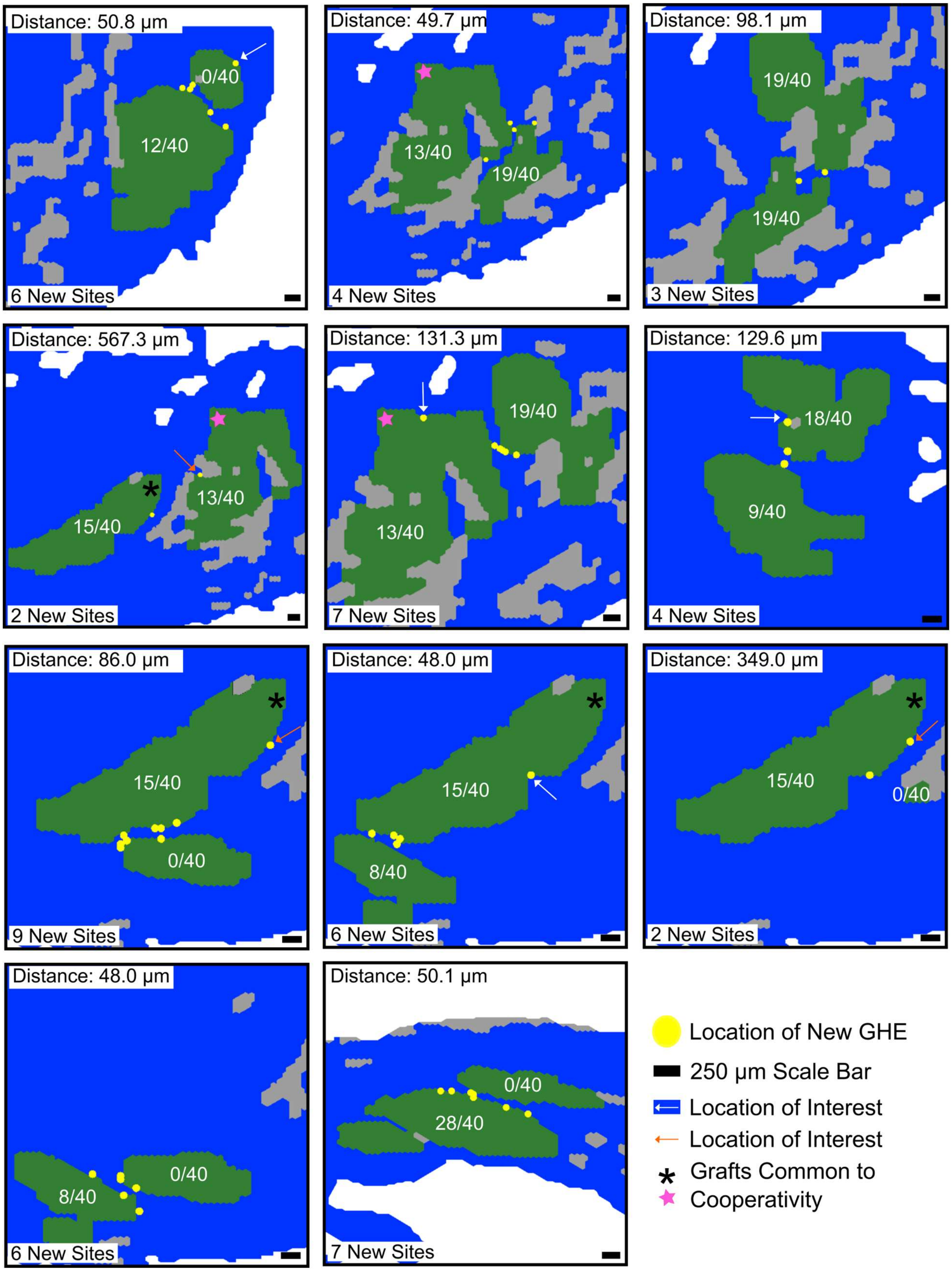
Distance: 50.8 µm
0/40
12/40
6 New Sites
Distance: 49.7 µm
13/40
19/40
4 New Sites
Distance: 98.1 µm
19/40
19/40
3 New Sites
Distance: 567.3 µm
13/40
15/40
2 New Sites
Distance: 131.3 µm
19/40
13/40
7 New Sites
Distance: 129.6 µm
18/40
9/40
4 New Sites
Distance: 86.0 µm
15/40
0/40
9 New Sites
Distance: 48.0 µm
15/40
8/40
6 New Sites
Distance: 349.0 µm
15/40
0/40
2 New Sites
Distance: 48.0 µm
0/40
8/40
6 New Sites
Distance: 50.1 µm
0/40
28/40
7 New Sites
Location of New GHE
250 µm Scale Bar
Location of Interest
Location of Interest
Grafts Common to
Cooperativity

Figure 3.4: Graft cooperativity occurred in multiple graft configurations. *Yellow dots represent locations of new GHEs resulting from graft cooperativity. Grafts that commonly contribute to new GHE are shown with a black asterisk or pink star. Boundary locations of interest are highlighted with white or orange arrows. All grafts are labeled with their individual propensity for GHE. Each panel provides the distance between the nearest points of the two grafts highlighted. Scale bars: 250 µm.*

Since cooperativity contributed modestly to aggregate GHE, we next sought to understand how much of the ectopic activity in multi-graft geometries could be attributed to complementarity. We defined complementarity at the population scale, meaning that for the N^{th} pattern of electric coupling for a particular combination of grafts in one geometry, the presence of GHE was the result of spontaneous excitation originating from one or more hPSC-CM regions that were already arrhythmogenic in a configuration with fewer grafts. In the context of complementarity, bystander grafts that did not affect GHE propensity were also possible. An example is shown in **Figure 3.5**. In Geometry 2, Graft 1 had 19 coupling permutations exhibiting GHE **(Fig. 3.5 A),** while Graft 5 had nine permutations exhibiting GHE **(Fig. 3.5 B)**. When both grafts were combined, new permutations resulted in GHE **(Fig. 3.5 C)**.

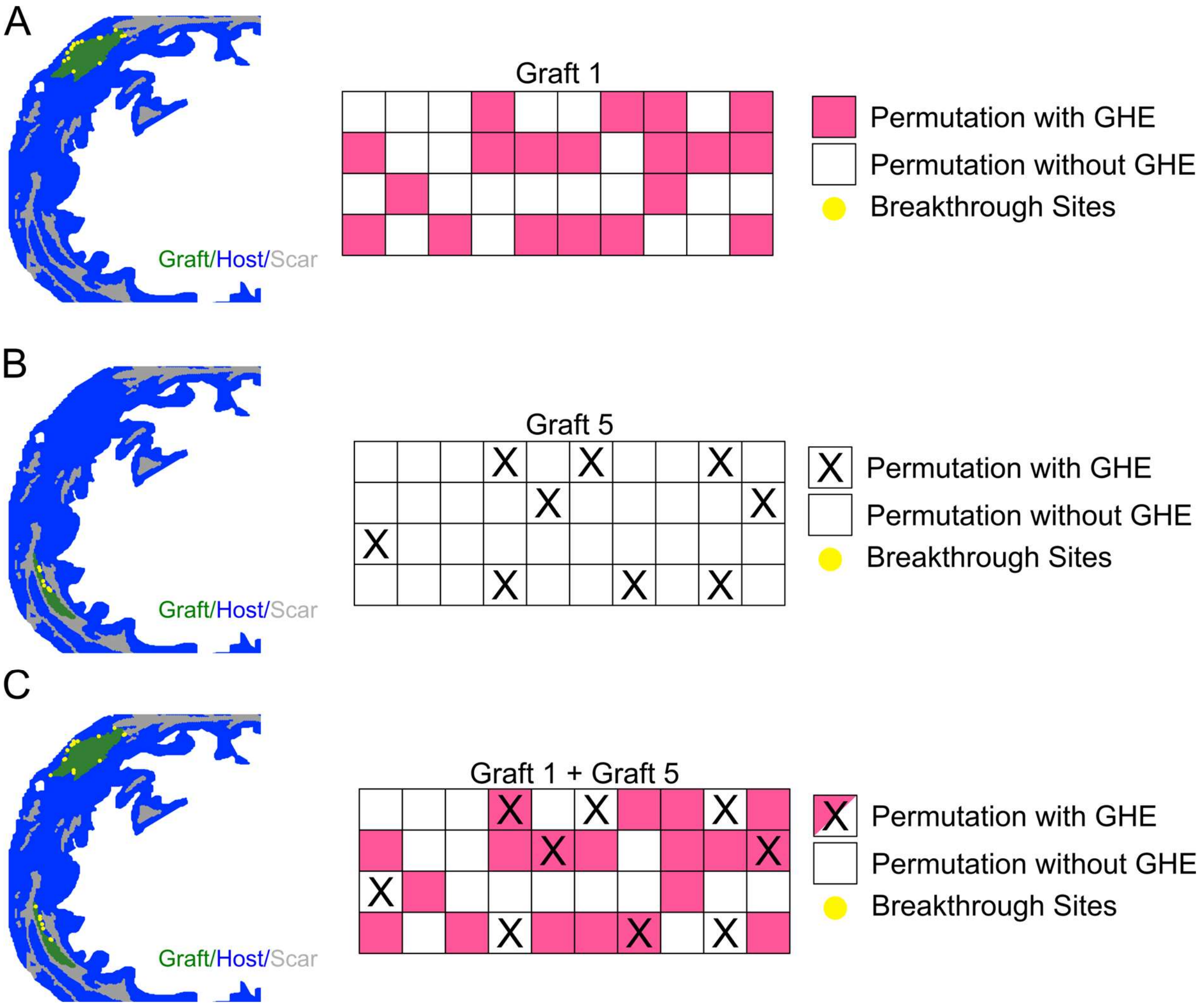

Graft 1

			🟥			🟥	🟥		🟥
🟥			🟥	🟥	🟥		🟥	🟥	🟥
	🟥						🟥		
🟥		🟥		🟥	🟥	🟥			🟥

🟥 Permutation with GHE
☐ Permutation without GHE
● Breakthrough Sites

Graft 5

			X		X			X	
				X					X
X									
			X			X		X	

X Permutation with GHE
☐ Permutation without GHE
● Breakthrough Sites

Graft 1 + Graft 5

			🟥 X		X	🟥	🟥	X	🟥
🟥			🟥	🟥 X	🟥		🟥	🟥	🟥 X
X	🟥						🟥		
🟥		🟥	X	🟥	🟥	🟥 X		X	🟥

🟥 X Permutation with GHE
☐ Permutation without GHE
● Breakthrough Sites

Figure 3.5: Graft complementarity occurs when two or more independently arrhythmogenic grafts have no new coupling configurations resulting in GHE. *A) Geometry 2 Graft 1 had 19/40 permutations, resulting in GHE. B) Geometry 2 Graft 5 had 9/40 permutations resulting in GHE. C) When Graft 1 and Graft 5 were combined, no new coupling configurations resulted in GHE.*

We next compared the individual GHE rates for each graft in each geometry to the incidence of ectopic firing when *all hPSC-CM regions except that specific graft* were present (i.e., "one graft is excluded" simulations). For Geometry 1, this analysis did not yield any notable differences in GHE rate, indicating a high level of cooperative redundancy between the fifteen grafts across the population of coupling configurations (**Fig. 3.6 A**). On the other hand, for Geometry 2 and 3, the effects of adding or removing a particular individual graft effect are better highlighted. When Graft 1 was excluded from Geometry 2, there was a noticeable decrease in GHE excitation (**Fig. 3.6 B**; GHE = 11/40 for the first box in the "Excluded Graft" row, vs. >20/40 for all other boxes, i.e., cases in which Graft 1 was present). Likewise, when Graft 2 was excluded from Geometry 3, the rate of GHE dropped to 10/40 compared to 32/40 when that particular hPSC-CM region was included (**Fig. 3.6 C**).

A clear illustration of the overall contributions of graft complementarity and cooperativity for all combinations of grafts is provided in **Figure 3.6 D-F**. For all geometries, increased GHE incidence was associated with the number of grafts included. For Geometry 1, most new GHE seen in multi-graft configurations was attributed to complementarity (**Fig. 3.6 D blue**), with only a tiny percentage attributed to cooperativity when two to four grafts were present (**Fig. 3.6 D orange**). We also observed a plateau in GHE when more than ten grafts were present. For Geometry 2, there were incidences of graft cooperativity observed across all simulations (**Fig. 3.6 E**). For Geometry 3, graft cooperativity contributed negligibly to overall GHE when two grafts were present (**Fig. 3.6 F**).

A

GHE Rates of Individual Grafts

1	2	…												15
0/40	12/40	22/40	19/40	13/40	19/40	15/40	0/40	0/40	0/40	8/40	0/40	0/40	9/40	18/40

GHE Rates of When One Graft is Excluded

All but 1	All but 2	…												All but 15
40/40	40/40	40/40	40/40	40/40	40/40	39/40	40/40	40/40	40/40	40/40	40/40	40/40	40/40	40/40

B

Individual Grafts

19/40	3/40	0/40	0/40	9/40	0/40	0/40

Excluded Graft

11/40	24/40	25/40	25/40	20/40	25/40	25/40

C

Individual Grafts

0/40	28/40	11/40	3/40	0/40	0/40	0/40

Excluded Graft

32/40	10/40	36/40	37/40	36/40	36/40	36/40

Figure 3.6: In simulations to assess the overall propensity for GHE, complementarity effects are dramatically more important than cooperativity effects. *A-C) GHE rates for simulations in which each individual graft was included vs. those in which all grafts were included, except for that individual graft are shown. A) Geometry 1 (Blue), B) Geometry 2 (pink), and C) Geometry 3 (Yellow) as shown in Figure 2. D-F) Normalized contributions of complementarity (blue, pink, or yellow) vs. cooperativity (orange) as the number of grafts increases for each geometry. Gray denotes no GHE. Black shows GHE when only one graft is present.*

3.4.3 Individual graft spatial features and inter-graft spacing affect GHE.

To better understand why some grafts are arrhythmogenic while others are not, we ran statistical analysis on hPSC-CM region spatial features for all permutations of either one or two grafts (**Fig. 3.7**). For individual grafts, the median graft area of grafts with one or more permutations resulting in GHE was 0.02151 cm^2 compared to 0.00161 cm^2 of those without. Larger graft area was strongly associated with GHE prevalence (**Fig. 3.7 A**; p=0.0000155). To estimate the characteristics of graft boundary waviness, tortuosity was calculated. We found that median tortuosity was also higher in grafts with one or more permutations resulting in GHE (6.244 vs. 4.188). A higher graft tortuosity was associated with GHE propensity (**Fig. 3.7 B;** p=0.00167). However, GHE propensity was not affected by the scar percentage within 1 mm of each graft's peripheral area (**Fig. 3.7 C**; median 13.181% vs 13.195%; p=0.82725). We also examined how inter-graft distance may play a role in GHE arising from cooperativity. We observed that new GHE occurred when inter-graft separation was ≤ 875 μm (**Fig. 3.7 D**).

Finally, we used a host isolatedness metric (see definition in Methods) to develop a more robust understanding of the relationship between graft micro-environment and GHE propensity. An example of the analysis for an illustrative individual graft in Geometry 1 is shown in **Figure 3.7 E-F**. Since the known breakthrough sites of GHE could be identified **(Fig. 3.7 E-F)**, host boundary proximal to known breakthrough sites was treated as ground truth positive (i.e., an ideal predictive metric would flag those locations as highly likely to be at or near the initiation of GHE). Then, analyzing only the host myocardium, we identified areas of high host isolatedness throughout the tissue, including along the graft-host boundary (**Fig. 3.7 G**; dark red areas indicate high levels of the metric). Indeed, for the same example shown in **Fig. 3.7 E-G**, host isolatedness values from points along the boundary proximal to breakthrough sites were significantly higher than those at distal boundary points **(Fig. 3.7 H)**. ROC analysis of this relationship across all cases of GHE from individual grafts in all three geometries revealed a robust predictive relationship (area under the ROC curve = 0.85; **Fig. 3.7 I**).

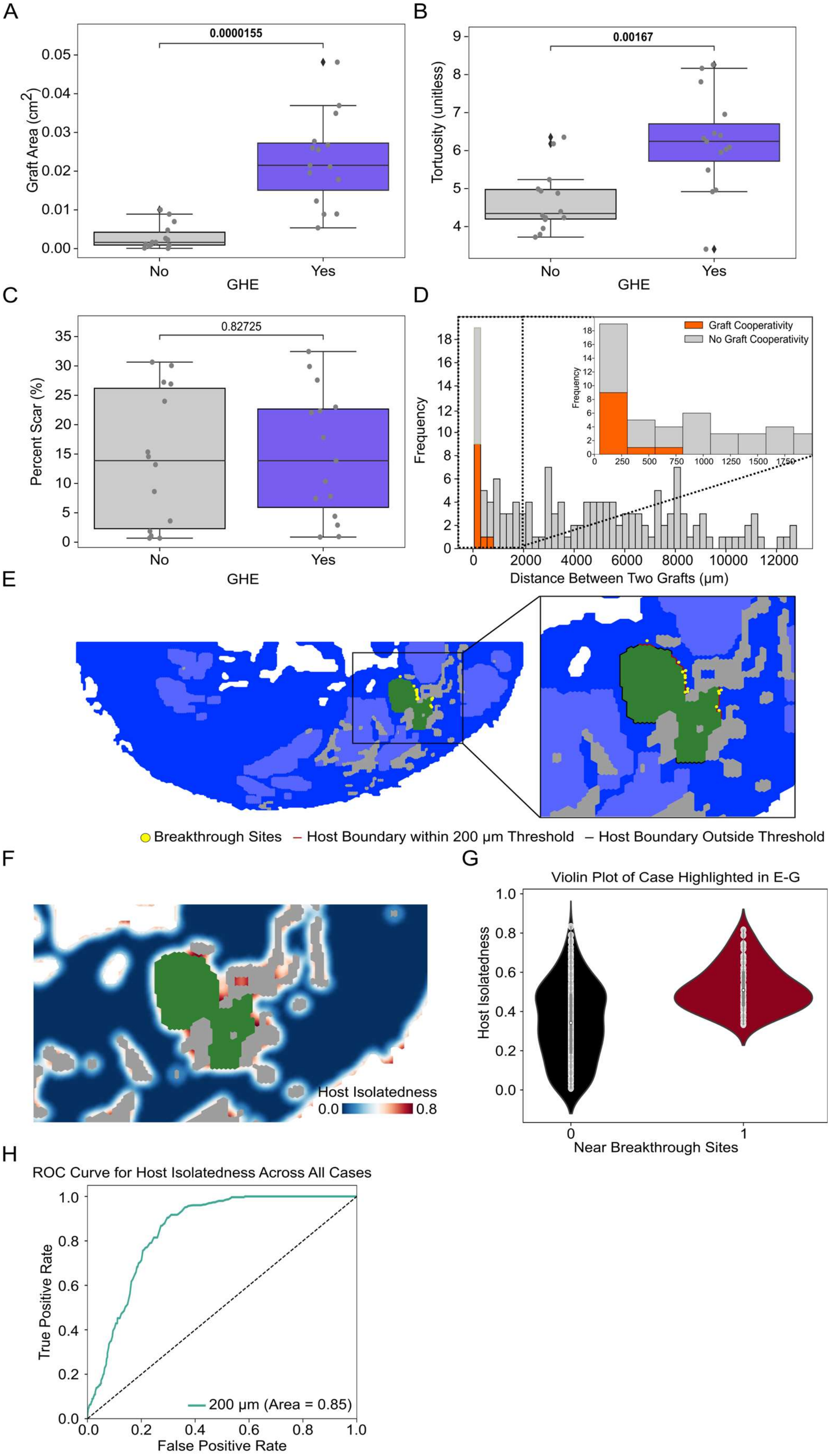
A
0.0000155
Graft Area (cm^2)
0.00
0.01
0.02
0.03
0.04
0.05
No
Yes
GHE
B
0.00167
Tortuosity (unitless)
4
5
6
7
8
9
No
Yes
GHE
C
0.82725
Percent Scar (%)
0
5
10
15
20
25
30
35
No
Yes
GHE
D
Graft Cooperativity
No Graft Cooperativity
Frequency
0
2
4
6
8
10
12
14
16
18
0
2000
4000
6000
8000
10000
12000
Distance Between Two Grafts (μm)
0
250
500
750
1000
1250
1500
1750
E
Breakthrough Sites
Host Boundary within 200 μm Threshold
Host Boundary Outside Threshold
F
Host Isolatedness
0.0
0.8
G
Violin Plot of Case Highlighted in E-G
Host Isolatedness
0.0
0.2
0.4
0.6
0.8
1.0
0
1
Near Breakthrough Sites
H
ROC Curve for Host Isolatedness Across All Cases
True Positive Rate
False Positive Rate
0.0
0.2
0.4
0.6
0.8
1.0
200 μm (Area = 0.85)

Figure 3.7: Statistical Analysis of Graft Spatial Features: *A) Graft area (cm*^{2}*) of single grafts with permutations resulting in GHE (purple) and without (gray) are significantly different. B) Boundary tortuosity of single grafts with permutations resulting in GHE (purple) and without (gray) were significantly different. C) The percentage of tissue within 1 mm of single grafts occupied by scar was not significantly different. D) Histogram of distances between two grafts for all combinations with (orange) and without cooperative GHE (gray). Bolded values denote statistical significance. All statistics were conducted using the Wilcoxon rank sum test. E) Geometry 1 with graft of interest (green) and breakthrough sites (yellow). Other grafts treated as host myocardium for this set of simulations are shown in light blue. Host boundary of graft of interest proximal to (i.e., within 200 µm; red) or distal from (black) any known breakthrough site(s). F) Host isolatedness for the region surrounding this graft of interest. G) Violin plots summarizing host isolatedness metric values for all points along the boundary of the graft of interest shown in E-F H) ROC analysis summarizing predictive power of using host isolatedness values to anticipate the subset of graft-host boundary points across all individual grafts in all histology-based geometries (AUROC=0.85).*

3.5 Discussion

In this study, we used computational simulations to investigate arrhythmogenic properties of single hPSC-CM grafts and combinations thereof in geometries derived from histological images. Our simulations used our previously published population-based approach for representing graft-host electrical coupling in a physiologically plausible way [79]. Our findings suggest that while synergistic cooperation between grafts is possible, the majority of arrhythmogenesis seen in the context of multiple grafts is due to inter-graft complementarity (i.e., redundancy). Practically, the implication is that in the context of realistic multi-graft hPSC-CM patterns resulting from therapeutic injections, if one graft fails to ignite an ectopic excitation, another is likely to compensate. We also observed that geometric features, such as graft area and tortuosity, can significantly impact GHE. The presence of spatially confined tracts of surviving myocardium (i.e., regions of high “host isolatedness”) in the vicinity of graft can also be used to identify possible GHE hot spots. To our knowledge, this is one of the first studies to investigate and characterize realistic graft geometry and assess individual and collective graft impact on arrhythmia.

Currently, cell injections in large animals are performed by intramyocardial injections to both the infarct and border zone in animals with MI (12–14) or in healthy myocardium for those without [131]. Injection schemes typically range from four to 16 injections [49,50,145]. In MI in vivo models, researchers use gross direct inspection or electroanatomical mapping to determine infarct regions [51]. Anywhere between 100 µL to 250 µL of cell suspension is used per injection. Our findings suggest that arrhythmogenicity could be minimized if researchers instead injected smaller quantities of cell suspension to a larger number of locations using a microneedle array or some other comparable approach. This would result in a reduced total area of each engrafted region. If larger grafts are still desired, graft cooperativity could be minimized if cell injections are spaced at least 850 µm apart. However, more work will be needed to assess these new configurations' contractile benefit since our current modeling framework only considers electrophysiology.

Recent attempts to reduce arrhythmogenic consequences of hPSC-CM injection have included pharmacologic treatment and genetic modification of hPSC-CMs. In a recent study by Nakamura et al. [51] clinically available antiarrhythmics were tested to mitigate the risk of VT in an infarcted porcine model. It was found that both amiodarone and ivabradine could enhance survivability following stem cell-induced VT but did not prevent it entirely. In another study, Marchiano et al. [131] hypothesized that spontaneous depolarizations originating from engrafted hPSC-CMs were the source of VT. They found that knocking out genes encoding for hyperpolarization-activated channels (i.e., channels responsible for I_f), T-type calcium channels, and the sodium-calcium exchanger while simultaneously overexpressing the gene encoding for inward rectifier potassium channels, VT did not occur following cell delivery into uninjured porcine hearts. Our work suggests that in addition to making the cells themselves less arrhythmogenic, it might also be beneficial to test more dispersed graft patterns.

Previous computational studies have also investigated the mechanisms leading to VT following cardiac stem cell therapy [75–77,146]. One examined the effects of a heterogeneous distribution of cardiomyocytes on ectopic arrhythmogenicity, reporting that increased cell density and dosage along the infarct boundary led to more ectopic propagation. However, this study only considered one patient-specific human post-MI geometry, using synthetically generated engrafted regions with idealized geometry [75]; moreover, a continuous approximation of graft-to-host electric coupling was used. Our present study differs critically in that it used a population-based approach to represent the complex spatially heterogeneous electrical coupling between graft and host. We believe this approach is critical to reconciling the rapid focal VT phenomena observed in vivo with the experimental in vitro recordings of slow-beating hPSC-CMs. Our population-based approach was necessary since no experimental data is available to provide exact measurements of graft-host coupling at continuous time points.

Another more recent study by Riebel et al. [146] created a computational framework to study hPSC-CM heterogeneity, the effects of the Purkinje system, and how infarct maturation would modulate arrhythmia propensity. In their study, the authors found that a mixture of atrial and nodal-like hPSC-CM exhibited ectopic activity. In contrast, the homogenous ventricular population did not beat under any scenario tested. The authors also explored re-entrant arrhythmia formation following ectopic activity with the addition of both impaired and healthy Purkinje propagation, finding reentry to be most common in acute MI with impaired Purkinje propagation. These findings highlight the importance of uniform maturation in the hPSC-CM electrophysiology and healthy Purkinje propagation to prevent re-entry. Our study does not consider the Purkinje system or hPSC-CM heterogeneity in 3D. Instead, our study focuses on how variability in graft geometry properties may increase the likelihood of focal arrhythmia that has been observed in experimental studies [49,51,54].

Our study has a few other notable limitations. First, due to the large volume of simulations, we chose to run all our simulations with a single graft-host electrical connectivity level of 10%. If we ran our simulations at different connectivity levels, our observations about cooperativity and complementarity might diverge from the current findings. Cooperativity could play a more significant role; however, based on the striking results presented in **Figs. 3.6 C-F**, we surmise that this phenomenon would unlikely surpass the dominant nature of the complementarity effect. It is also important to note that we chose 10% connectivity because, in our previous study, this level was globally the most favorable for the prevalence of GHE [79].

Another limitation of our study is that we chose to model scar as non-conductive, similar to previous work [98,116,147]. Recent studies have shown that nonmyocytes can affect cardiac excitability [120,148], but the connection between hPSC-CMs and nonmyocytes following transplantation is poorly characterized. We previously investigated the effect of slow-conducting scar on arrhythmogenesis and found that slow-conducting scar decreased GHE propensity compared to the same simulations run with non-conductive scar. We chose to use non-conductive scar since those geometries exhibited the highest propensity of GHE [79]. Furthermore, GHE is only a surrogate measurement of focal VT. We did not apply external pacing to mimic sinus rhythm, and it remains unknown whether ectopic beating of engrafted cells in our modeling framework could out-compete sinus rhythm. Finally, we did not exhaustively test how arbitrary modifications of size, shape, and distance would impact GHE in this study. Instead, we focused primarily on actual graft geometries derived from histology images. Prior computational work focused on testing prescribed cell density and dosage, but the boundary conditions only allowed those virtual grafts to exist within a spheroidal cell delivery region [75].

In conclusion, we have presented a deep analysis of how individual grafts and groups of grafts can impact arrhythmogenicity following stem-cell injection. In all three histology-based geometries examined, we found that individual grafts can be arrhythmogenic, and the combination of independently arrhythmogenic grafts contributes most to higher rates of arrhythmia in realistic multi-graft configurations, not synergistic interaction between grafts to create new excitations. This work also provided new insights into experiments that could be used to create a safer target delivery system for hPSC-CM therapy.

3.6 Supplemental Figures

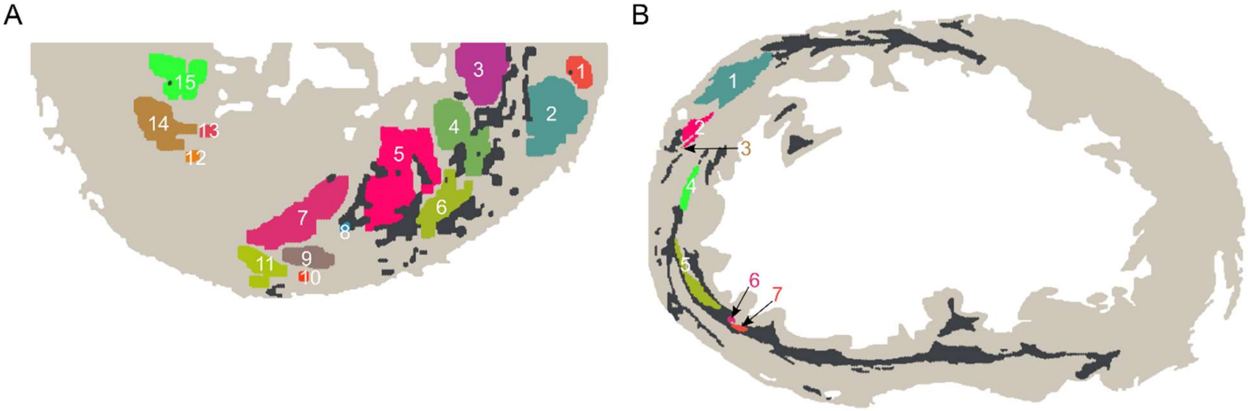

Supplemental Figure 3.1: Individually labeled grafts for A) Geometry 1 and B) Geometry 2

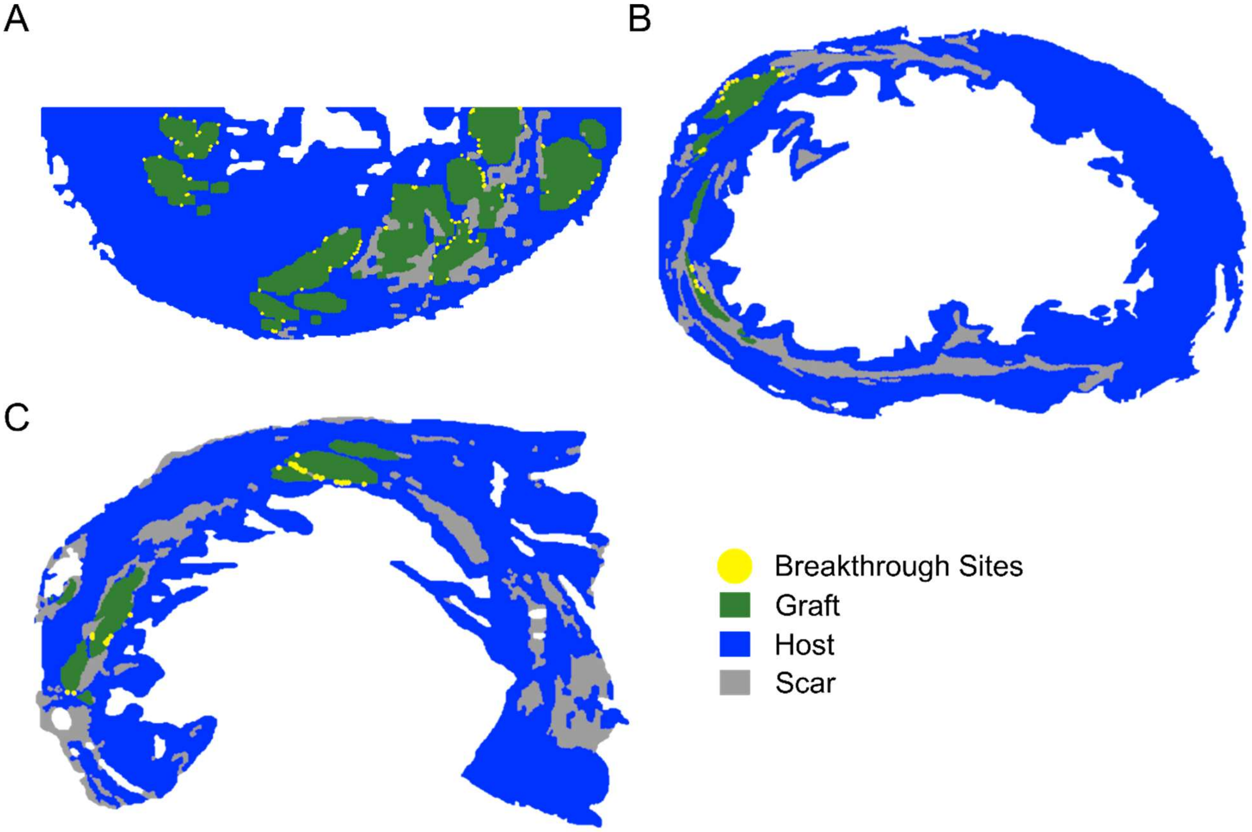

Supplemental Figure 3.2: Activation site for each individual graft of A) Geometry 1, B) Geometry 2, and C) Geometry 3

Chapter 4: Accelerated Intrinsic Beating Rate in Heterogeneously Coupled Stem Cells May Underlie Focal Ventricular Tachycardia in Regenerative Cardiac Therapy

4.1 Abstract

Novel cardiac stem cell therapies seek to replace damaged tissue following a myocardial infarction to prevent heart failure. Human pluripotent stem-cell derived cardiomyocyte (hPSC-CM) therapies are a promising treatment that can remuscularize the heart and improve cardiac function. However, they can be a source of rapid ventricular tachycardia (VT). Electrical mapping studies have suggested this VT is focal, but the true mechanisms remain unknown. Computational simulations may provide new insights into these complex arrhythmias, but current simulation frameworks have not replicated focal VT. In this study, we conduct simulations with biophysically plausible representations of cell injection and the formation of gap junctions between engrafted hPSC-CMs (graft) and host tissue. We examine hPSC-CM ionic models with different intrinsic beating rates (1.1, 2.5, 4.0 Hz) and assess whether any of these conditions can produce focal VT that is adequately rapid and robust to overpower sinus rhythm. Using a population of three human ventricular slice geometries with non-human primate graft patterns, we assessed susceptibility to focal VT. VT was observed with all ionic models but to varying degrees. Our 1.1 Hz model could only produce focal VT with a 40bpm sinus rhythm. Conversely, our faster ionic models could produce VT under all sinus pacing. We also doubled graft size to cover larger infarct areas and found robust VT when the 2.5 and 4.0 Hz models were applied. This work suggests that our computational framework can produce focal VT by increasing hPSC-CM spontaneous beating rate and could help plan future injection schemes.

4.2 Introduction

Myocardial infarction (MI) is a life-threatening cardiac event associated with sudden cardiac death and affects over 3 million people per year [149,150]. During an MI, blood flow to the heart is restricted, leading to cell necrosis and death [151]. If a patient survives the initial MI, they experience a decrease in quality of life that can partly be attributed to the heart's lack of self-regeneration [5,152]. When cardiomyocytes become damaged, they are replaced by scar [11,153]. The presence of scar can lead to adverse structural remodeling and eventual heart failure [154–156]. There are currently no treatment options to replace the damaged myocardial tissue aside from a transplant, where there are limited donors [13,157]. This has created an urgent need for diverse and novel cardiac therapies.

The use of human pluripotent stem cell-derived cardiomyocytes (hPSC-CM) to repair damaged tissue through injections has shown promise in improving cardiac function [55,56,89,158,159]. However, ventricular tachycardia (VT) following hPSC-CM injection remains a concern for cardiac regenerative therapies [49,51,54]. In large animal models, VTs as rapid as 3 Hz are frequently observed within a few days following injection [50,51,54]. Clinical-grade electrical mapping studies have been performed and suggest the VT is focal and originates from hPSC-CM implantation sites [49,54]. Nevertheless, the mechanisms leading to VT remain incompletely understood.

Computational tools can provide valuable insight into arrhythmia mechanisms and susceptibility [95,132,160–162]. Previous computational frameworks have been established to try to investigate focal VT but were unable to fully replicate this phenomenon in silico with sinus pacing [75–77,79]. This could be due to the cell scale hPSC-CM models spontaneously beating at a rate between 0.58 Hz and 1.9 Hz [79,163,70,69]. These models are all based on in vitro data taken from cells on tissue culture plastic. During the differentiation process, the maturity of hPSC-CM is challenging to control, and the end result most closely resembles that of neonatal cardiomyocytes [62,164,165]. Currently, no published data exists that describes the electrophysiology of these cells following in vivo engraftment. We hypothesize that the beating rate of hPSC-CM must accelerate to achieve rapid focal VT in silico. Thus, we set out to test if rapid focal VT was possible by only modifying the spontaneous beating rate of the hPSC-CM in silico cell scale models.

Previous work in our lab altered an existing hPSC-CM ionic model to beat at 1.9 Hz and investigated heterogeneous electrical coupling between graft and host myocardium. We found that ectopic beats originating from the graft could lead to host excitations when the boundary was varied [79]. However, we never tested whether this phenomenon could be sustained in the presence of sinus pacing (i.e., if the arrhythmic events we simulated reflected sustained VT, as opposed to the theoretical possibility of ectopic excitation). Building off our previous framework, we generated three new 2D human slice geometries for this study and applied three graft patterns derived from histological image analysis of hearts following cell injection in non-human primates (NHPs). We tested three intrinsic hPSC-CM beating rates between 1.1 Hz and 4.0 Hz and three sinus rates between 40-80 beats per minute (bpm) to determine if rapid focal VT could occur under any of these conditions. We also looked at if doubling graft size would increase the prevalence of focal VT.

4.3 Methods

4.3.1 Cell- and Tissue-Scale Electrophysiological Modeling

In the engraft hPSC-CM region (graft), we tested three ionic hPSC-CM models with spontaneous beating rates of 1.1, 2.5, and 4.0 Hz (**Fig. 4.1**). An existing model of hPSC-CM membrane kinetics without modification [69] was used for 1.1 Hz simulations **(Fig. 4.1 A)**. Due to the absence of data about these cells' behavior in vivo, we modified the existing model to create two hypothetical faster-beating hPSC-CMs. We first create a 2.5 Hz model by increasing the conductance values of rapidly and slowly activating delayed rectifier potassium (g_{Kr} and g_{Ks})

currents by a factor of three and reducing the inward rectifier potassium (g_{K1}) current to zero **(Fig. 4.1 B)**. Our second model that had a spontaneous beating rate of 4 Hz was generated by increasing the baseline models t-type calcium (g_{CaT}), hyperpolarization-activated (g_f, i.e., "funny"), g_{Kr}, and $g_{Ks,}$ current conductance values by a factor of 11.5 and reducing g_{K1} to zero **(Fig. 4.1 C)**. To ensure steady state conditions before inserting these variants into organ-scale geometries, each hPSC-CM representation was allowed to beat spontaneously for 120 cycles before we saved the model state at the time of the minimum diastolic potential (MDP, i.e., the most negative membrane voltage of the action potential).

Three 2D human slice geometries were extracted from existing post-MI 3D ventricular geometries comprising healthy myocardium, border zone, and scar (**Fig. 4.1 D**) [166]. We identified three geometries for the existing cohort with two fully transmural infarcts but varying degrees of border zone. We also picked one with a more endocardial infarct with a large border. A 1 mm of healthy myocardium was preserved on either side of the infarct to ensure wavefront propagation and reduce computational cost. Three histology-derived NHP hPSC-CM injection patterns from our previous study [79] were superimposed onto the new slice geometries at a 1:1 scale (**Fig. 4.1 E-G)** or at a 2:1 scale in imaging software **(Fig. 4.1 H)** (GNU Image Manipulation Program). All grafts were applied to regions that followed the contour of the infarct but were situated near healthy myocardium to assess arrhythmia propensity. We made this decision because scar during hPSC-CM cell transplantation, cells are injected both into the ischemic region and border zone [49,51]. We chose not to focus too closely on the ischemic regions because scar is modeled as non-conductive in our simulation, preventing propagation of electrical activity. For slice Geometry 1 and 3, 1:1 scale graft patterns were applied in two locations on either side of the transmural scar. For Geometry 2, 1:1 scale graft patterns were applied in three areas. If the placement of graft patterns resulted in some engraft regions being outside of the slice, that graft pattern was placed in a new region. When graft patterns were scaled up to 2:1, grafts were placed throughout the infarct to cover as much scar as possible, and graft proximity was not preserved. All geometries and graft patterns are shown in **Supplemental Figure 4.1**.

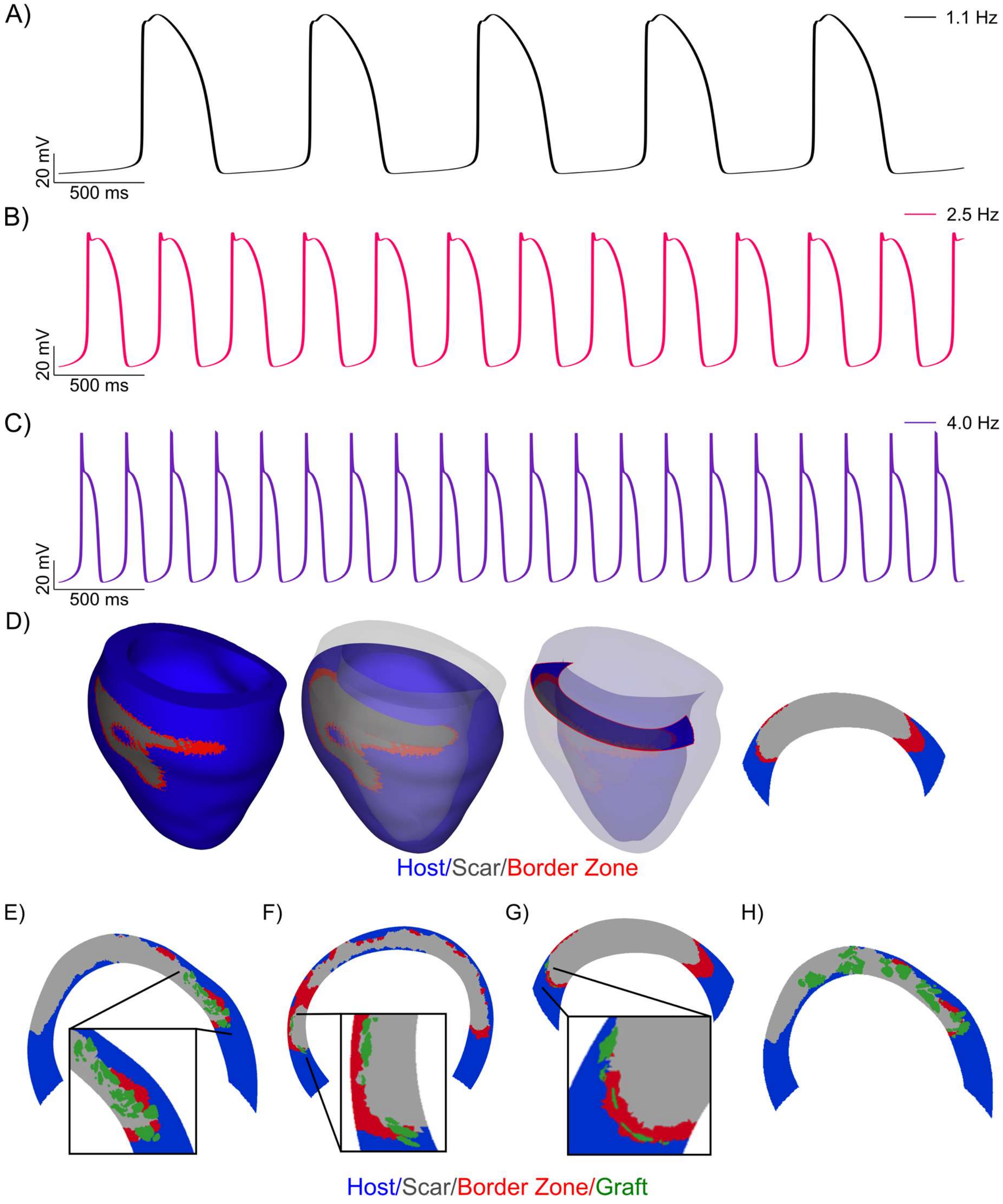

Figure 4.1: Three ionic models and three graft patterns were tested. *A-C) Action potential traces of published model (black) beats at 1.1 Hz. The published action potential model was*

modified to beat to B) 2.5 Hz and C) 4.0 Hz. D) Example segmentation used to create slice geometries E-F) Representative examples of the three human geometries with three non-human primate (NHP) graft patterns applied at a 1:1 scale H) Representative examples of Geometry 1 with a graft pattern at a 2:1 scale.

Similar to prior work, in our tissue scale simulations, ventricular [109], border zone [98], and above hPSC-CM cellular models were used in the corresponding regions; the scar was modeled as non-conductive [167,116,147,168]. To generate our population of models, we used an established model for graft-host coupling to explore ectopic excitation in a probabilistic manner. A subpopulation of 40 varied graft-host boundary coupling configurations was created for each human slice with an hPSC-CM graft-to-host intercellular electrical connectedness of 20%. As in our previous studies, this was done using a discontinuous finite element method to disconnect 80% of elements along each boundary between graft and host regions. Tissue scale simulations were run with electrical stimulation from two endocardial points (4×), delivered every 1500 ms, 1000 ms, or 750 ms to mimic sinus rhythms of 40 bpm, 60 bpm, and 80 bpm, respectively (**Fig. 4.2**). We chose to test a variety of sinus beating rates to cover a large portion of the population who have a resting heart rate above or below 60 bpm [169,170]. VT was considered a graft-driven beating rate faster than 100 bpm [171,172].

Similar to other studies, the monodomain finite-element approximation governed the propagation of electrical activity in our simulations [79,137,168,173]. This was done by numerically solving the partial differential equation for each tissue type representing the myocardium's electric flow. Membrane kinetics were described by solving the algebraic and ordinary differential equations for each cellular electrophysiology model applied to ventricular host, ventricular border zone, and hPSC-CM graft regions. Also similar to prior work [98], conductivity tensor values for host myocardium in the longitudinal and transverse directions with respect to fiber orientation were set to σ_L = 0.255 S/m and σ_T = 0.0775 S/m, respectively.

Conductivity tensor values for border zone with respect to fiber orientation were set to σ_L = 0.255 S/m and σ_T = 0.00775 S/m [98]. In cases, engrafted hPSC-CMs (grafts) areas were modeled with an isotropic conductivity tensor of $\sigma_{hPSC\text{-}CM}$ = 0.0775 S/m [79]. All bioelectrical simulations were conducted using Version 7.0 of openCARP [118], and the resulting data were visualized using the meshalyzer tool. Both are available for non-commercial use (http://opencarp.org/). This work was facilitated using advanced computational, storage, and networking infrastructure provided by the Hyak supercomputer system at the University of Washington.

4.3.2 Pseudo-Electrocardiogram Generation

To analyze graft-initiated excitations during sinus rhythm, pseudo-electrocardiograms (ECGs) were generated by placing electrodes in two locations distal to scar on the left and right side of each slice geometry **(Fig. 4.2).** Similar to previous work [174,175], the difference between extracellular potential values of the electrodes was calculated to construct our pseudo-ECGs. VT was defined as the average beats per minute (bpm) exceed 100 at one the pseudo-ECG leads. A Python code was generated to automate this process. Briefly, this code took the absolute value of the derivative of each signal, found the time of each peak, and calculated the average bpm for the entire signal. Python libraries Pandas [140], NumPy [141], and SciPy [143] packages were used. An arrhythmogenicity metric was created for each graft pattern by averaging the VT observed in of our population of models regardless of graft location and normalizing the data out of one. This metric was then used to generate our heatmaps.

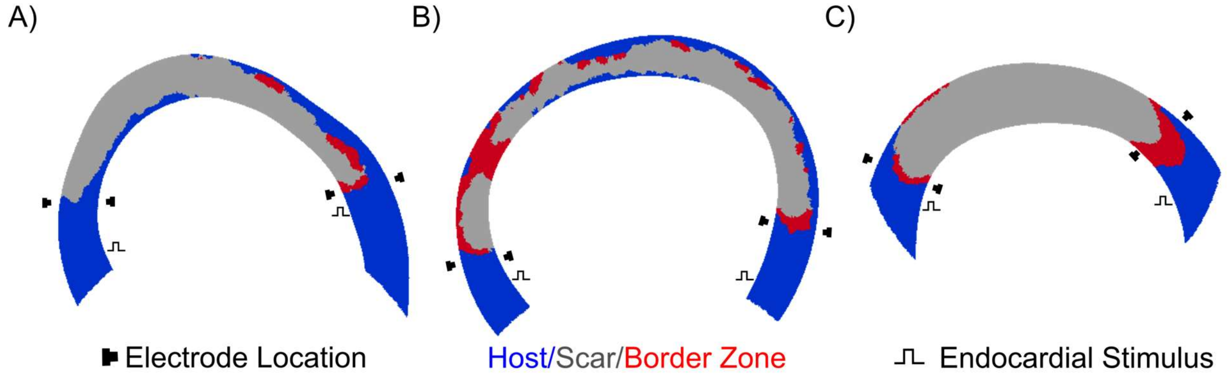

Figure 4.2: Sinus pacing and electrode locations for pseudo-ECGs. *A-C) The left and right leads pseudo-ECGs are generated by taking the difference between signals of the electrodes on the endo and epicardial surface for A) Geometry 1, B) Geometry 2, and C) Geometry 3. Electrode locations are shown. Endocardial pacing sites are also shown.*

4.4 Results

Lowest intrinsic hPSC-CM beating rate rarely causes in silico focal VT

Looking first at the slowest spontaneous beating ionic model [69], we examined if rapid focal VT was possible with simulated sinus rates of 40, 60, and 80 bpm. For the example shown in **Figure 4.3**, ectopic beats originating from the graft could propagate, and the host tissue recovered before each sinus beat **(Fig. 4.3 A)**. This created an average beating rate of 105 bpm in our left pseudo-ECG trace (Fig. 3B). Due to the transmurality of the scar in this model, the right lead shows that sinus rhythm was maintained (**Fig. 4.3 C**). Interestingly, when we looked at all graft patterns in all human slice geometries, the total VT incidence was low. Only 10-11% of our simulations with graft 1 in human slice Geometry 1 and 2 exhibited this behavior. All other graft patterns did not produce VT. Human slice Geometry 3 also had no VT (**Fig. 4.3 D-F**).

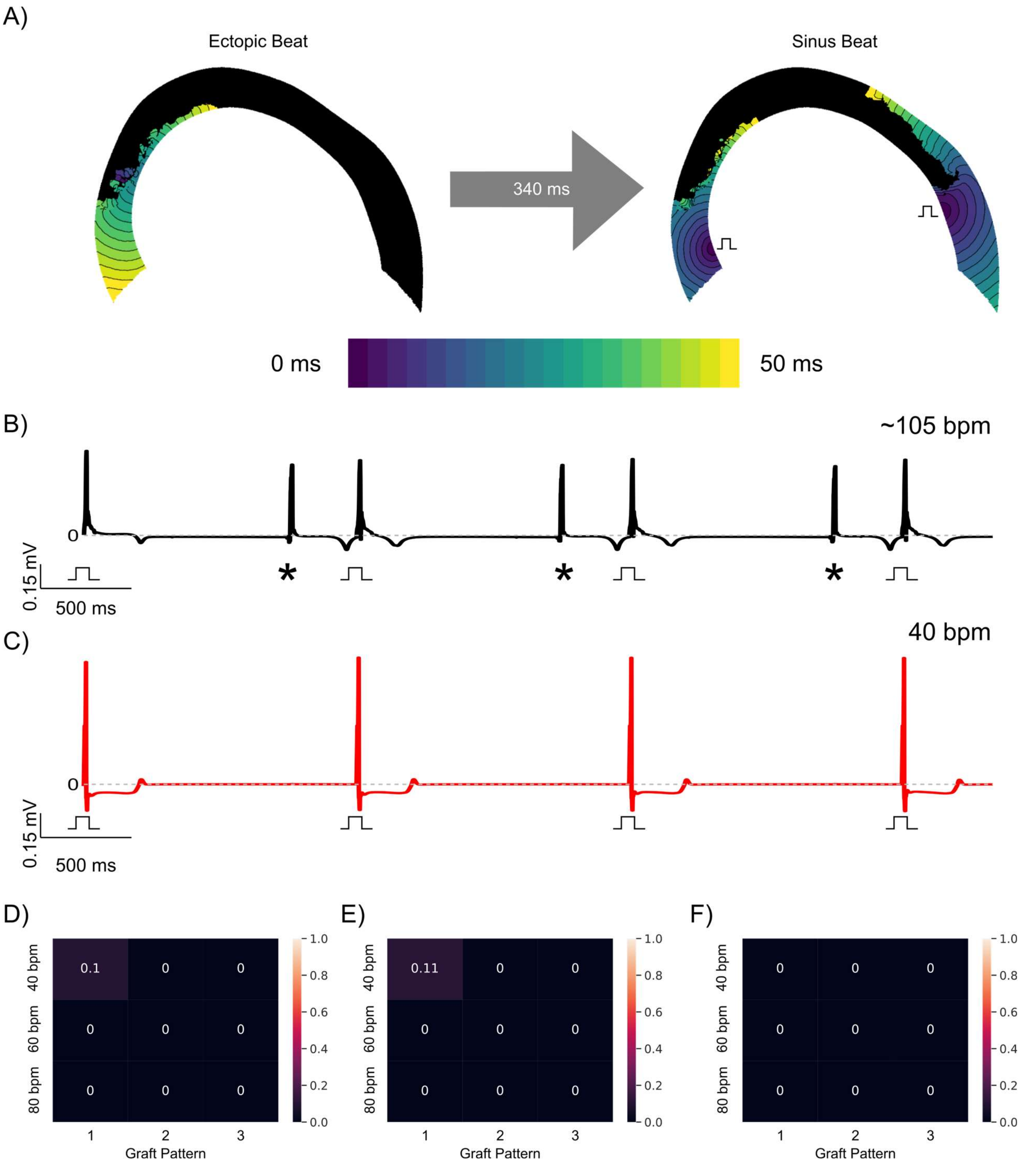

Figure 4.3: When a 1.1 Hz ionic model was applied, a VT-like beating rate was only observed with a sinus beating rate of 40 bpm. *A) Activation map of the first ectopic beat followed by a successful sinus beat 340 ms later. B) Left pseudo-ECG lead of Geometry 1 with VT is shown. C) Example of 40 bpm sinus pacing observed in the right pseudo-ECG lead of the same geometry.*

D-F) Heatmap of simulations with focal beating originating from grafts in Geometries 1-3. Ectopic beats are denoted by an asterisk

Faster intrinsic hPSC-CM beating rate more consistently causes in silico focal VT

We then assessed how this behavior might change when our 2.5 Hz model was applied and found a larger portion of our simulations resulted in VT (**Fig. 4.4**). In the example shown of Geometry 3 in **Figure 4.4**, an ectopic beat originating from the graft occurs on the right side of the model at 880 ms. It traveled slowly through border zone tissue prior to host excitation. Due to the timing of this ectopic beat, when sinus pacing occurs 20 ms later, the tissue is still refractory and fails to excite the host myocardium. Further investigation of the spontaneous beating rate showed that the right side increased from 60 bpm to 122 bpm (**Fig. 4.4 B-C**). Looking at our data in aggregate, we found that all graft patterns in all geometries were capable of producing focal VT but to varying degrees (**Fig. 4.4 D-F**). Across all geometries, graft pattern one exhibited the highest amount of VT. Interestingly, the incidence of VT seemed to increase slightly as sinus pacing increased. Graft pattern two, on the other hand, had a low propensity of VT in all cases. Human slice geometry two also appeared to have the most arrhythmogenic geometry, while human slice geometry three was least arrhythmogenic.

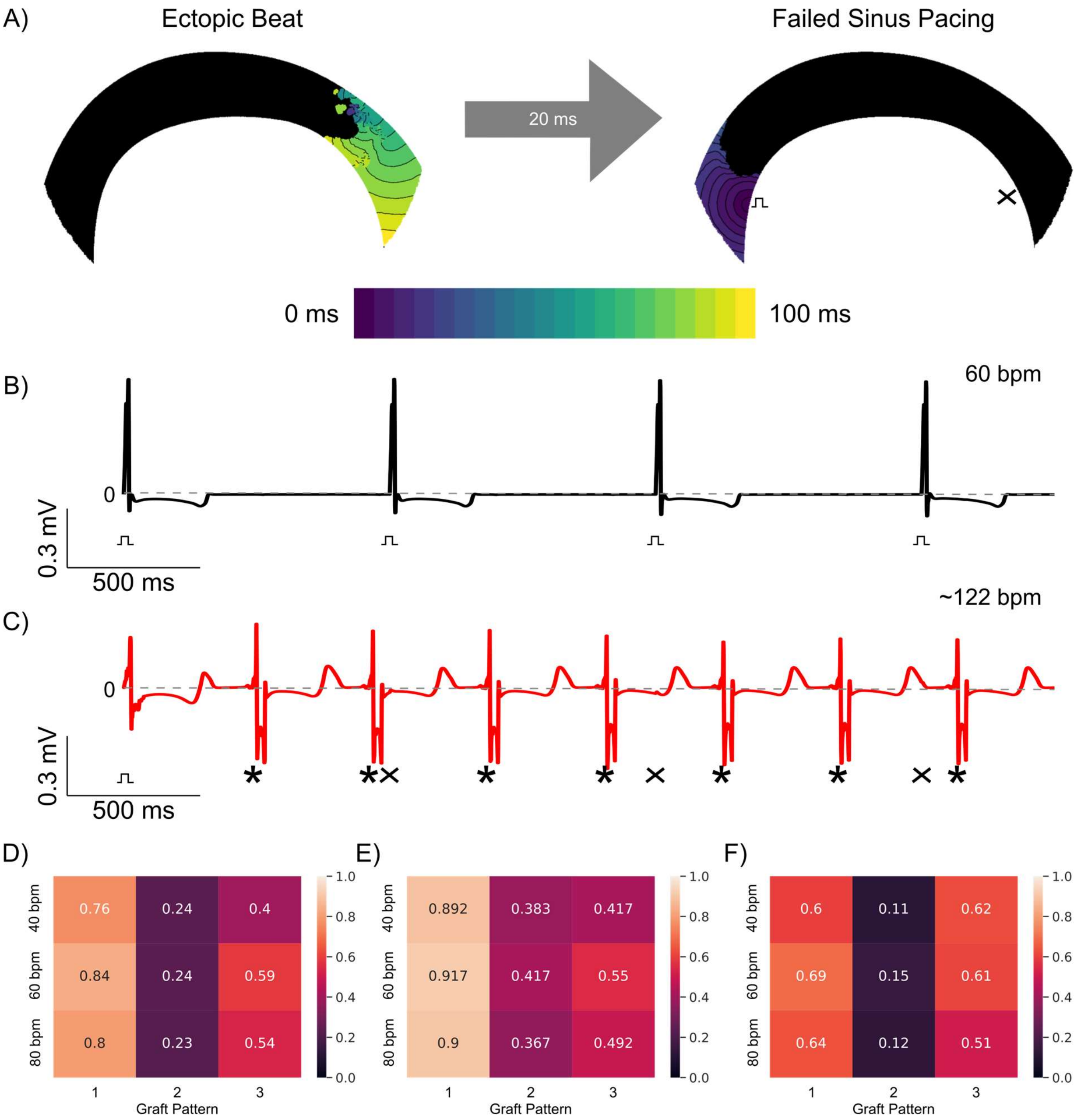

Figure 4.4: With a 2.5 Hz ionic model applied to grafts, focal ectopy is observed at all sinus pacing rates. *A) Activation maps of ectopic beat followed by failed sinus pacing in Geometry 3. B) A 60 bpm sinus rhythm was observed on the left pseudo-ECG. C) Right pseudo-ECG trace of the representative example shows a beating rate of 122 bpm with ectopic beats outcompete sinus rhythm D-E) Heatmap of the proportion of simulations with VT grafts in Geometries 1-3. Asterisks denote ectopic beats. Failed sinus pacing is shown with X.*

When we applied our 4 Hz ionic model to our population, we saw a further increase in the number of simulations resulting in focal VT. In the representative example shown for human geometry two, following the initial sinus pacing beat, ectopic beats originating from the graft overwhelm most sinus pacing (**Fig. 4.5 A-C**). The third sinus beat as shown in the activation maps resulted in fused beat on the left side of the geometry followed 200 ms later by an ectopic beat **(Fig. 4.5 A)**. Looking at pseudo ECG both the left and right lead we saw left lead have a 202 bpm (**Fig. 4.5 B**) rhythm while the right maintained 80 bpm sinus pacing (**Fig. 4.5 C**). When looking at all simulations in aggregate, we found that regardless of which graft pattern and geometry were at least 70% of simulations resulted in focal VT regardless of the sinus pacing. Both graft patterns one and three were highly arrhythmogenic regardless of human slice geometry. Graft pattern two was less so, especially in our second human slice geometry where it averaged a VT propensity of 71.7% (**Fig. 4.5 D-F**).

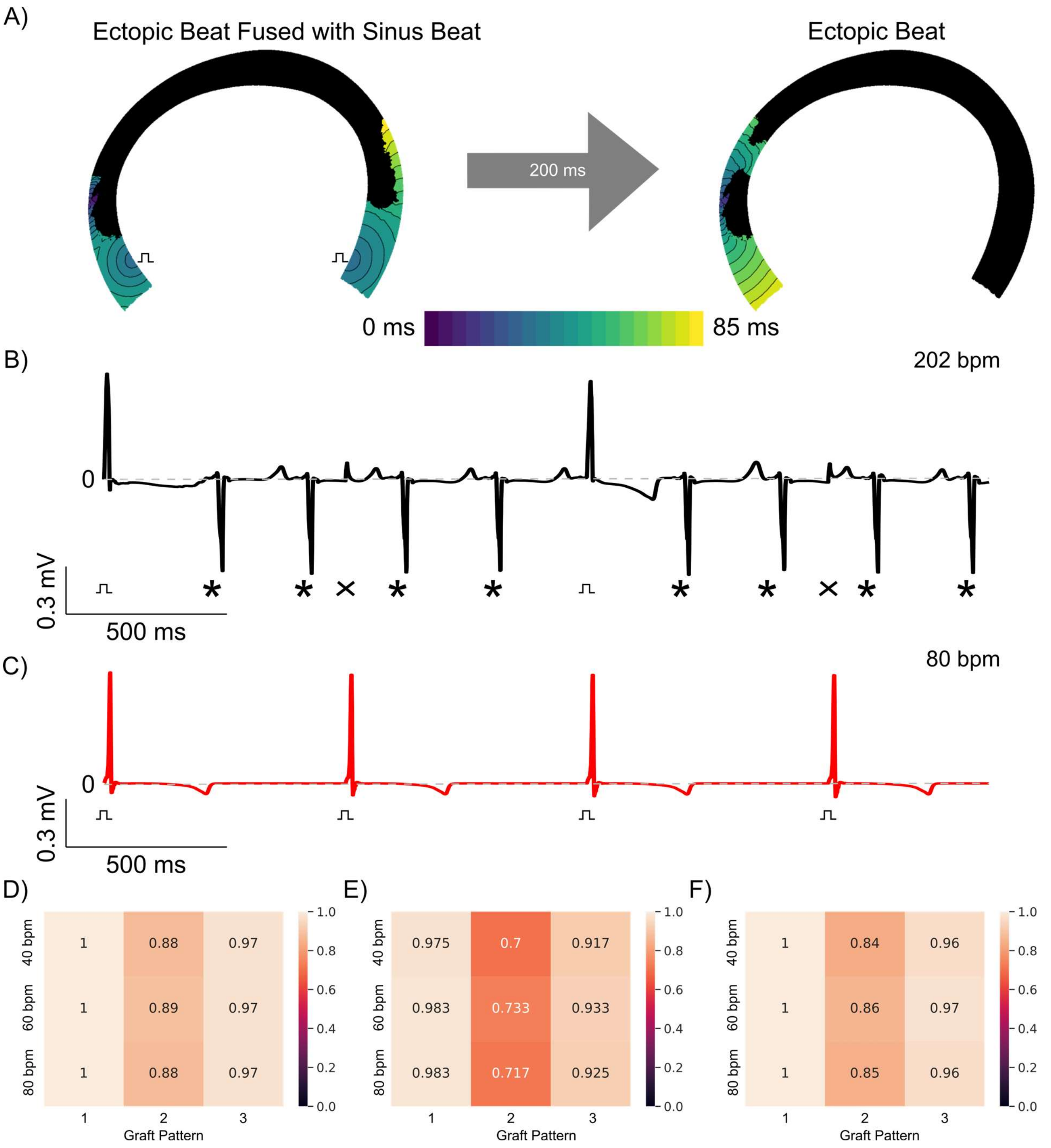

***Figure 4.5: Rapid VT was observed for all sinus rates with a 4 Hz ionic model applied to graft regions**. A) Activation maps of ectopic beat fusing with sinus beat followed by another successful ectopic beat for human geometry two graft pattern two. B) Left pseudo-ECG showed rapid focal VT of 202 bpm C) Right pseudo-ECG lead shows 80 bpm paced sinus rhythm. D-F)*

Heatmap of simulations with focal beating originating from grafts in Geometries 1-3. Ectopic beats are denoted by asterisks. Failed sinus pacing is shown with X.

Doubling graft size increased arrhythmia susceptibility

While superimposing the grafts from non-human primates at a 1:1 scale in the human geometries was informative, it is possible the limited scar coverage of these grafts would lead to a failure to achieve the desired therapeutic benefit (i.e., effective remuscularization). Thus, we examined how doubling the graft size would affect arrhythmogenic propensity under the same three sinus rhythms using the same ionic models described above. We found that in all cases, doubling graft size increased the incidence of VT regardless of human geometry or which ionic model was tested (**Fig. 4.6**). With larger graft sizes scaled to proportionally match human geometry, the average incidence when the 1.1 Hz model was applied was only 0-3% of all simulation with a 40-bpm sinus rhythm (**Fig. 4.6 A**). When the graft size was, the average incidence of VT increased to 20-31%. Interestingly, even with a larger graft size, no VT was observed when the sinus rhythm was greater than 40 bpm. For both the 2.5 Hz and 4.0 Hz ionic models, VT incidence was robust when graft size was doubled and occurred in almost all simulations (**Fig. 4.6 B**).

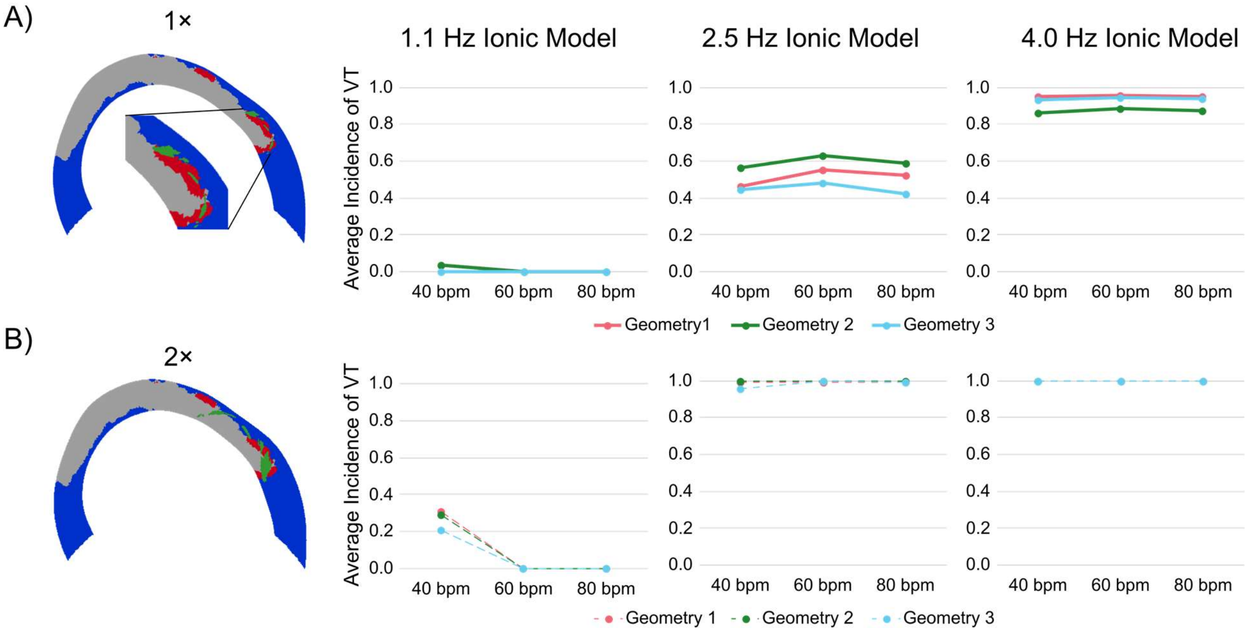

Figure 4.6: When graft size was doubled, all model populations were more prone to VT. *A) 1× results. B) 2× results. Column 1 shows a representative example of human Geometry 1 with graft two applied at either 1× scale or 2× scale. Columns 2-4 show the average incidence of VT when the 1.1 Hz, 2.5 Hz, and 4.0 Hz ionic models were applied.*

4.5 Discussion

In this preliminary study, we used our population-based computational framework to investigate how hPSC-CM intrinsic beating rate at the cell scale can manifest into focal VT at the tissue scale in human ventricular slice geometries. To our knowledge, this is the first computational study to show that graft-originating focal VT can outcompete sinus rhythm. This is also the first study to use human ventricular MI geometry and assess how graft patterns derived from histology images acquired from the hearts of animals used in pre-clinical studies might behave in these larger hearts. Our findings show rapid VT was observed for all sinus rhythms only when the hPSC-CM intrinsically beat at 2.5 Hz or higher (**Fig. 4.3-4.6**). We also found that we could consistently get rapid VT in almost all cases when the graft size was doubled, so long as a 2.5 Hz or higher ionic model was used (**Fig. 4.6**). These findings provide evidence in support of one hypothesis explaining the origins of these focal VTs: following engraftment, regardless of how cells behaved in the dish, some form of phenotype switching occurs, and the cells become pacemaker cells with faster spontaneous excitation rates. This could be due to environmental factors such as paracrine signaling or the mechanical properties of the heart and its environment, neither of which are captured in our simulation framework.

Previous computational frameworks have used patient-specific post-MI ventricular geometries to assess stem cell therapy arrhythmogenicity. In a study by Yu et al. [75], two human post-MI geometries were used with engrafted cells that were synthetically placed within the myocardium. They found that ectopic beats originating for the grafts depended on delivery site location and how patchy they modeled their grafts. However, they used a hPSC-CM model that could only spontaneously beat at 37.5 bpm and did not apply sinus pacing. In their follow-up study [76], using an integrated cardiac patch in human post-MI geometries, they never saw the ectopic beating rate exceed the intrinsic beating rate of the hPSC-CM model and cannot outcompete a 60 bpm sinus rate. Our study differs in its use of a hypothetical hPSC-CM intrinsic beating rate that is much faster than in vitro data to see if hPSC-CM can function as a focal source in larger human geometries.

Our study has a few notable limitations. First, our modifications to the ionic model are not based on experimental data. The original model [69], with a spontaneous beating rate of 1.1 Hz, is based on data from the electrophysiology of different experimental preps of hPSC-CMs that were combined to create a model that recapitulated the generalized phenotype of a healthy hPSC-CM. We made our modifications to increase the beating while maintaining a reasonable ventricular-like action potential shape. This is not the first time modifications have been made to this model or ventricular models to get them to behave differently. In that same study by Kernik et al.[69], the authors generated a population of hPSC-CM models to better capture the heterogeneity in hPSC-CM behavior by modifying I_{Na}, I_{CaL}, I_{K1}, I_{Kr}, and I_f. These parameters were varied to be within the experimentally observed range. Still, it was found that changing the parameter kinetics to the median value ± standard deviation strongly impacted action potential morphology. That modification we made to the model altered the same current apart from I_{Na}. In a study by Yu et al. [77], the authors modified the Luo-Rudy I guinea pig ventricular myocyte model to create an oscillatory graft-like cardiomyocyte. They did this by adding a constant depolarization current that they claim was analogous to a funny-current (I_f). In their study, the authors were still unable to conclude how focal VT was possible. On the other hand, our study made hypothetical changes to an hPSC-CM model that may not be realistic but are a starting point with action potentials that look reasonable and minimize the number of parameters we altered.

Another limitation of our study is that we only examined these models' behavior with a graft-host coupling level of 20%. Due to our previous work [79] on which this study is built, we believe that similar trends would have been observed with the wax and wane of VT as the coupling increased and then decreased. We chose not to focus on that for the purpose of this study due to modifying multiple other factors, such as intrinsic beating rate and paced sinus rhythm. Additionally, two out of three human geometries have fully transmural scars. Like other modeling frameworks, we model scar as non-conductive, which limits where grafts could be placed that could theoretically excite the host myocardium. While this is a limitation, we placed grafts in multiple locations along the scar-host, scar-border zone, and border zone-host boundary to gain more insights into how these different environments could affect ectopic excitations. Finally, this study did not test whether micro-reentry within grafts could produce the faster beating rates needed for rapid VT. These micro-reentrant circuits can be masked on anatomical mapping studies as a focal VT, but no one has created a successful framework to test this hypothesis.

In conclusion, we create a computational framework that can produce focal VT regardless of sinus pacing in human geometries. This framework is now well suited to work in tandem with our experimental colleges to test new hypotheses about graft placement and distribution to prevent focal VT following cardiac stem cell therapy. This will help us get one step closer to improving the safety profile of this proposed therapy.

4.6: Supplemental Figures

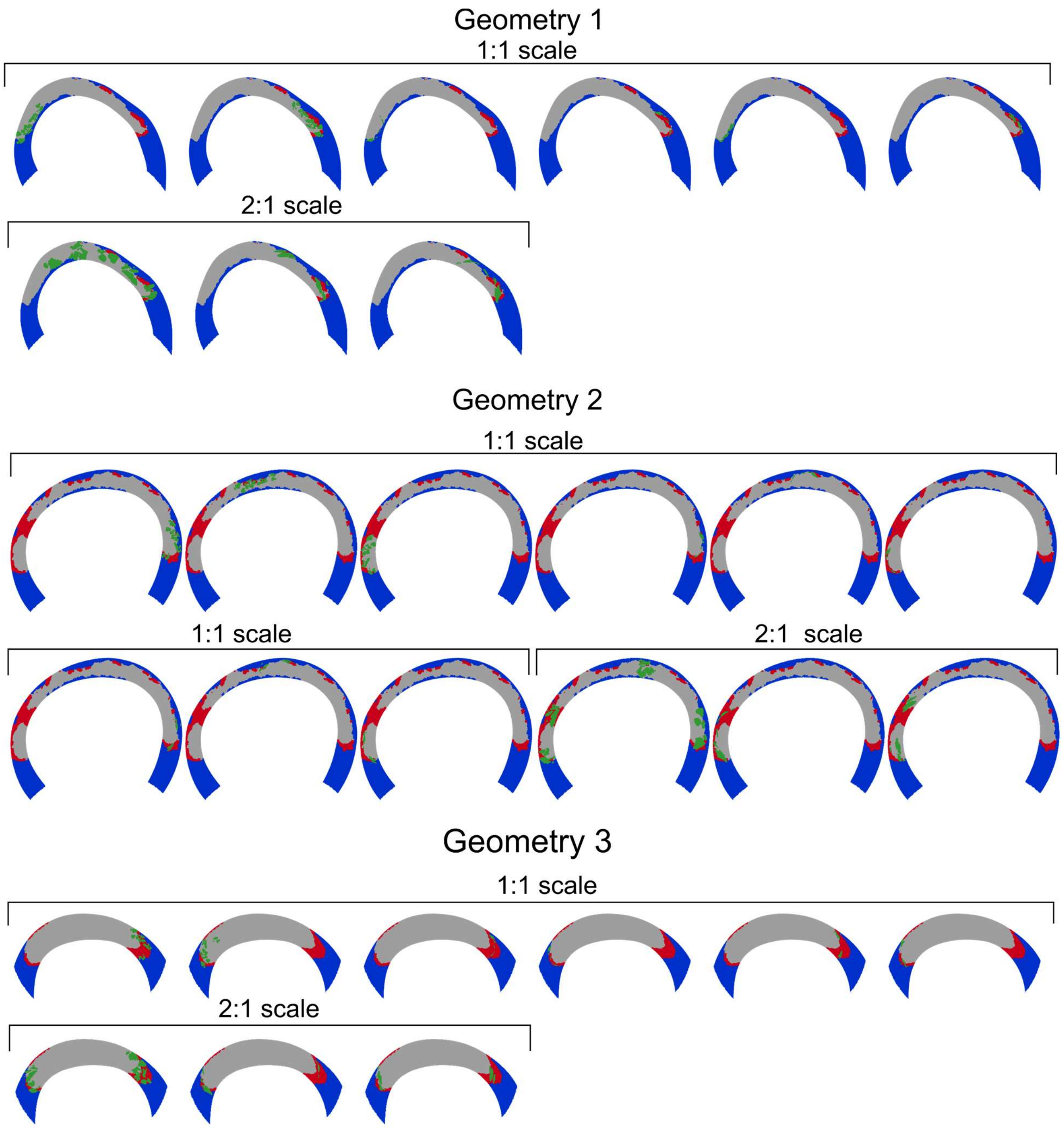

Supplemental Figure 4.1: *All model geometries and graft patterns are shown. Graft patterns are imposed at a 1:1 scale or a 2:1 scale to host tissue.*

Chapter 5: Conclusion

Cardiac regenerative therapies have come a long way over the past few decades, and hPSC-CM remains a promising therapy candidate. Both epicardial patches and intramyocardial injections have been shown to improve cardiac function [17,29,49]. However, there are still concerns with epicardial patches' lack of electrical integration [29] and hPSC-CMs' lack of maturity and proarrhythmic activity [17,51,62]. Current approaches to mitigate the risk through gene edits and antiarrhythmics have brought us one step closer to enhancing the safety profile of hPSC-CMs [51,66]. Still, more work is needed to uniformly control these cells' maturity. A greater understanding of the true mechanisms leading to VT following cell therapy is also required prior to large therapeutic implementation.

Computational models are an important tool for helping us understand focal VT using a multiscale approach. The work presented in this dissertation established in silico models for understanding focal VT following stem cell therapy. In Chapter 2, histology-derived slice models were used to test if varied graft-host coupling could partially explain the transient phenomena of focal VT. We found that a Goldilocks zone existed when grafts were coupled just enough for focal VT to escape the graft and excite the host without source-sink match occurring. We also found this phenomenon to be geometrically variable and that many of these graft patterns can still be arrhythmogenic even when in slow-conducting and healthy myocardium [79]. Chapter 3 explored the arrhythmogenic consequences of individual and groups of grafts using a population-based approach. We found that many grafts had at least one electrical coupling configuration where graft-host excitation could occur. We also discovered that total graft area, tortuosity, and isolation of host regions near graft could be used to pinpoint arrhythmogenic regions. Finally, in Chapter 4, we create a computational model to explore how intrinsic hPSC-CM beating rate affects VT propensity. We found that current in vivo data does not capture a fast enough intrinsic rate for VT to outcompete sinus rhythm, except in some cases with bradycardia. These findings indicate that other factors encourage these cells to phenotype switch into a more pacemaker-like cell and beat much faster.

While the presented work has not given us a definitive answer into all the mechanisms leading to focal VT following cardiac stem cell therapy, it has helped us generate new hypotheses that warrant further in vivo testing. In Chapter 2, we found that the evolution of graft-host coupling was conducive to graft-initiated arrhythmias. We hypothesize that overexpression of connexin 43 may diminish or prevent focal VT (**Fig. 5.1 A**). In that chapter, we also tested how different properties of scar may affect arrhythmogenic propensity. We found that no arrhythmia can occur due to the scar being non-conductive in our models if cells are injected into the scar. To our knowledge, no one has looked at the potential therapeutic effects of injecting stem cells into scar alone (**Fig. 5.1 B**). We believe this experiment will answer important questions such as how proximal cells must be to healthy myocardium for cell survival and help computational modelers to better understand the properties of the infarcted heart and whether dense scar should be modeled as non-conductive. In Chapter 3, our findings showed us that host isolatedness and graft area were important for arrhythmogenesis. Therefore, we hypothesize that smaller injections spread over a larger area would decrease arrhythmogenicity, a conjecture that would warrant future in vivo study (**Fig 5.1 C**). This could be important for designing new injection tools such as microarrays.

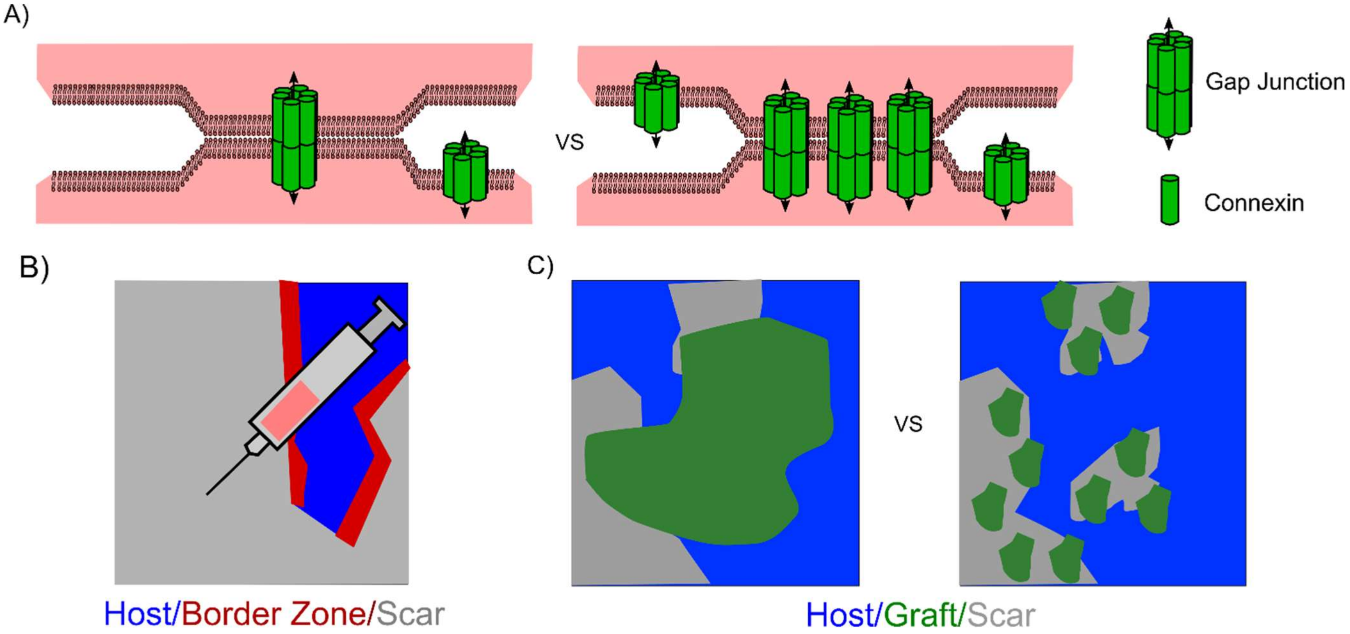

***Figure 5.1: Schematics of three hypotheses we believe warrant in vivo testing**. A) Over-expression of connexin proteins may reduce arrhythmogenic burden following stem cell therapy. B) Injecting stem-cell therapies into scar tissue only could prove to be cardioprotective. C) Smaller injections spread over a large area may decrease arrhythmia susceptibility compared to a large single injection.*

In addition to the outline of in vivo studies, advancements in cardiac computational modeling also hold great potential for helping us understand the arrhythmia mechanism of stem cell therapies and potential therapeutic benefits. While current computational models hold potential, advancements to cell-scale modeling of hPSC-CMs remain essential. Currently, only one electromechanics model of hPSC-CMs exists [176], which has not yet been applied to the tissue or organ scale. Regardless of whether we can create new hPSC-CM models or alter the existing ones, a better reflection of experimental electrophysiology data and a reduction of computational cost is needed. Investigations could then be done to look at new injection schemes' effects on arrhythmia susceptibility and improve cardiac contractility. More work is also needed to evaluate the EP properties of post-MI scar tissue. As stated above, scar is currently modeled as non-conductive which may not accurately represent acute vs. chronic MI.

While the work in this dissertation has focused solely on 2D slice models with realistic graft patterns, improvements to current imaging modalities and contrast agents are needed to create accurate 3D models with engrafted cells. One recent study has used diffusion tensor imaging of ex-vivo Guinea pig hearts with engrafted cells [177], but this technique has yet to be tried in live animals. Leveraging machine learning or neural networks may also prove advantageous in creating better image segmentation, allowing for histology images to be used. If we can make more accurate 3D computational models of engrafted stem cells, we can better assess if other mechanisms, such as reentry due to myocardial isthmuses, could also impact injection locations. The effect of the Purkinje system and possible reintegration also warrants further exploration. A previous computational modeling study attempted to understand the electrophysiologic consequence of reintegration but only examined the effect that engrafted cells may have when coupled to a small segment of the right bundle branch [75]. Additionally, a greater understanding of the pig Purkinje system following stem cell injection would also be helpful in uncovering why stem cell-originating VT is lethal in this pre-clinical model. At this time, it is hypothesized that VT is more lethal because pigs have a more transmural Purkinje system compared to non-human primates and humans [178,179]

Computational models represent a powerful tool for understanding cardiac regenerative therapies and arrhythmias. The ability to model subcellar changes systematically and see the effects at the tissue and organ scale is a significant advantage. Pairing with in vitro and in vivo models, we can generate new hypotheses to help us understand the complex phenomena of arrhythmia. If we can answer the above questions, we will be one step closer to aiding individuals suffering from heart failure following an MI.

References

[1] Nowbar AN, Gitto M, Howard JP, Francis DP, Al-Lamee R. Mortality from ischemic heart disease: Analysis of data from the world health organization and coronary artery disease risk factors from NCD risk factor collaboration. Circulation: Cardiovascular Quality and Outcomes 2019;12. https://doi.org/10.1161/CIRCOUTCOMES.118.005375.

[2] Khan MA, Hashim MJ, Mustafa H, Baniyas MY, Al Suwaidi SKBM, AlKatheeri R, et al. Global Epidemiology of Ischemic Heart Disease: Results from the Global Burden of Disease Study. Cureus n.d.;12:e9349. https://doi.org/10.7759/cureus.9349.

[3] Lu L, Liu M, Sun R, Zheng Y, Zhang P. Myocardial Infarction: Symptoms and Treatments. Cell Biochem Biophys 2015;72:865–7. https://doi.org/10.1007/s12013-015-0553-4.

[4] Mollon L, Bhattacharjee S. Health related quality of life among myocardial infarction survivors in the United States: a propensity score matched analysis. Health Qual Life Outcomes 2017;15:235. https://doi.org/10.1186/s12955-017-0809-3.

[5] Laflamme MA, Murry CE. Heart regeneration. Nature 2011;473:326–35. https://doi.org/10.1038/nature10147.

[6] Richardson WJ, Clarke SA, Alexander Quinn T, Holmes JW. Physiological implications of myocardial scar structure. Comprehensive Physiology 2015;5:1877–909. https://doi.org/10.1002/cphy.c140067.

[7] Konstam MA, Kramer DG, Patel AR, Maron MS, Udelson JE. Left ventricular remodeling in heart failure: current concepts in clinical significance and assessment. JACC Cardiovasc Imaging 2011;4:98–108. https://doi.org/10.1016/j.jcmg.2010.10.008.

[8] Awada HK, Hwang MP, Wang Y. Towards comprehensive cardiac repair and regeneration after myocardial infarction: Aspects to consider and proteins to deliver. Biomaterials 2016;82:94–112. https://doi.org/10.1016/j.biomaterials.2015.12.025.

[9] Francis Stuart SD, De Jesus NM, Lindsey ML, Ripplinger CM. The crossroads of inflammation, fibrosis, and arrhythmia following myocardial infarction. Journal of Molecular and Cellular Cardiology 2016;91:114–22. https://doi.org/10.1016/j.yjmcc.2015.12.024.

[10] Myerburg RJ. Implantable cardioverter defibrillators after myocardial infarction. New England Journal of Medicine 2008;359:2245–53. https://doi.org/10.1056/nejmra0803409.

[11] Rog-Zielinska EA, Norris RA, Kohl P, Markwald R. The Living scar - cardiac fibroblasts and the injured heart. Trends in Molecular Medicine 2016;22:99–114. https://doi.org/10.1016/j.molmed.2015.12.006.

[12] Colvin M, Smith JM, Ahn Y, Skeans MA, Messick E, Bradbrook K, et al. OPTN/SRTR 2020 Annual Data Report: Heart. American J Transplantation 2022;22:350–437. https://doi.org/10.1111/ajt.16977.

[13] Colvin MM, Smith JM, Ahn YS, Handarova DK, Martinez AC, Lindblad KA, et al. OPTN/SRTR 2022 Annual Data Report: Heart. American Journal of Transplantation 2024;24:S305–93. https://doi.org/10.1016/j.ajt.2024.01.016.

[14] Cameli M, Pastore MC, Campora A, Lisi M, Mandoli GE. Donor shortage in heart transplantation: How can we overcome this challenge? Front Cardiovasc Med 2022;9:1001002. https://doi.org/10.3389/fcvm.2022.1001002.

[15] Liew LC, Ho BX, Soh B-S. Mending a broken heart: current strategies and limitations of cell-based therapy. Stem Cell Res Ther 2020;11:138. https://doi.org/10.1186/s13287-020-01648-0.

[16] Menasché P. Skeletal myoblasts and cardiac repair. Journal of Molecular and Cellular Cardiology 2008;45:545–53. https://doi.org/10.1016/j.yjmcc.2007.11.009.

[17] Nakamura K, Murry CE. Function Follows Form - A Review of Cardiac Cell Therapy. Circ J 2019;83:2399–412. https://doi.org/10.1253/circj.CJ-19-0567.

[18] Menasche P. Cardiac cell therapy: Lessons from clinical trials. Journal of Molecular and Cellular Cardiology 2011;50:258–65. https://doi.org/10.1016/j.yjmcc.2010.06.010.

[19] Soonpaa MH, Koh GY, Klug MG, Field LJ. Formation of Nascent Intercalated Disks Between Grafted Fetal Cardiomyocytes and Host Myocardium. Science 1994;264:98–101. https://doi.org/10.1126/science.8140423.

[20] Eschenhagen T, Ridders K, Weinberger F. How to repair a broken heart with pluripotent stem cell-derived cardiomyocytes. Journal of Molecular and Cellular Cardiology 2022;163:106–17. https://doi.org/10.1016/j.yjmcc.2021.10.005.

[21] Hashimoto H, Olson EN, Bassel-Duby R. Therapeutic approaches for cardiac regeneration and repair. Nat Rev Cardiol 2018;15:585–600. https://doi.org/10.1038/s41569-018-0036-6.

[22] Zhu Z, Huangfu D. Human pluripotent stem cells: an emerging model in developmental biology. Development 2013;140:705–17. https://doi.org/10.1242/dev.086165.

[23] Batalov I, Feinberg AW. Differentiation of Cardiomyocytes from Human Pluripotent Stem Cells Using Monolayer Culture: Supplementary Issue: Stem Cell Biology. Biomark Insights 2015;10s1:BMI.S20050. https://doi.org/10.4137/BMI.S20050.

[24] Silver SE, Barrs RW, Mei Y. Transplantation of Human Pluripotent Stem Cell-Derived Cardiomyocytes for Cardiac Regenerative Therapy. Front Cardiovasc Med 2021;8:707890. https://doi.org/10.3389/fcvm.2021.707890.

[25] Wang Q, Yang H, Bai A, Jiang W, Li X, Wang X, et al. Functional engineered human cardiac patches prepared from nature's platform improve heart function after acute myocardial infarction. Biomaterials 2016;105:52–65. https://doi.org/10.1016/j.biomaterials.2016.07.035.

[26] Kawaguchi S, Soma Y, Nakajima K, Kanazawa H, Tohyama S, Tabei R, et al. Intramyocardial Transplantation of Human iPS Cell–Derived Cardiac Spheroids Improves Cardiac Function in Heart Failure Animals. JACC: Basic to Translational Science 2021;6:239–54. https://doi.org/10.1016/j.jacbts.2020.11.017.

[27] Guragain B, Wei Y, Zhang H, Kahn-Krell A, Ye L, Walcott GP, et al. Implanted Human Cardiac Spheroids Electrically Couple With Infarcted Swine Myocardium. Circulation 2024;149:1855–7. https://doi.org/10.1161/CIRCULATIONAHA.123.068568.

[28] Yan W, Xia Y, Zhao H, Xu X, Ma X, Tao L. Stem cell-based therapy in cardiac repair after myocardial infarction: Promise, challenges, and future directions. Journal of Molecular and Cellular Cardiology 2024;188:1–14. https://doi.org/10.1016/j.yjmcc.2023.12.009.

[29] Jabbour RJ, Owen TJ, Pandey P, Reinsch M, Wang B, King O, et al. In vivo grafting of large engineered heart tissue patches for cardiac repair. JCI Insight 2021;6:e144068. https://doi.org/10.1172/jci.insight.144068.

[30] Gao L, Kupfer ME, Jung JP, Yang L, Zhang P, Da Sie Y, et al. Myocardial Tissue Engineering With Cells Derived From Human-Induced Pluripotent Stem Cells and a Native-Like, High-Resolution, 3-Dimensionally Printed Scaffold. Circulation Research 2017;120:1318–25. https://doi.org/10.1161/CIRCRESAHA.116.310277.

[31] Huang K, Ozpinar EW, Su T, Tang J, Shen D, Qiao L, et al. An off-the-shelf artificial cardiac patch improves cardiac repair after myocardial infarction in rats and pigs. Sci Transl Med 2020;12:eaat9683. https://doi.org/10.1126/scitranslmed.aat9683.

[32] Masumoto H, Nakane T, Tinney JP, Yuan F, Ye F, Kowalski WJ, et al. The myocardial regenerative potential of three-dimensional engineered cardiac tissues composed of multiple human iPS cell-derived cardiovascular cell lineages. Sci Rep 2016;6:29933. https://doi.org/10.1038/srep29933.

[33] Soma Y, Tani H, Morita-Umei Y, Kishino Y, Fukuda K, Tohyama S. Pluripotent stem cell-based cardiac regenerative therapy for heart failure. Journal of Molecular and Cellular Cardiology 2024;187:90–100. https://doi.org/10.1016/j.yjmcc.2023.12.001.

[34] Iyer RK, Chiu LL, Reis LA, Radisic M. Engineered cardiac tissues. Current Opinion in Biotechnology 2011;22:706–14. https://doi.org/10.1016/j.copbio.2011.04.004.

[35] Shimizu T, Yamato M, Isoi Y, Akutsu T, Setomaru T, Abe K, et al. Fabrication of Pulsatile Cardiac Tissue Grafts Using a Novel 3-Dimensional Cell Sheet Manipulation Technique and Temperature-Responsive Cell Culture Surfaces. Circulation Research 2002;90. https://doi.org/10.1161/hh0302.105722.

[36] Zhang J. Engineered Tissue Patch for Cardiac Cell Therapy. Curr Treat Options Cardio Med 2015;17:37. https://doi.org/10.1007/s11936-015-0399-5.

[37] Weinberger F, Breckwoldt K, Pecha S, Kelly A, Geertz B, Starbatty J, et al. Cardiac repair in guinea pigs with human engineered heart tissue from induced pluripotent stem cells. Sci Transl Med 2016;8. https://doi.org/10.1126/scitranslmed.aaf8781.

[38] Gao L, Gregorich ZR, Zhu W, Mattapally S, Oduk Y, Lou X, et al. Large Cardiac Muscle Patches Engineered From Human Induced-Pluripotent Stem Cell–Derived Cardiac Cells Improve Recovery From Myocardial Infarction in Swine. Circulation 2018;137:1712–30. https://doi.org/10.1161/CIRCULATIONAHA.117.030785.

[39] Querdel E, Reinsch M, Castro L, Köse D, Bähr A, Reich S, et al. Human Engineered Heart Tissue Patches Remuscularize the Injured Heart in a Dose-Dependent Manner. Circulation 2021;143:1991–2006. https://doi.org/10.1161/CIRCULATIONAHA.120.047904.

[40] Leor J, Aboulafia-Etzion S, Dar A, Shapiro L, Barbash IM, Battler A, et al. Bioengineered Cardiac Grafts: A New Approach to Repair the Infarcted Myocardium? Circulation 2000;102. https://doi.org/10.1161/circ.102.suppl_3.III-56.

[41] Stevens KR, Kreutziger KL, Dupras SK, Korte FS, Regnier M, Muskheli V, et al. Physiological function and transplantation of scaffold-free and vascularized human cardiac muscle tissue. Proc Natl Acad Sci USA 2009;106:16568–73. https://doi.org/10.1073/pnas.0908381106.

[42] Zhang J, Zhu W, Radisic M, Vunjak-Novakovic G. Can We Engineer a Human Cardiac Patch for Therapy? Circ Res 2018;123:244–65. https://doi.org/10.1161/CIRCRESAHA.118.311213.

[43] Shadrin IY, Allen BW, Qian Y, Jackman CP, Carlson AL, Juhas ME, et al. Cardiopatch platform enables maturation and scale-up of human pluripotent stem cell-derived engineered heart tissues. Nat Commun 2017;8:1825. https://doi.org/10.1038/s41467-017-01946-x.

[44] Leonard A, Bertero A, Powers JD, Beussman KM, Bhandari S, Regnier M, et al. Afterload promotes maturation of human induced pluripotent stem cell derived cardiomyocytes in engineered heart tissues. J Mol Cell Cardiol 2018;118:147–58. https://doi.org/10.1016/j.yjmcc.2018.03.016.

[45] Hirt MN, Boeddinghaus J, Mitchell A, Schaaf S, Börnchen C, Müller C, et al. Functional improvement and maturation of rat and human engineered heart tissue by chronic electrical stimulation. Journal of Molecular and Cellular Cardiology 2014;74:151–61. https://doi.org/10.1016/j.yjmcc.2014.05.009.

[46] Gerbin KA, Yang X, Murry CE, Coulombe KLK. Enhanced Electrical Integration of Engineered Human Myocardium via Intramyocardial versus Epicardial Delivery in Infarcted Rat Hearts. PLOS ONE 2015;10:e0131446. https://doi.org/10.1371/journal.pone.0131446.

[47] Lancaster JJ, Grijalva A, Fink J, Ref J, Daugherty S, Whitman S, et al. Biologically derived epicardial patch induces macrophage mediated pathophysiologic repair in chronically infarcted swine hearts. Commun Biol 2023;6:1–14. https://doi.org/10.1038/s42003-023-05564-w.

[48] Lancaster JJ, Sanchez P, Repetti GG, Juneman E, Pandey AC, Chinyere IR, et al. Human Induced Pluripotent Stem Cell–Derived Cardiomyocyte Patch in Rats With Heart Failure. The Annals of Thoracic Surgery 2019;108:1169–77. https://doi.org/10.1016/j.athoracsur.2019.03.099.

[49] Liu YW, Chen B, Yang X, Fugate JA, Kalucki FA, Futakuchi-Tsuchida A, et al. Human embryonic stem cell-derived cardiomyocytes restore function in infarcted hearts of non-human primates. Nature Biotechnology 2018;36:597–605. https://doi.org/10.1038/nbt.4162.

[50] Chong JJH, Yang X, Don CW, Minami E, Liu YW, Weyers JJ, et al. Human embryonic-stem-cell-derived cardiomyocytes regenerate non-human primate hearts. Nature 2014;510:273–7. https://doi.org/10.1038/nature13233.

[51] Nakamura K, Neidig LE, Yang X, Weber GJ, El-Nachef D, Tsuchida H, et al. Pharmacologic therapy for engraftment arrhythmia induced by transplantation of human cardiomyocytes. Stem Cell Reports 2021;16:2473–87. https://doi.org/10.1016/J.STEMCR.2021.08.005.

[52] Dhahri W, Sadikov Valdman T, Wilkinson D, Pereira E, Ceylan E, Andharia N, et al. In Vitro Matured Human Pluripotent Stem Cell–Derived Cardiomyocytes Form Grafts With Enhanced Structure and Function in Injured Hearts. Circulation 2022;145:1412–26. https://doi.org/10.1161/CIRCULATIONAHA.121.053563.

[53] Caspi O, Huber I, Kehat I, Habib M, Arbel G, Gepstein A, et al. Transplantation of Human Embryonic Stem Cell-Derived Cardiomyocytes Improves Myocardial Performance in Infarcted Rat Hearts. Journal of the American College of Cardiology 2007;50:1884–93. https://doi.org/10.1016/j.jacc.2007.07.054.

[54] Romagnuolo R, Masoudpour H, Porta-Sánchez A, Qiang B, Barry J, Laskary A, et al. Human Embryonic Stem Cell-Derived Cardiomyocytes Regenerate the Infarcted Pig Heart but Induce Ventricular Tachyarrhythmias. Stem Cell Reports 2019;12:967–81. https://doi.org/10.1016/J.STEMCR.2019.04.005.
[55] Shiba Y, Fernandes S, Zhu WZ, Filice D, Muskheli V, Kim J, et al. Human ES-cell-derived cardiomyocytes electrically couple and suppress arrhythmias in injured hearts. Nature 2012;489:322–5. https://doi.org/10.1038/nature11317.
[56] Kadota S, Pabon L, Reinecke H, Murry CE. In Vivo Maturation of Human Induced Pluripotent Stem Cell-Derived Cardiomyocytes in Neonatal and Adult Rat Hearts. Stem Cell Reports 2017;8:278–89. https://doi.org/10.1016/j.stemcr.2016.10.009.
[57] Laflamme MA, Chen KY, Naumova AV, Muskheli V, Fugate JA, Dupras SK, et al. Cardiomyocytes derived from human embryonic stem cells in pro-survival factors enhance function of infarcted rat hearts. Nature Biotechnology 2007;25:1015–24. https://doi.org/10.1038/nbt1327.
[58] Heartseed Inc. A Phase I/II Study of Human Induced Pluripotent Stem (iPS) Cell-derived Cardiomyocyte Spheroids (HS-001) in Patients With Severe Heart Failure, Secondary to Ischemic Heart Disease. clinicaltrials.gov; 2024.
[59] Wu JC. A Phase I, Randomized Pilot Study of Human Embryonic Stem Cell-Derived Cardiomyocytes (hESC-CMs) in PaTients With ChrOnic Ischemic Left VentRicular Dysfunction Secondary to Myocardial Infarction (HECTOR). clinicaltrials.gov; 2023.
[60] Zhang H, Xue Y, Pan T, Zhu X, Chong H, Xu C, et al. Epicardial injection of allogeneic human-induced-pluripotent stem cell-derived cardiomyocytes in patients with advanced heart failure: protocol for a phase I/IIa dose-escalation clinical trial. BMJ Open 2022;12:e056264. https://doi.org/10.1136/bmjopen-2021-056264.
[61] Tao L, Help Therapeutics. Treating Congestive HF With hiPSC-CMs Through Endocardial Injection. clinicaltrials.gov; n.d.
[62] Karbassi E, Fenix A, Marchiano S, Muraoka N, Nakamura K, Yang X, et al. Cardiomyocyte maturation: advances in knowledge and implications for regenerative medicine. Nature Reviews Cardiology 2020;17:341–59. https://doi.org/10.1038/s41569-019-0331-x.
[63] Marchianò S, Bertero A, Murry CE. Learn from Your Elders: Developmental Biology Lessons to Guide Maturation of Stem Cell-Derived Cardiomyocytes. Pediatric Cardiology 2019;40:1367–87. https://doi.org/10.1007/s00246-019-02165-5.
[64] Yang X, Pabon L, Murry CE. Engineering Adolescence: Maturation of Human Pluripotent Stem Cell–Derived Cardiomyocytes. Circ Res 2014;114:511–23. https://doi.org/10.1161/CIRCRESAHA.114.300558.
[65] Herron TJ, Rocha AMD, Campbell KF, Ponce-Balbuena D, Willis BC, Guerrero-Serna G, et al. Extracellular Matrix–Mediated Maturation of Human Pluripotent Stem Cell–Derived Cardiac Monolayer Structure and Electrophysiological Function. Circ: Arrhythmia and Electrophysiology 2016;9:e003638. https://doi.org/10.1161/CIRCEP.113.003638.
[66] Marchiano S, Nakamura K, Reinecke H, Neidig L, Lai M, Kadota S, et al. Gene editing to prevent ventricular arrhythmias associated with cardiomyocyte cell therapy. Cell Stem Cell 2023;30:396-414.e9. https://doi.org/10.1016/j.stem.2023.03.010.

[67] Zhang Y, Barocas VH, Berceli SA, Clancy CE, Eckmann DM, Garbey M, et al. Multi-scale Modeling of the Cardiovascular System: Disease Development, Progression, and Clinical Intervention. Annals of Biomedical Engineering 2016;44:2642–60. https://doi.org/10.1007/s10439-016-1628-0.

[68] Pathmanathan P, Gray RA. Validation and trustworthiness of multiscale models of cardiac electrophysiology. Frontiers in Physiology 2018;9:106. https://doi.org/10.3389/fphys.2018.00106.

[69] Kernik DC, Morotti S, Wu HD, Garg P, Duff HJ, Kurokawa J, et al. A computational model of induced pluripotent stem-cell derived cardiomyocytes incorporating experimental variability from multiple data sources. Journal of Physiology 2019;597:4533–64. https://doi.org/10.1113/JP277724.

[70] Koivumäki JT, Naumenko N, Tuomainen T, Takalo J, Oksanen M, Puttonen KA, et al. Structural Immaturity of Human iPSC-Derived Cardiomyocytes: In Silico Investigation of Effects on Function and Disease Modeling. Front Physiol 2018;9:Suppl 14. https://doi.org/10.3389/fphys.2018.00080.

[71] Paci M, Hyttinen J, Aalto-Setälä K, Severi S. Computational models of ventricular-and atrial-like human induced pluripotent stem cell derived cardiomyocytes. Annals of Biomedical Engineering 2013;41:2334–48. https://doi.org/10.1007/s10439-013-0833-3.

[72] Paci M, Passini E, Severi S, Hyttinen J, Rodriguez B. Phenotypic variability in LQT3 human induced pluripotent stem cell-derived cardiomyocytes and their response to antiarrhythmic pharmacologic therapy: An in silico approach. Heart Rhythm 2017;14:1704–12. https://doi.org/10.1016/j.hrthm.2017.07.026.

[73] Paci M, Passini E, Klimas A, Severi S, Hyttinen J, Rodriguez B, et al. All-optical electrophysiology refines populations of in silico human iPSC-CMs for drug evaluation. Biophysical Journal 2020:1–16. https://doi.org/10.1016/j.bpj.2020.03.018.

[74] Paci M, Koivumäki JT, Lu HR, Gallacher DJ, Passini E, Rodriguez B. Comparison of the Simulated Response of Three in Silico Human Stem Cell-Derived Cardiomyocytes Models and in Vitro Data Under 15 Drug Actions. Frontiers in Pharmacology 2021;12:1–16. https://doi.org/10.3389/fphar.2021.604713.

[75] Yu JK, Franceschi W, Huang Q, Pashakhanloo F, Boyle PM, Trayanova NA. A comprehensive, multiscale framework for evaluation of arrhythmias arising from cell therapy in the whole post-myocardial infarcted heart. Scientific Reports 2019;9:1–16. https://doi.org/10.1038/s41598-019-45684-0.

[76] Yu JK, Liang JA, Franceschi WH, Huang Q, Pashakhanloo F, Sung E, et al. Assessment of arrhythmia mechanism and burden of the infarcted ventricles following remuscularization with pluripotent stem cell-derived cardiomyocyte patches using patient-derived models. Cardiovascular Research 2022;118:1247–61. https://doi.org/10.1093/CVR/CVAB140.

[77] Yu JK, Liang JA, Weinberg SH, Trayanova NA. Computational modeling of aberrant electrical activity following remuscularization with intramyocardially injected pluripotent stem cell-derived cardiomyocytes. Journal of Molecular and Cellular Cardiology 2022;162:97–109. https://doi.org/10.1016/j.yjmcc.2021.08.011.

[78] Fassina D, Costa CM, Longobardi S, Karabelas E, Plank G, Harding SE, et al. Modelling the interaction between stem cells derived cardiomyocytes patches and host myocardium

to aid non-arrhythmic engineered heart tissue design. PLoS Comput Biol 2022;18:e1010030. https://doi.org/10.1371/journal.pcbi.1010030.

[79] Gibbs CE, Marchianó S, Zhang K, Yang X, Murry CE, Boyle PM. Graft–host coupling changes can lead to engraftment arrhythmia: a computational study. The Journal of Physiology 2023;601:2733–49. https://doi.org/10.1113/JP284244.

[80] Vos T, Lim SS, Abbafati C, Abbas KM, Abbasi M, Abbasifard M, et al. Global burden of 369 diseases and injuries in 204 countries and territories, 1990–2019: a systematic analysis for the Global Burden of Disease Study 2019. The Lancet 2020;396:1204–22. https://doi.org/10.1016/S0140-6736(20)30925-9.

[81] Bergmann O, Bhardwaj RD, Bernard S, Zdunek S, Barnabé-Heider F, Walsh S, et al. Evidence for cardiomyocyte renewal in humans. Science 2009;324:98–102. https://doi.org/10.1126/science.1164680.

[82] Prabhu SD, Frangogiannis NG. The Biological Basis for Cardiac Repair After Myocardial Infarction: From Inflammation to Fibrosis. Circ Res 2016;119:91–112. https://doi.org/10.1161/CIRCRESAHA.116.303577.

[83] Velagaleti RS, Pencina MJ, Murabito JM, Wang TJ, Parikh NI, D'Agostino RB, et al. Long-Term Trends in the Incidence of Heart Failure After Myocardial Infarction. Circulation 2008;118:2057–62. https://doi.org/10.1161/CIRCULATIONAHA.108.784215.

[84] Ezekowitz JA, Kaul P, Bakal JA, Armstrong PW, Welsh RC, McAlister FA. Declining In-Hospital Mortality and Increasing Heart Failure Incidence in Elderly Patients With First Myocardial Infarction. Journal of the American College of Cardiology 2009;53:13–20. https://doi.org/10.1016/j.jacc.2008.08.067.

[85] Gerber Y, Weston SA, Enriquez-Sarano M, Berardi C, Chamberlain AM, Manemann SM, et al. Mortality Associated With Heart Failure After Myocardial Infarction: A Contemporary Community Perspective. Circ: Heart Failure 2016;9. https://doi.org/10.1161/CIRCHEARTFAILURE.115.002460.

[86] Bahit MC, Kochar A, Granger CB. Post-Myocardial Infarction Heart Failure. JACC: Heart Failure 2018;6:179–86. https://doi.org/10.1016/j.jchf.2017.09.015.

[87] Eschenhagen T, Bolli R, Braun T, Field LJ, Fleischmann BK, Frisén J, et al. Cardiomyocyte Regeneration: A Consensus Statement. Circulation 2017;136:680–6. https://doi.org/10.1161/CIRCULATIONAHA.117.029343.

[88] Bertero A, Murry CE. Hallmarks of cardiac regeneration. Nat Rev Cardiol 2018;15:579–80. https://doi.org/10.1038/s41569-018-0079-8.

[89] Laflamme MA, Gold J, Xu C, Hassanipour M, Rosler E, Police S, et al. Formation of Human Myocardium in the Rat Heart from Human Embryonic Stem Cells. The American Journal of Pathology 2005;167:663–71. https://doi.org/10.1016/S0002-9440(10)62041-X.

[90] Shiba Y, Gomibuchi T, Seto T, Wada Y, Ichimura H, Tanaka Y, et al. Allogeneic transplantation of iPS cell-derived cardiomyocytes regenerates primate hearts. Nature 2016;538:388–91. https://doi.org/10.1038/nature19815.

[91] Filice D, Dhahri W, Solan JL, Lampe PD, Steele E, Milani N, et al. Optical mapping of human embryonic stem cell-derived cardiomyocyte graft electrical activity in injured hearts. Stem Cell Research & Therapy 2020;11:417. https://doi.org/10.1186/s13287-020-01919-w.

[92] Peinkofer G, Burkert K, Urban K, Krausgrill B, Hescheler J, Saric T, et al. From Early Embryonic to Adult Stage: Comparative Study of Action Potentials of Native and Pluripotent Stem Cell-Derived Cardiomyocytes. Stem Cells Dev 2016;25:1397–406. https://doi.org/10.1089/scd.2016.0073.

[93] Guo Y, Pu WT. Cardiomyocyte Maturation: New Phase in Development. Circ Res 2020;126:1086–106. https://doi.org/10.1161/CIRCRESAHA.119.315862.

[94] Lundy SD, Zhu W-Z, Regnier M, Laflamme MA. Structural and Functional Maturation of Cardiomyocytes Derived from Human Pluripotent Stem Cells. Stem Cells and Development 2013;22:1991–2002. https://doi.org/10.1089/scd.2012.0490.

[95] Moreno JD, Zhu ZI, Yang P-C, Bankston JR, Jeng M-T, Kang C, et al. A Computational Model to Predict the Effects of Class I Anti-Arrhythmic Drugs on Ventricular Rhythms. Sci Transl Med 2011;3. https://doi.org/10.1126/scitranslmed.3002588.

[96] Boyle PM, Franceschi WH, Constantin M, Hawks C, Desplantez T, Trayanova NA, et al. New insights on the cardiac safety factor: Unraveling the relationship between conduction velocity and robustness of propagation. Journal of Molecular and Cellular Cardiology 2019;128:117–28. https://doi.org/10.1016/j.yjmcc.2019.01.010.

[97] Boyle PM, Zghaib T, Zahid S, Ali RL, Deng D, Franceschi WH, et al. Computationally guided personalized targeted ablation of persistent atrial fibrillation. Nature Biomedical Engineering 2019. https://doi.org/10.1038/s41551-019-0437-9.

[98] Arevalo HJ, Vadakkumpadan F, Guallar E, Jebb A, Malamas P, Wu KC, et al. Arrhythmia risk stratification of patients after myocardial infarction using personalized heart models. Nature Communications 2016;7:1–8. https://doi.org/10.1038/ncomms11437.

[99] Trayanova NA, Pashakhanloo F, Wu KC, Halperin HR. Imaging-Based Simulations for Predicting Sudden Death and Guiding Ventricular Tachycardia Ablation. Circ: Arrhythmia and Electrophysiology 2017;10:e004743. https://doi.org/10.1161/CIRCEP.117.004743.

[100] Papadacci C, Finel V, Provost J, Villemain O, Bruneval P, Gennisson J-L, et al. Imaging the dynamics of cardiac fiber orientation in vivo using 3D Ultrasound Backscatter Tensor Imaging. Sci Rep 2017;7:830. https://doi.org/10.1038/s41598-017-00946-7.

[101] Williams NP, Rhodehamel M, Yan C, Smith AST, Jiao A, Murry CE, et al. Engineering anisotropic 3D tubular tissues with flexible thermoresponsive nanofabricated substrates. Biomaterials 2020;240:119856. https://doi.org/10.1016/j.biomaterials.2020.119856.

[102] Palpant NJ, Pabon L, Friedman CE, Roberts M, Hadland B, Zaunbrecher RJ, et al. Generating high-purity cardiac and endothelial derivatives from patterned mesoderm using human pluripotent stem cells. Nat Protoc 2017;12:15–31. https://doi.org/10.1038/nprot.2016.153.

[103] Costa CM, Silva PAA, Santos RWD. Mind the Gap: A semicontinuum model for discrete electrical propagation in cardiac tissue. IEEE Transactions on Biomedical Engineering 2016;63:765–74. https://doi.org/10.1109/TBME.2015.2470256.

[104] Li S, Chen G, Li RA. Calcium signalling of human pluripotent stem cell-derived cardiomyocytes. J Physiol 2013;591:5279–90. https://doi.org/10.1113/jphysiol.2013.256495.

[105] Ivashchenko CY, Pipes GC, Lozinskaya IM, Lin Z, Xiaoping X, Needle S, et al. Human-induced pluripotent stem cell-derived cardiomyocytes exhibit temporal changes in

phenotype. American Journal of Physiology-Heart and Circulatory Physiology 2013;305:H913–22. https://doi.org/10.1152/ajpheart.00819.2012.

[106] Verkerk AO, van Ginneken ACG, Wilders R. Pacemaker activity of the human sinoatrial node: Role of the hyperpolarization-activated current, If. International Journal of Cardiology 2009;132:318–36. https://doi.org/10.1016/j.ijcard.2008.12.196.

[107] Kim JJ, Yang L, Lin B, Zhu X, Sun B, Kaplan AD, et al. Mechanism of automaticity in cardiomyocytes derived from human induced pluripotent stem cells. J Mol Cell Cardiol 2015;81:81–93. https://doi.org/10.1016/j.yjmcc.2015.01.013.

[108] Sun Y, Timofeyev V, Dennis A, Bektik E, Wan X, Laurita KR, et al. A Singular Role of IK1 Promoting the Development of Cardiac Automaticity during Cardiomyocyte Differentiation by IK1 -Induced Activation of Pacemaker Current. Stem Cell Rev Rep 2017;13:631–43. https://doi.org/10.1007/s12015-017-9745-1.

[109] Ten Tusscher KHWJ, Panfilov AV. Alternans and spiral breakup in a human ventricular tissue model. American Journal of Physiology - Heart and Circulatory Physiology 2006;291:1088–100. https://doi.org/10.1152/ajpheart.00109.2006.

[110] Vigmond E, Vadakkumpadan F, Gurev V, Arevalo H, Deo M, Plank G, et al. Towards predictive modelling of the electrophysiology of the heart: Predictive modelling of cardiac electrophysiology. Experimental Physiology 2009;94:563–77. https://doi.org/10.1113/expphysiol.2008.044073.

[111] Rocha BM, Kickinger F, Prassl AJ, Haase G, Vigmond EJ, Weber dos Santos R, et al. A Macro Finite-Element Formulation for Cardiac Electrophysiology Simulations Using Hybrid Unstructured Grids. IEEE Trans Biomed Eng 2011;58:1055–65. https://doi.org/10.1109/TBME.2010.2064167.

[112] Balaban G, Costa CM, Porter B, Halliday B, Rinaldi CA, Prasad S, et al. 3D Electrophysiological Modeling of Interstitial Fibrosis Networks and Their Role in Ventricular Arrhythmias in Non-Ischemic Cardiomyopathy. IEEE Trans Biomed Eng 2020;67:3125–33. https://doi.org/10.1109/TBME.2020.2976924.

[113] Bifulco SF, Scott GD, Sarairah S, Birjandian Z, Roney CH, Niederer SA, et al. Computational modeling identifies embolic stroke of undetermined source patients with potential arrhythmic substrate. eLife 2021;10:e64213. https://doi.org/10.7554/eLife.64213.

[114] Ochs AR, Karathanos TV, Trayanova NA, Boyle PM. Optogenetic Stimulation Using Anion Channelrhodopsin (GtACR1) Facilitates Termination of Reentrant Arrhythmias With Low Light Energy Requirements: A Computational Study. Front Physiol 2021;12. https://doi.org/10.3389/fphys.2021.718622.

[115] O'Hara RP, Binka E, Prakosa A, Zimmerman SL, Cartoski MJ, Abraham MR, et al. Personalized computational heart models with T1-mapped fibrotic remodeling predict sudden death risk in patients with hypertrophic cardiomyopathy. eLife 2022;11:e73325. https://doi.org/10.7554/eLife.73325.

[116] Prakosa A, Arevalo HJ, Deng D, Boyle PM, Nikolov PP, Ashikaga H, et al. Personalized virtual-heart technology for guiding the ablation of infarct-related ventricular tachycardia. Nat Biomed Eng 2018;2:732–40. https://doi.org/10.1038/s41551-018-0282-2.

[117] Connolly AJ, Bishop MJ. Computational Representations of Myocardial Infarct Scars and Implications for Arrhythmogenesis. Clin Med Insights Cardiol 2016;10s1:CMC.S39708. https://doi.org/10.4137/CMC.S39708.

[118] Plank G, Loewe A, Neic A, Augustin C, Huang Y-L, Gsell MAF, et al. The openCARP simulation environment for cardiac electrophysiology. Computer Methods and Programs in Biomedicine 2021;208:106223. https://doi.org/10.1016/j.cmpb.2021.106223.

[119] Spector P. Principles of cardiac electric propagation and their implications for re-entrant arrhythmias. Circ Arrhythm Electrophysiol 2013;6:655–61. https://doi.org/10.1161/CIRCEP.113.000311.

[120] Quinn TA, Camelliti P, Rog-Zielinska EA, Siedlecka U, Poggioli T, O'Toole ET, et al. Electrotonic coupling of excitable and nonexcitable cells in the heart revealed by optogenetics. Proc Natl Acad Sci USA 2016;113:14852–7. https://doi.org/10.1073/pnas.1611184114.

[121] Hulsmans M, Clauss S, Xiao L, Aguirre AD, King KR, Hanley A, et al. Macrophages Facilitate Electrical Conduction in the Heart. Cell 2017;169:510-522.e20. https://doi.org/10.1016/j.cell.2017.03.050.

[122] Dhanjal TS, Lellouche N, von RCJ, Abehsira G, Edwards DH, Dubois -Randé Jean-Luc, et al. Massive Accumulation of Myofibroblasts in the Critical Isthmus Is Associated With Ventricular Tachycardia Inducibility in Post-Infarct Swine Heart. JACC: Clinical Electrophysiology 2017;3:703–14. https://doi.org/10.1016/j.jacep.2016.11.010.

[123] Luo CH, Rudy Y. A model of the ventricular cardiac action potential. Depolarization, repolarization, and their interaction. Circ Res 1991;68:1501–26. https://doi.org/10.1161/01.res.68.6.1501.

[124] Jackman CP, Ganapathi AM, Asfour H, Qian Y, Allen BW, Li Y, et al. Engineered cardiac tissue patch maintains structural and electrical properties after epicardial implantation. Biomaterials 2018;159:48–58. https://doi.org/10.1016/j.biomaterials.2018.01.002.

[125] Sottas V, Wahl C-M, Trache MC, Bartolf-Kopp M, Cambridge S, Hecker M, et al. Improving electrical properties of iPSC-cardiomyocytes by enhancing Cx43 expression. Journal of Molecular and Cellular Cardiology 2018;120:31–41. https://doi.org/10.1016/j.yjmcc.2018.05.010.

[126] Tsao CW, Aday AW, Almarzooq ZI, Anderson CAM, Arora P, Avery CL, et al. Heart Disease and Stroke Statistics—2023 Update: A Report From the American Heart Association. Circulation 2023;147. https://doi.org/10.1161/CIR.0000000000001123.

[127] Caulfield JB, Leinbach R, Gold H. The relationship of myocardial infarct size and prognosis. Circulation 1976;53:I141-144.

[128] Murry CE, Reinecke H, Pabon LM. Regeneration Gaps. Journal of the American College of Cardiology 2006;47:1777–85. https://doi.org/10.1016/j.jacc.2006.02.002.

[129] Rossignol P, Hernandez AF, Solomon SD, Zannad F. Heart failure drug treatment. The Lancet 2019;393:1034–44. https://doi.org/10.1016/S0140-6736(18)31808-7.

[130] Tromp J, Ouwerkerk W, van VDJ, Hillege HL, Richards AM, van der MP, et al. A Systematic Review and Network Meta-Analysis of Pharmacological Treatment of Heart Failure With Reduced Ejection Fraction. JACC: Heart Failure 2022;10:73–84. https://doi.org/10.1016/j.jchf.2021.09.004.

[131] Marchiano S, Nakamura K, Reinecke H, Neidig L, Lai M, Kadota S, et al. Gene editing to prevent ventricular arrhythmias associated with cardiomyocyte cell therapy. Cell Stem Cell 2023;30:396-414.e9. https://doi.org/10.1016/j.stem.2023.03.010.

[132] Boyle PM, Williams JC, Ambrosi CM, Entcheva E, Trayanova NA. A comprehensive multiscale framework for simulating optogenetics in the heart. Nat Commun 2013;4:2370. https://doi.org/10.1038/ncomms3370.

[133] Boyle PM, Vigmond EJ. An Intuitive Safety Factor for Cardiac Propagation. Biophysical Journal 2010;98:L57–9. https://doi.org/10.1016/j.bpj.2010.03.018.

[134] Bifulco SF, Scott GD, Sarairah S, Birjandian Z, Roney CH, Niederer SA, et al. Computational modeling identifies embolic stroke of undetermined source patients with potential arrhythmic substrate. eLife 2021;10:e64213. https://doi.org/10.7554/eLife.64213.

[135] Strocchi M, Augustin CM, Gsell MAF, Karabelas E, Neic A, Gillette K, et al. A publicly available virtual cohort of fourchamber heart meshes for cardiac electromechanics simulations. PLoS ONE 2020;15:1–26. https://doi.org/10.1371/journal.pone.0235145.

[136] Martínez Díaz P, Sánchez J, Fitzen N, Ravens U, Dössel O, Loewe A. The right atrium affects *in silico* arrhythmia vulnerability in both atria. Heart Rhythm 2024. https://doi.org/10.1016/j.hrthm.2024.01.047.

[137] Zhang Y, Zhang K, Prakosa A, James C, Zimmerman SL, Carrick R, et al. Predicting ventricular tachycardia circuits in patients with arrhythmogenic right ventricular cardiomyopathy using genotype-specific heart digital twins. eLife 2023;12:RP88865. https://doi.org/10.7554/eLife.88865.

[138] Space Constant - an overview | ScienceDirect Topics n.d. https://www.sciencedirect.com/topics/engineering/space-constant (accessed March 26, 2024).

[139] Carmeliet E. Conduction in cardiac tissue. Historical reflections. Physiol Rep 2019;7:e13860. https://doi.org/10.14814/phy2.13860.

[140] The pandas development team. pandas-dev/pandas: Pandas 2024. https://doi.org/10.5281/ZENODO.10957263.

[141] Harris CR, Millman KJ, Van Der Walt SJ, Gommers R, Virtanen P, Cournapeau D, et al. Array programming with NumPy. Nature 2020;585:357–62. https://doi.org/10.1038/s41586-020-2649-2.

[142] Hunter JD. Matplotlib: A 2D Graphics Environment. Comput Sci Eng 2007;9:90–5. https://doi.org/10.1109/MCSE.2007.55.

[143] Virtanen P, Gommers R, Oliphant TE, Haberland M, Reddy T, Cournapeau D, et al. SciPy 1.0: fundamental algorithms for scientific computing in Python. Nat Methods 2020;17:261–72. https://doi.org/10.1038/s41592-019-0686-2.

[144] Pedregosa F, Varoquaux G, Gramfort A, Michel V, Thirion B, Grisel O, et al. Scikit-learn: Machine Learning in Python. Journal of Machine Learning Research 2011;12:2825–30.

[145] Cheng Y-C, Hsieh ML, Lin C-J, Chang CMC, Huang C-Y, Puntney R, et al. Combined Treatment of Human Induced Pluripotent Stem Cell-Derived Cardiomyocytes and Endothelial Cells Regenerate the Infarcted Heart in Mice and Non-Human Primates. Circulation 2023;148:1395–409. https://doi.org/10.1161/CIRCULATIONAHA.122.061736.

[146] Riebel LL, Wang ZJ, Martinez-Navarro H, Trovato C, Camps J, Berg LA, et al. In silico evaluation of cell therapy in acute versus chronic infarction: role of automaticity, heterogeneity and Purkinje in human. Sci Rep 2024;14:21584. https://doi.org/10.1038/s41598-024-67951-5.

[147] Deng D, Prakosa A, Shade J, Nikolov P, Trayanova NA. Sensitivity of Ablation Targets Prediction to Electrophysiological Parameter Variability in Image-Based Computational Models of Ventricular Tachycardia in Post-infarction Patients. Front Physiol 2019;10:628. https://doi.org/10.3389/fphys.2019.00628.

[148] Wang Y, Li Q, Tao B, Angelini M, Ramadoss S, Sun B, et al. Fibroblasts in heart scar tissue directly regulate cardiac excitability and arrhythmogenesis. Science 2023;381:1480–7. https://doi.org/10.1126/science.adh9925.

[149] Salari N, Morddarvanjoghi F, Abdolmaleki A, Rasoulpoor S, Khaleghi AA, Hezarkhani LA, et al. The global prevalence of myocardial infarction: a systematic review and meta-analysis. BMC Cardiovascular Disorders 2023;23:206. https://doi.org/10.1186/s12872-023-03231-w.

[150] Mechanic OJ, Gavin M, Grossman SA. Acute Myocardial Infarction. StatPearls, Treasure Island (FL): StatPearls Publishing; 2024.

[151] Thygesen K, Alpert JS, White HD, Joint ESC/ACCF/AHA/WHF Task Force for the Redefinition of Myocardial Infarction. Universal Definition of Myocardial Infarction. Circulation 2007;116:2634–53. https://doi.org/10.1161/CIRCULATIONAHA.107.187397.

[152] Breckwoldt K, Weinberger F, Eschenhagen T. Heart regeneration. Biochimica et Biophysica Acta (BBA) - Molecular Cell Research 2016;1863:1749–59. https://doi.org/10.1016/j.bbamcr.2015.11.010.

[153] Sun Y, Weber KT. Infarct scar: a dynamic tissue. Cardiovascular Research 2000;46:250–6. https://doi.org/10.1016/S0008-6363(00)00032-8.

[154] Frangogiannis NG, Smith CW, Entman ML. The inflammatory response in myocardial infarction. Cardiovasc Res 2002;53:31–47. https://doi.org/10.1016/s0008-6363(01)00434-5.

[155] Sharpe N. Ventricular remodeling following myocardial infarction. The American Journal of Cardiology 1992;70:20–6. https://doi.org/10.1016/0002-9149(92)91354-7.

[156] van den Borne SWM, Diez J, Blankesteijn WM, Verjans J, Hofstra L, Narula J. Myocardial remodeling after infarction: the role of myofibroblasts. Nat Rev Cardiol 2010;7:30–7. https://doi.org/10.1038/nrcardio.2009.199.

[157] Hsich EM. Matching the Market for Heart Transplantation. Circulation: Heart Failure 2016;9:e002679. https://doi.org/10.1161/CIRCHEARTFAILURE.115.002679.

[158] Wu X, Wang D, Qin K, Iroegbu CD, Xiang K, Zhou Y, et al. Cardiac Repair With Echocardiography-Guided Multiple Percutaneous Left Ventricular Intramyocardial Injection of hiPSC-CMs After Myocardial Infarction. Front Cardiovasc Med 2021;8. https://doi.org/10.3389/fcvm.2021.768873.

[159] Guan X, Xu W, Zhang H, Wang Q, Yu J, Zhang R, et al. Transplantation of human induced pluripotent stem cell-derived cardiomyocytes improves myocardial function and reverses ventricular remodeling in infarcted rat hearts. Stem Cell Research and Therapy 2020;11:73. https://doi.org/10.1186/s13287-020-01602-0.

[160] Sung E, Etoz S, Zhang Y, Trayanova NA. Whole-heart ventricular arrhythmia modeling moving forward: Mechanistic insights and translational applications. Biophysics Reviews 2021;2:031304. https://doi.org/10.1063/5.0058050.

[161] Campos FO, Orini M, Arnold R, Whitaker J, O'Neill M, Razavi R, et al. Assessing the ability of substrate mapping techniques to guide ventricular tachycardia ablation using

computational modelling. Computers in Biology and Medicine 2021;130:104214. https://doi.org/10.1016/j.compbiomed.2021.104214.

[162] Bifulco SF, Akoum N, Boyle PM. Translational applications of computational modelling for patients with cardiac arrhythmias. Heart 2021;107:456–61. https://doi.org/10.1136/heartjnl-2020-316854.

[163] Paci M, Pölönen RP, Cori D, Penttinen K, Aalto-Setälä K, Severi S, et al. Automatic optimization of an in silico model of human iPSC derived cardiomyocytes recapitulating calcium handling abnormalities. Frontiers in Physiology 2018;9:1–14. https://doi.org/10.3389/fphys.2018.00709.

[164] Fijnvandraat AC, van Ginneken ACG, de Boer PAJ, Ruijter JM, Christoffels VM, Moorman AFM, et al. Cardiomyocytes derived from embryonic stem cells resemble cardiomyocytes of the embryonic heart tube. Cardiovascular Research 2003;58:399–409. https://doi.org/10.1016/S0008-6363(03)00282-7.

[165] Robertson C, Tran DD, George SC. Concise Review: Maturation Phases of Human Pluripotent Stem Cell-Derived Cardiomyocytes. Stem Cells (Dayton, Ohio) 2013;31:10.1002/stem.1331. https://doi.org/10.1002/stem.1331.

[166] Mendonca Costa C, Neic A, Kerfoot E, Porter B, Sieniewicz B, Gould J, et al. Pacing in proximity to scar during cardiac resynchronization therapy increases local dispersion of repolarization and susceptibility to ventricular arrhythmogenesis. Heart Rhythm 2019;16:1475–83. https://doi.org/10.1016/j.hrthm.2019.03.027.

[167] Moinuddin A, Ali SY, Goel A, Sethi Y, Patel N, Kaka N, et al. The age of computational cardiology and future of long-term ablation target prediction for ventricular tachycardia. Front Cardiovasc Med 2023;10. https://doi.org/10.3389/fcvm.2023.1233991.

[168] Ochs AR, Boyle PM. Optogenetic Modulation of Arrhythmia Triggers: Proof-of-Concept from Computational Modeling. Cell Mol Bioeng 2023;16:243–59. https://doi.org/10.1007/s12195-023-00781-z.

[169] Spodick DH. Normal sinus heart rate: Sinus tachycardia and sinus bradycardia redefined. American Heart Journal 1992;124:1119–21. https://doi.org/10.1016/0002-8703(92)91012-P.

[170] Mason JW, Ramseth DJ, Chanter DO, Moon TE, Goodman DB, Mendzelevski B. Electrocardiographic reference ranges derived from 79,743 ambulatory subjects. Journal of Electrocardiology 2007;40:228-234.e8. https://doi.org/10.1016/j.jelectrocard.2006.09.003.

[171] Nikolic G. Definition of ventricular tachycardia. Am J Cardiol 1982;50:1197–8. https://doi.org/10.1016/0002-9149(82)90443-x.

[172] Foth C, Gangwani MK, Ahmed I, Alvey H. Ventricular Tachycardia. StatPearls, Treasure Island (FL): StatPearls Publishing; 2024.

[173] Bayer JD, Sobota V, Bear LR, Haïssaguerre M, Vigmond EJ. A His bundle pacing protocol for suppressing ventricular arrhythmia maintenance and improving defibrillation efficacy. Computer Methods and Programs in Biomedicine 2024;253:108239. https://doi.org/10.1016/j.cmpb.2024.108239.

[174] Boyle PM, Massé S, Nanthakumar K, Vigmond EJ. Transmural IK(ATP) heterogeneity as a determinant of activation rate gradient during early ventricular fibrillation: Mechanistic

insights from rabbit ventricular models. Heart Rhythm 2013;10:1710–7. https://doi.org/10.1016/j.hrthm.2013.08.010.

[175] Boyle PM, Veenhuyzen GD, Vigmond EJ. Fusion during entrainment of orthodromic reciprocating tachycardia is enhanced for basal pacing sites but diminished when pacing near Purkinje system end points. Heart Rhythm 2013;10:444–51. https://doi.org/10.1016/j.hrthm.2012.11.021.

[176] Forouzandehmehr M, Koivumäki JT, Hyttinen J, Paci M. A mathematical model of hiPSC cardiomyocytes electromechanics. Physiological Reports 2021;9:e15124. https://doi.org/10.14814/phy2.15124.

[177] Cook MP, Dhahri W, Laflamme MA, Ghugre NR, Wright GA. Using diffusion tensor imaging to depict myocardial changes after matured pluripotent stem cell-derived cardiomyocyte transplantation. Journal of Cardiovascular Magnetic Resonance 2024;26:101045. https://doi.org/10.1016/j.jocmr.2024.101045.

[178] Lelovas PP, Kostomitsopoulos NG, Xanthos TT. A Comparative Anatomic and Physiologic Overview of the Porcine Heart. J Am Assoc Lab Anim Sci 2014;53:432–8.

[179] Dosdall DJ, Cheng K-A, Huang J, Allison JS, Allred JD, Smith WM, et al. Transmural and endocardial Purkinje activation in pigs before local myocardial activation after defibrillation shocks. Heart Rhythm 2007;4:758–65. https://doi.org/10.1016/j.hrthm.2007.02.017.